IMPLICATIONS OF LIMITED SLIP IN CRYSTAL PLASTICITY

A Thesis
Presented to
The Academic Faculty

by

Jeffrey Townsend Lloyd

In Partial Fulfillment
of the Requirements for the Degree
Master's of Science in the
Woodruff School of Mechanical Engineering

Georgia Institute of Technology
August, 2010

IMPLICATIONS OF LIMITED SLIP IN CRYSTAL PLASTICITY

Approved by:

Dr. David McDowell, Advisor
School of Mechanical Engineering
Georgia Institute of Technology

Dr. Rick Neu
School of Mechanical Engineering
Georgia Institute of Technology

Dr. Min Zhou
School of Mechanical Engineering
Georgia Institute of Technology

Date Approved: April 29, 2010

ACKNOWLEDGEMENTS

First, I would like to thanks Dr. David McDowell for advising me through this entire process. His knowledge of solid mechanics and materials science has been a great source during my research. I thank Dr. Min Zhou and Dr. Rick Neu for serving on my committee and providing thoughtful suggestions for this work.

Also, I would like to thank all of friends and fellow lab-mates for helping to make Georgia Tech and enjoyable time. I would like to thank my entire family from oldest to youngest; Gammy, Grandma Colleen, Mom, Dad, Mike and Rebecca, Bill, and Jeff, for their support and encouragement during this process. I would also like to thank Melanie for her patience, encouragement, and support during my thesis writing. Without my friends and family, I would have never made it this far!

TABLE OF CONTENTS

LIST OF FIGURES

LIST OF TABLES

ABSTRACT

Mechanisms that control polycrystalline deformation are rooted in a variety of length scales which are controlled by microstructural characteristics at each of these respective scales. Existing macroscale models that incorporate internal state variables (ISVs) to capture the overall response of the evolving microstructure can accurately reproduce the net response, but fail in predicting the variability or localized deformation caused by the material's microstructure.

In order to capture the non-uniform deformation response of polycrystalline metals at the largest controlling microstructural feature, crystal plasticity formulations were created that take into account the regular crystallographic lattice of each grain, and use this as the controlling microstructural length scale. In order to accurately model the effect of the grains, mesoscale deformation must be understood so that the overall response of the grain can be accurately modeled.

Traditionally, crystal plasticity models were formulated by incorporating crystallographic information about the regular lattice at the atomic scale into a local continuum formulation, so that local continuum stresses could be resolved onto the individual close packed slip planes responsible for mediating plastic deformation. While this method contains information from the crystallographic length scale, controlling mechanisms of deformation at the grain scale are largely ignored. Yielding and hardening relations are derived in a top-down approach by fitting constitutive parameters to macroscopic experiments. The deformation represented by this top-down approach of informing parameters from the macroscale is often unable to replicate the actual observed deformation patterns seen in micrographs at the scale of grains.

To better understand consequences of classical assumptions regarding deformation mechanisms at the mesoscale, experimental observations of mesoscale deformation are presented. In light of actual micrographics of deformed polycrystals, the Von Mises criterion which states that 5 independent plastic deformation sources are needed at each material point to satisfy compatibility is studied, and the consequences of violating this assumption are presented through comprehensive parametric studies. From these studies, it can be concluded that not only are 5 independent plastic deformation sources not needed or observed at each point, but if less than 5 sources are allowed to be active a new physical understanding of a mechanism for kinematic hardening emerges. Furthermore, for enhanced subgrain rotation and evolution the Von Mises criterion must be violated.

The second focus of this work is looking at studies, experiments, and models of mesoscale deformation in order to better understand controlling deformation length scales, so that they can be fed into a combined top-down, bottom-up, non-uniform crystal plasticity model that captures the variability provided by the mesoscale during deformation. This can in turn be used to more accurately model the heterogeneity provided by the response of each grain. The length scale intuited from insight into mesoscale deformation mechanisms through observation of experiments and analytical models is the free slip line length of each slip system, which informs non-uniform material parameters in a crystal plasticity model that control the yielding, hardening, and subsequent softening of each individual slip system. The usefulness of this non-uniform multiscale crystal plasticity model is then explored with respect to its ability to reproduce experimentally measured responses at different strain levels for different size grains.

Furthermore, a “Mantle-Core” type model which combines both the non-uniform material parameter model and the limited slip model is created, in which the majority of plastic deformation is accommodated near the grain boundary under multi-slip, and uniform plastic deformation occurs in the bulk dominated by double or triple slip. These models are compared for similar levels of hardening, and the pole figures that result from their deformation are compared to experimental pole figures.

While there are other models that can capture the heterogeneity introduced by mesoscale deformation at the grain scale, this combined top-down, bottom-up multiscale crystal plasticity model is by far one of the most computationally efficient as the heterogeneity of the mesoscale is does not emerge by introducing higher order terms, but rather by incorporating the heterogeneity into a simple crystal plasticity formulation. Therefore, as computational power increases, this approach will be among the first that will be able to perform accurate polycrystal level modeling while retaining the heterogeneity introduced by non-local mesoscale deformation mechanisms at the sub-grain scale.

CHAPTER 1: CRYSTAL PLASTICITY INTRODUCTION

While macroscale models can accurately predict the overall response of polycrystalline metals to externally applied loads or displacements, they fail to take into account information regarding the microstructure of the material. Therefore macroscale models are by construction unable to predict the response and evolution of the non-uniform deformation at the microstructure scale. Because every mechanism governing deformation at the individual grain scale is anisotropic, information about grain orientation and the mechanisms that govern the elastic-plastic response inside of the grain are needed in order to accurately model texture evolution, onset of plasticity, fatigue, and many other boundary value problems in metals.

Crystal plasticity theory was developed in order to take into account the heterogeneity of the microstructure, thus gaining information about the local deformation at the grain scale. Detailed modeling of a material's response at the grain scale is not necessary for applications where knowledge of the microstructure scale response are not paramount such as large scale component design without localized deformation or applications where large factors of safety are inconsequential to the overall design process. However, for applications such as texture evolution, stress localization at notches, component design which is close to the grain size, fretting fatigue, fatigue at stress localization from inclusions or voids, fracture, and superplastic forming, mesoscale information must be taken into account as it is the regime that controls the fundamental heterogeneity due to these localized responses.

Furthermore in the realm of design of new materials, the rate of computational power increase has seen an asymmetrically large rate of growth which has pushed

technology towards a more limited, targeted role for experimental investigation in developing new material systems. It follows that material design methods with the ability to incorporate computational models that complement experimental development materials approaches not only benefit from the decreased cost of computational modeling relative to experiments, but will also see increased growth due to computational speedup.

In order to realize the gains of using higher order computational models such as crystal plasticity, the model being used must accurately subsume the collective behavior of lower length scales it and pass this information into the deformation mechanisms which are modeled at the individual grain scale. This collective response is then put into a continuum framework and modeled using finite element analysis. Traditionally in crystal plasticity models, the material parameters are initially assumed to be uniform throughout the entire grain. In order to capture the net effect of microstructure evolution seen in micrographs which show that deformation inside of the grain can exhibit a variety of structures such as primary slip bands, cellular structures, and lamellar structures, hardening relations that are borrowed from macroplasticity such as isotropic and kinematic hardening are introduced. While this top-down methodology is useful and does an accurate job modeling the overall grain response, the mesoscale response inside of the grain is largely ignored. In order to address this issue experimental, analytical, and computational results of mesoscale deformation are examined, and reformulated in terms of a crystal plasticity model to create a combined top-down, bottom-up non-uniform crystal plasticity model.

In Chapter 2, the fundamental elements of plastic deformation along with theories that model the overall macroscopic behavior are introduced. Then, both macroscale and

crystal plasticity formulations are introduced, along with the evolution equations and how they pertain to the fundamental elements plastic deformation.

In Chapter 3, one of the fundamental assumptions of crystal plasticity theory, the Von Mises criterion that at least 5 independent plastic deformation sources must be active at each material point, is examined and the consequences of violating this assumption are explored. Doing so is entirely motivated by looking at experimental results of mesoscale plastic deformation and seeing that less than five slip systems are actually observed at each material point in most cases. From these results, a novel explanation for kinematic hardening is introduced, along with an explanation of how limiting the number of active slip systems can be used to drive subgrain rotation as seen in actual experiments.

Chapter 4 first presents the consequences that can arise from introducing a top-down crystal plasticity model, serving to motivate a length scale dependent, combined top-down, bottom-up crystal plasticity model that takes into account deformation mechanisms at the mesoscale by having parameters in the crystal plasticity evolution equations depend on the slip line length of each individual slip system inside of the grain. The heterogeneity provided by this model and the evolution equations introduced are then correlated with experimental data of tension tests in Ni at 77K, resulting in a very close fit for a variety of grain sizes at different strain levels.

Then, a “Mantle-Core” type model is introduced in order to combine both the non-uniform length-scale dependent model with the limited slip model, so that limited slip can be enforced in the grain interior which sees less compatibility requirements, and multiple slip is allowed near the grain boundary, which sees more compatibility requirements.

Chapter 5 restates the introduction and objective of this work, evaluates the results and contributions from Chapters 3 and 4, and then states both the novel contributions and recommended future work necessary to extend the impact and scope of this work.

CHAPTER 2: BACKGROUND INFORMATION AND MOTIVATION FOR CRYSTAL PLASTICITY MODELING

Facts of Plastic Deformation

Many theories have been created since the late 1800s that seek to either mathematically incorporate plasticity models into a framework that depends on a few measurable parameters which can then be used to predict the deformation of a material subjected to different loading conditions, or predict the physical mechanisms by which plastic deformation actually occurs. While many of these theories have been proposed, there are fundamental experimental observations that serve as a litmus test for any deformation theory.

Bridgman Experiments and Plasticity Incompressibility

In a series of experiments by Bridgman in 1947 and 1952, tensile tests were performed under extremely large hydrostatic pressures. Of the conclusions made, the two observations that a large hydrostatic pressure does not permanently change the volume of the material, and that the hydrostatic pressure has a negligible effect on yield strength, are fundamental underpinnings of classical plasticity theory (Khan 1995).

In terms of true strain, plastic incompressibility can be expressed as

$$\varepsilon_1^p + \varepsilon_2^p + \varepsilon_3^p = 0. \tag{2.1}$$

The consequences of this relation with respect to compatibility requirements, as first postulated by Von Mises, is that instead of needing six independent plastic deformation sources to satisfy any arbitrary plastic deformation via compatibility, the plastic

incompressibility requirement can be invoked so that only five independent sources of plastic deformation are required to satisfy plastic compatibility. In a crystal plasticity formulation considering only Schmid effects this translates into five independent slip systems are needed to require plastic incompressibility.

Bauschinger Effect

First observed by Bauschinger in 1886, the Bauschinger effect is the experimental observation that when a specimen is loaded in one direction then loaded in the reverse direction, the material yields at a reversed stress range greater than twice the original yield strength but less than the stress magnitude achieved in the prior loading branch. Figure 2.1 illustrates this concept, which is well known in textbooks (Khan 1995); (Yang 1993).

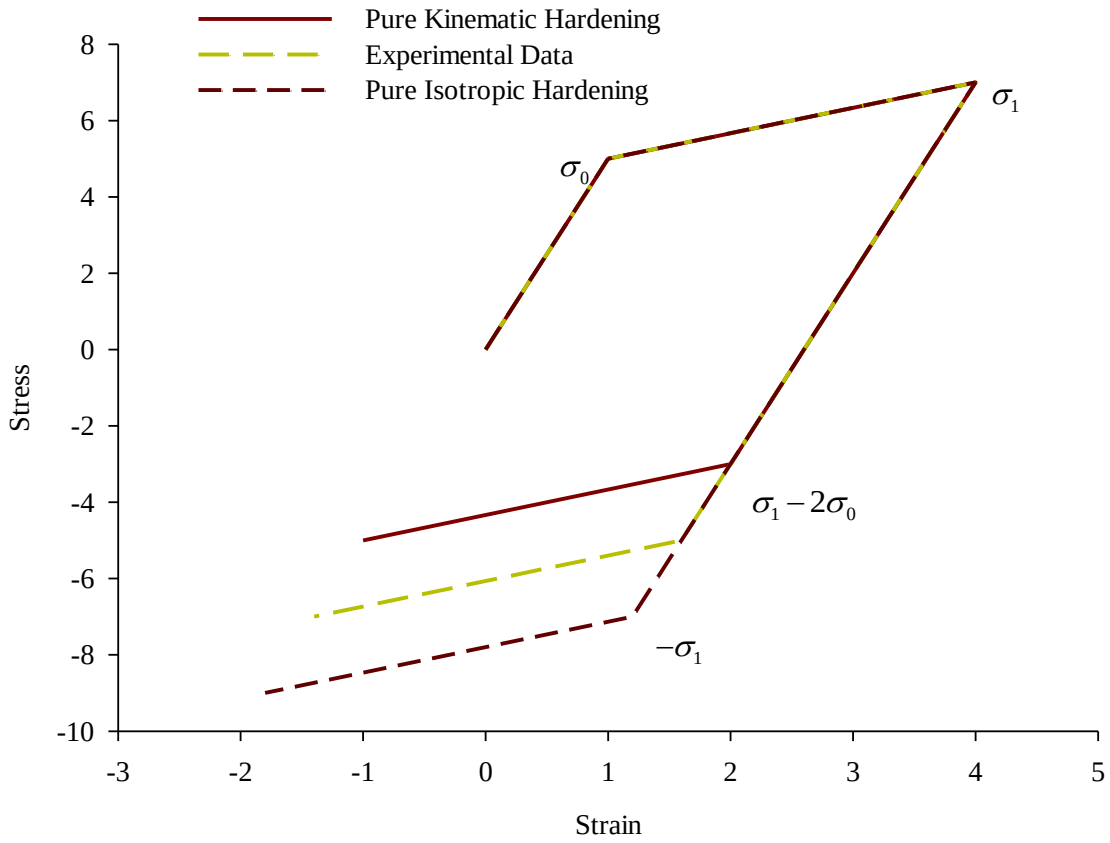

Figure 2.1. Idealized model illustrating the Bauschinger effect with respect to isotropic and kinematic hardening.

For pure metals, the Bauschinger effect is attributed to the change in dislocation substructure due to reversed loading, the aggregate change of the internal stress response of the system, and the interplay of intergranular interactions (Suresh 1991). In alloys, the Bauschinger effect is physically justified due to a combination of the forest hardening due to interaction of mobile dislocations with forest dislocations which is the mechanism behind isotropic hardening, and the mean internal stress exerted on the matrix by second phase particles, is responsible for the reversible back stress and corresponds to kinematic hardening.

Hall-Petch Relationship

The classical Hall-Petch relationship for initial yield strength stems from experimental observations that the initial yield strength of a polycrystal has an inverse square root relationship with the grain size, i.e.,

$$\sigma_y = \sigma_0 + \frac{k_y}{\sqrt{D}} \tag{2.2}$$

where σ_0 is the lattice friction stress required to move a dislocation in a single crystal, k_y is a material constant, and *D* is the grain diameter (Hall 1951); (Petch 1953). The Hall-Petch relationship for the onset of yielding holds for a large variety of materials; however, the exponent of the grain diameter ranges from 0.3-1.0, with an average reported exponent of 0.5, as seen through hardness measurements in Figure 2.2.

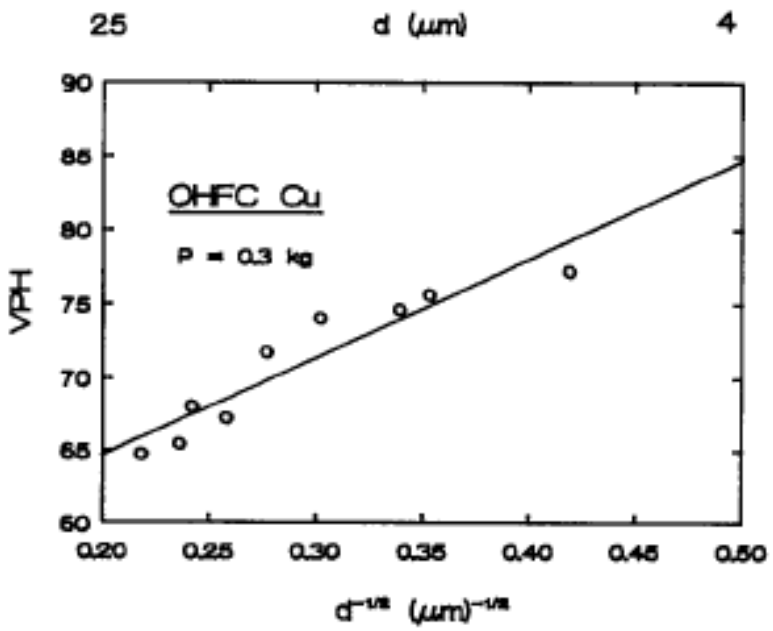

Figure 2.2. Classical Hall-Petch dependence of hardness on grain diameter reproduced from Chokshi et al. (1989).

While the classical Hall-Petch relation holds for grain sizes ranging from a few microns to several hundred microns, a breakdown in the Hall-Petch relation was first realized by Chokshi et al. (1989) for polycrystals with grain sizes on the order of tens to hundreds of nanometers as seen in Figure 2.3. There are many theoretical models used to explain the breakdown of the Hall-Petch relation which will be discussed later, but the fact remains that experimental observation shows that for different materials the classical initial yield strength dependence on grain size given by the Hall-Petch relation breaks down at the nanoscale.

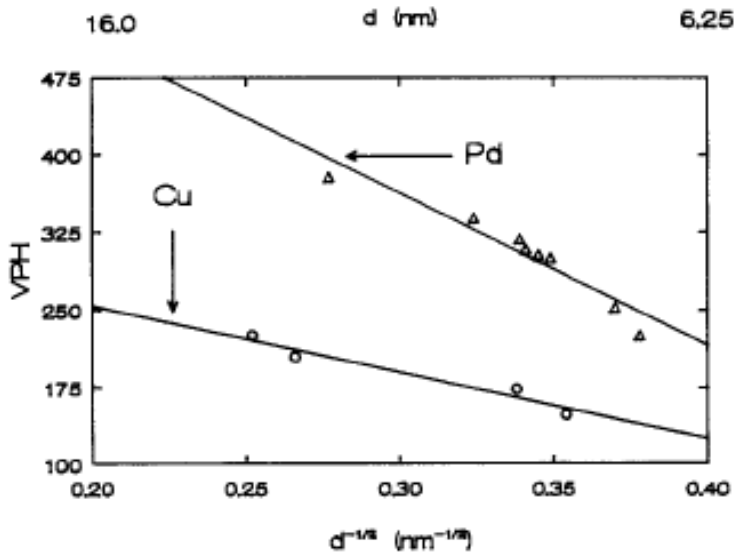

Figure 2.3. Inverse Hall-Petch dependence of hardness on grain diameter reproduced from Chokshi et al. (1989).

Single Crystal Behavior

Single crystal tests were first performed to understand the fundamental structure-property relations of crystalline materials. It was thought that a fundamental understanding of the deformation mechanisms and hardening behavior in single crystals would transfer directly to the behavior of polycrystals.

The experimental macroscopic stress-strain response of a single crystal, however, can vastly differ from that of a grain in a polycrystal. In this section, the macroscopic response of single crystals will be presented, and then in later sections, after the fundamental mechanisms of plasticity are introduced, the hardening behavior will be discussed in more detail.

The stress-strain response of single crystals exhibits three distinct phases, as seen from stress-strain curves shown in Figure 2.4 below.

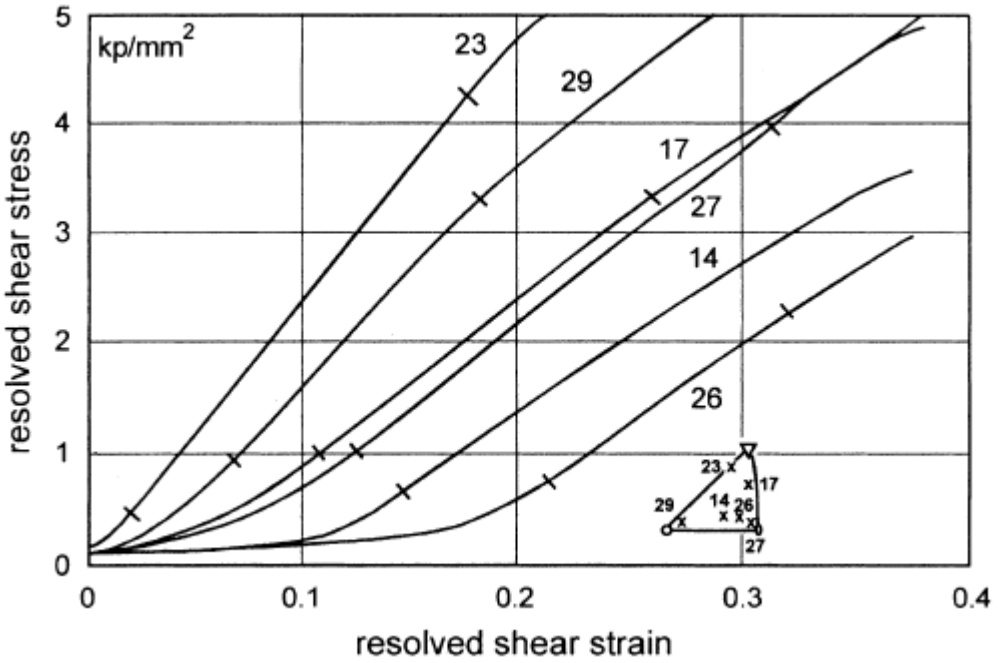

Figure 2.4. Stress-strain response of single crystal copper loaded in various orientations in quasi-static room-temperature loading conditions from Kocks and Mecking (2003).

The experimental Data in Figure 2.4 shows two distinct regions of hardening, the amount of strain for which each hardening region occurs, and how this amount depends on the crystal orientation. Stage I hardening is characterized by easy glide of dislocations, and exhibits little to no hardening and thus a slope of zero in the stress-strain response. Stage II hardening is characterized by a linear region with a strengthening ratio of approximately G / 300, where G is the shear modulus. The second stage of hardening is defined by the onset of secondary slip (Yang 1993). Stage III hardening is not present in Figure 2.4 due to the strains that the crystals were loaded to, but is portrayed in Figure 2.5. It is normally characterized by a saturation of the resolved shear stress with respect to the shear strain, and corresponds to a decreasing slope compared to Stage II linear hardening.

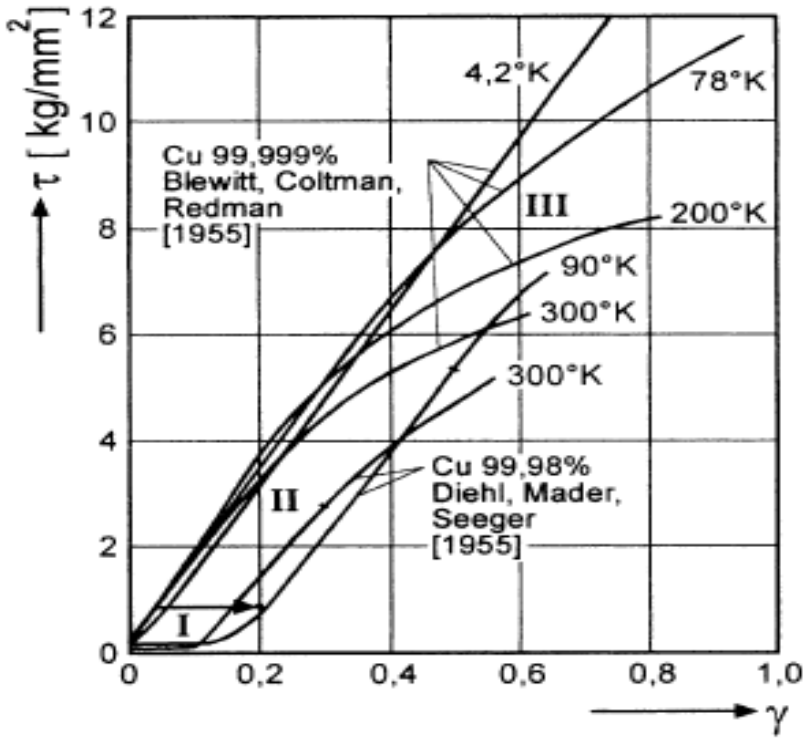

Figure 2.5. The three stages of hardening in single crystal copper at different temperatures from Kocks and Mecking (2003).

Plastic Deformation Mechanisms

Irreversible plastic deformation is a function of numerous mechanisms, and the importance of each depends on many variables. The most important variables that determine which plastic deformation mechanism is dominant are stress, strain rate, and temperature. The first attempt to identify these through experimental observation was done by Ashby (1972), and is presented in Figure 2.6 below for pure Nickel.

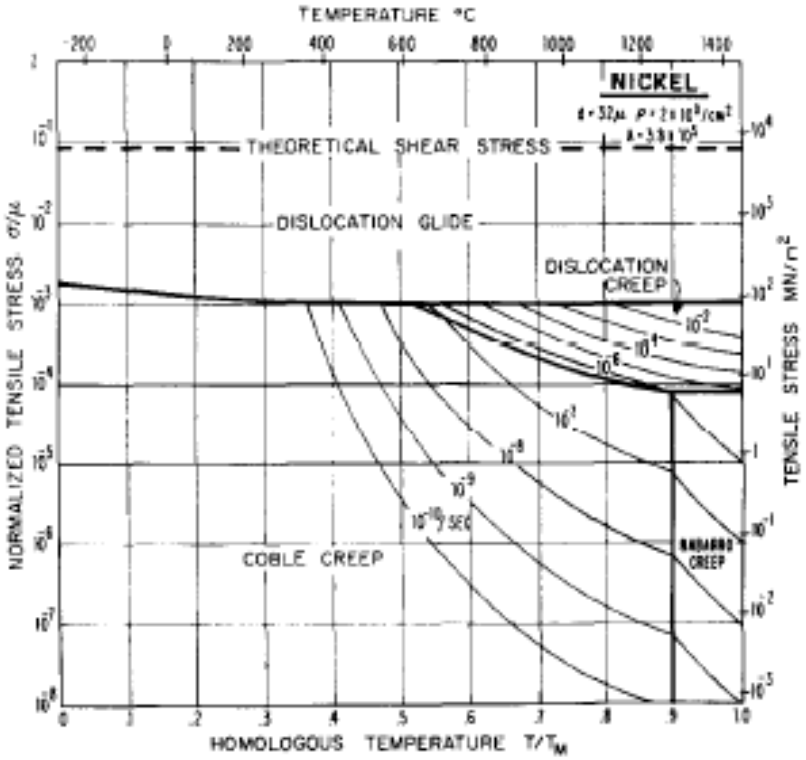

Figure 2.6. Deformation mechanism map for pure polycrystalline Ni from Ashby (1972).

For polycrystalline Ni, and for many other materials which can be found in the original or subsequent works on deformation mechanism maps, dislocation-mediated plasticity is the primary plastic deformation mechanism for a variety of tensile stresses regardless of strain rate or homologous temperature. Only at very low stresses does dislocation, Coble, or Nabarro creep become relevant phenomena. From this deformation map and observation of other deformation maps for other materials, it is apparent that dislocation mediated-plasticity is the primary mechanism for elastic-plastic deformation over a large range of service conditions, and therefore much attention is warranted to examine the dislocation glide-dominated regime.

Slip

The primary mechanism for plasticity at low to medium homologous temperatures under quasi-static loading is collective dislocation nucleation, interaction, and multiplication on specific crystallographic planes. Depending on the crystal structure, e.g., FCC, BCC, or HCP, different close packed planes will define the possible active slip systems on which dislocation glide can occur.

By resolving the stress onto the close packed slip plane defined by the slip direction s^{α} and slip normal m^{α} using *Schmid's Law* (Schmid 1924),

$$\boldsymbol{\tau}^{\alpha} = \mathbf{m}^{\alpha} \cdot \boldsymbol{\sigma} \cdot \mathbf{s}^{\alpha} \tag{2.3}$$

yields the resolved shear stress (RSS) acting on an individual slip system, which serves as the driving force for glide of dislocations on that individual slip system. The collective motion of dislocations due to the action of the RSS is governed by the Orowan equation which idealized the shear strain rate of like-signed dislocation lines on a slip plane as

$$\dot{\gamma} = \rho_d b v \tag{2.4}$$

where $\dot{\gamma}$ is the shearing rate, ρ_d is the dislocation line density, b is the magnitude of the Burgers vector, and v is the average dislocation speed.

Twinning

Deformation twinning is another mechanism in which the total volume of the material does not change but permanent deformation takes place (Yang 1993). Twinning is when a plane of atoms shear by a fixed magnitude parallel to the fixed twinning place so that the deformed lattice is symmetric about the plane as seen in Figure 2.7 in the two symmetric demarcated regions I and II. Deformation twinning in FCC metals is mainly

prevalent at high strain rates, low temperatures, or for very small grain sizes. All of these instances are cases in which dislocation migration is not an energetically favorable way to accommodate arbitrary deformation beyond initial yielding.

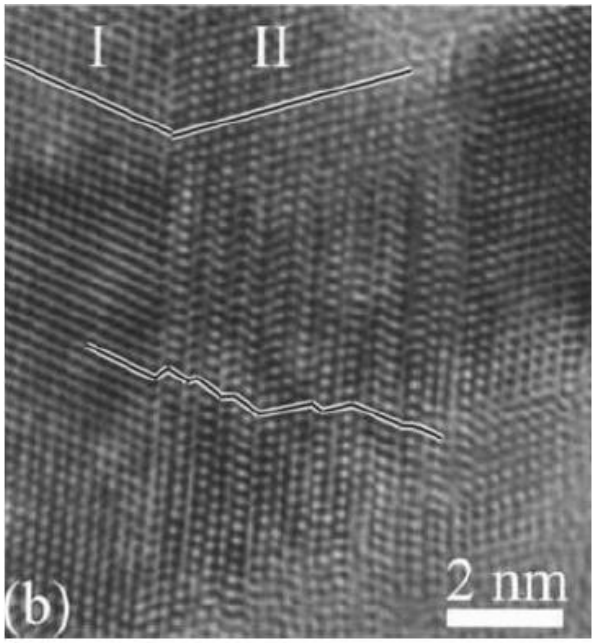

Figure 2.7. Deformation twins in nano-structured copper from Liao et al. (2004).

Grain Boundary Sliding

Grain boundary sliding is experimentally observed as another source of plastic deformation as it conserves the total volume yet causes permanent deformation. Grain boundary sliding initiates far from the triple junction, and, under certain sets of conditions which are highly material and temperature dependent, can cause large amounts of plastic deformation as seen in Figure 2.8 (Yang 1993).

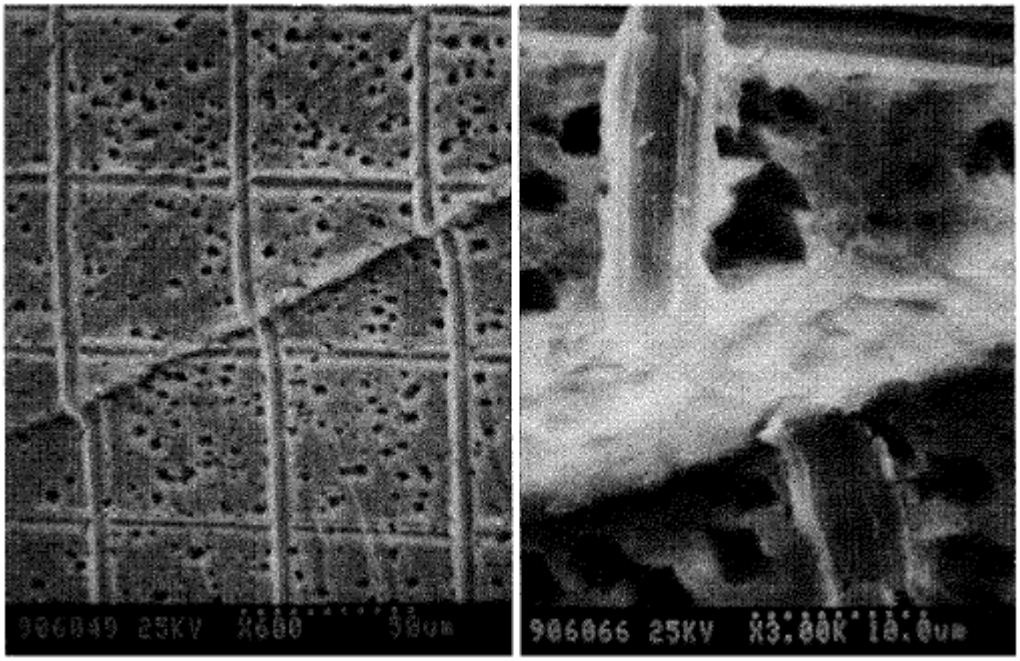

Figure 2.8. Illustration of grain boundary sliding on the left from an originally grid patterned material, and a close up of the shearing layer of the same material on the right from Yang (1993).

While it is not a significant source of plastic deformation at room temperature under quasi-static loading in most pure metals, it can accommodate some plastic deformation, which then eases the requirement of other plastic deformation sources, as is seen in Figure 2.9 where only single slip is observed.

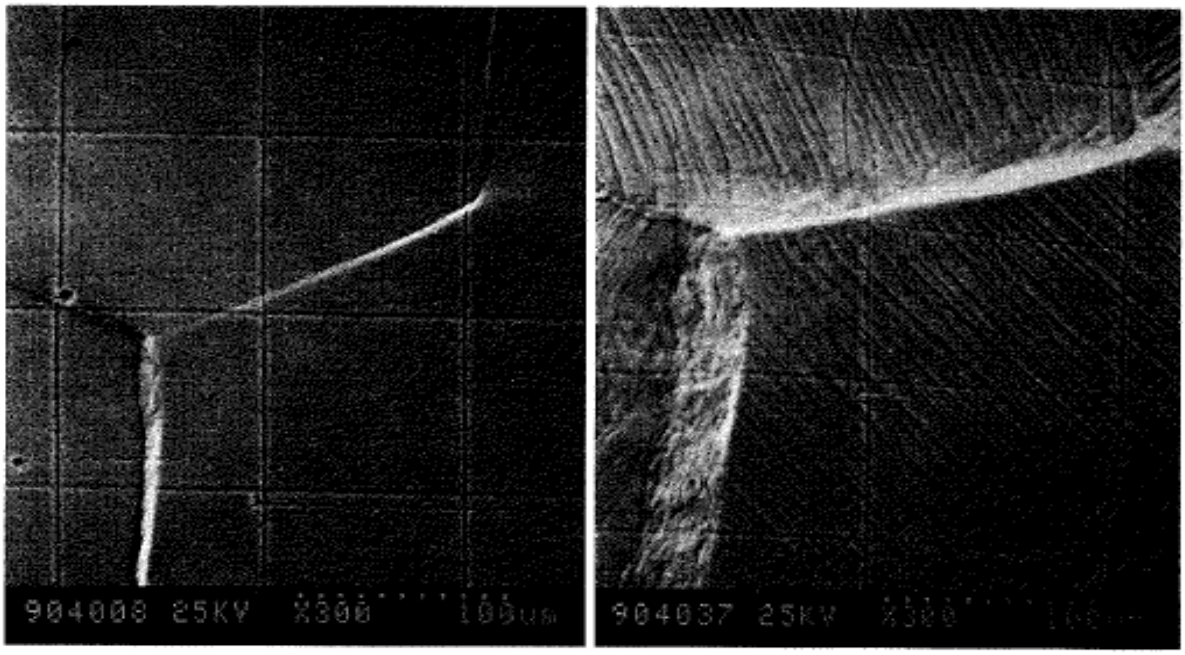

Figure 2.9 Out-of-plane grain boundary sliding of the same specimen at 1% strain on the left, and 35% strain on the right from Yang (1993). Note that only single slip is observed in right pane due to relaxed constraint on slip deformation due to grain boundary sliding.

Crystal Plasticity Theory

Since the first experimental works of Schmid (1924) and subsequently Taylor and Elam (1925), the modeling of single and polycrystalline deformation has enjoyed several advances. With sufficient experimental data on single crystal behavior, a single crystal theory was needed first, so that it could be generalized to the polycrystalline case. The lineage of the modern constitutive laws for slip-induced plasticity follows the works of Taylor (1938), Hill (1966), and Hill and Rice (1972), of which a comprehensive review can be found by Asaro (1983).

Because of the ever-increasing need to connect the response of metals to the physical mechanisms responsible for deformation, crystal plasticity theories are continually being refined in order to more accurately represent the response of different

materials at finer length scales. The basic foundation for crystal plasticity is presented next.

Crystalline Deformation Kinematics

A key to crystal plasticity theory which was verified experimentally at low strains is that as dislocations glided through the lattice they left the regular lattice of the crystal unperturbed. Therefore, deformation can be separated into two steps: plastic deformation mediated through dislocation glide, and elastic deformation of the unperturbed lattice.

The decomposition of the deformation gradient

$$\mathbf{F} = \mathbf{F}^{e} \cdot \mathbf{F}^{p}, \tag{2.5}$$

into elastic and plastic parts is a non-unique multiplicative decomposition of the deformation gradient. The physical meaning of this decomposition is more effectively illustrated in Figure 2.11, where $\mathbf{s}_0^{\alpha}$ and $\mathbf{m}_0^{\alpha}$ are the slip and slip normal directions respectively in the undeformed and intermediate configurations, and $\mathbf{s}^{\alpha}$ and $\mathbf{m}^{\alpha}$ are the slip and slip normal directions in the current configuration. Dislocation glide is mapped by $\mathbf{F}^{p}$ and the elastic stretch and rotation of the unperturbed lattice is mapped by $\mathbf{F}^{e}$. While this decomposition has a physical basis, calculation of $\mathbf{F}^{e}$ after calculation of $\mathbf{F}^{p}$ to find the total deformation gradient still remains a topic of interest owing to the heterogeneous deformation associated with populations of dislocations, see (Clayton and McDowell 2003).

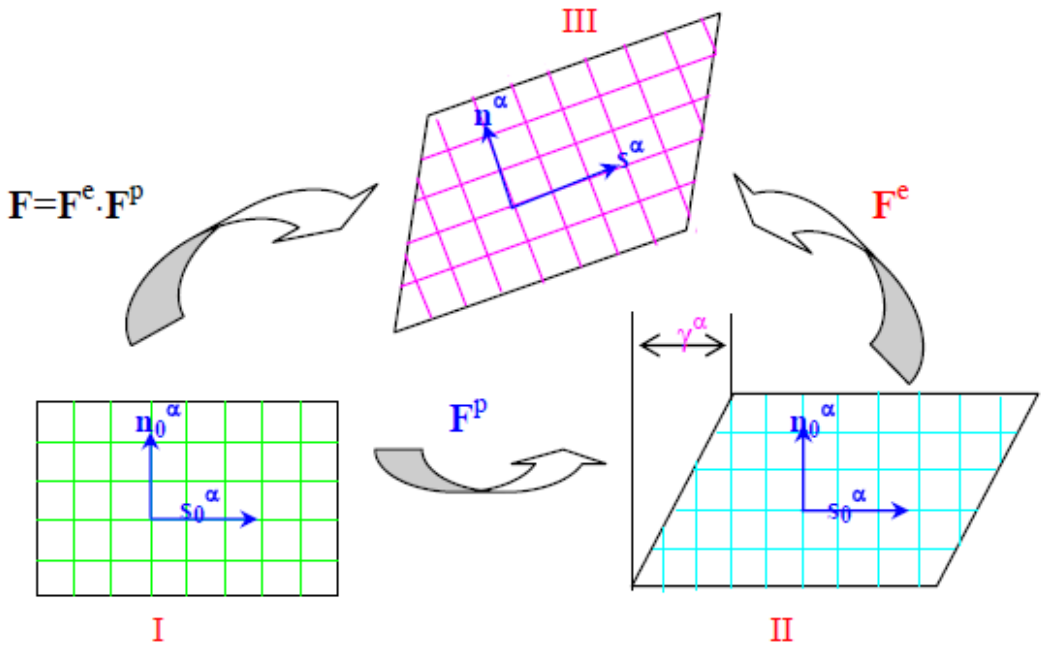

Figure 2.10. Decomposition of the deformation gradient from: I) Undeformed Configuration; II) The Intermediate Configuration; III) The Current Configuration from Mayeur (2004).

The slip plane direction $\mathbf{s}_0^\alpha$ is mapped from the intermediate to the current configuration by

$$\mathbf{s}^\alpha = \mathbf{F}^e \cdot \mathbf{s}_0^\alpha . \tag{2.6}$$

By requiring that the slip direction are normal in both the undeformed, intermediate, and current states, namely

$$\mathbf{s}_0^\alpha \cdot \mathbf{m}_0^\alpha = 0 = \mathbf{s}^\alpha \cdot \mathbf{m}^\alpha , \tag{2.7}$$

then the slip plane normal direction in the current configuration $\mathbf{m}^\alpha$ is found as

$$\mathbf{m}^\alpha = \left(\mathbf{F}^e\right)^{-1} \cdot \mathbf{m}_0^\alpha . \tag{2.8}$$

The connection from the non-local microscale to the continuum macroscale is made by assuming that the simple shear on each slip system is caused by dislocation

glide acting in the slip direction, which implies that the velocity gradient associated with each material point is

$$\mathbf{L}_0^p = \dot{\mathbf{F}}^p \cdot \left(\mathbf{F}^p\right)^{-1} = \sum_{\alpha=1}^{N} \dot{\gamma}^\alpha \left(\mathbf{s}_0^\alpha \otimes \mathbf{m}_0^\alpha\right) \tag{2.9}$$

where $\dot{\gamma}^\alpha$ is the rate of shearing on each slip system, and *N* is the total number of slip systems in the material (Peirce et al. 1983). Note that the dyad $\left(\mathbf{s}_0^\alpha \otimes \mathbf{m}_0^\alpha\right)$ is the Schmid tensor previously discussed in single crystal deformation (Schmid 1924). With the definition of the plastic part of the velocity gradient, the elastic part is therefore

$$\mathbf{L}^e = \mathbf{L} - \mathbf{F}^e \cdot \mathbf{L}_0^p \cdot \left(\mathbf{F}^e\right)^{-1} \tag{2.10}$$

where $\mathbf{L}$ is the velocity gradient in the current configuration defined by

$$\mathbf{L} = \dot{\mathbf{F}} \cdot \mathbf{F}^{-1}. \tag{2.11}$$

It is noted that the decomposition of the elastic and plastic parts of the deformation gradient into two distinct steps and defining the plastic part of the velocity gradient in the intermediate configuration as the sum of the shearing rates on each slip system implies that irreversible dislocation glide is solely responsible for shearing of the lattice, and that reversible elastic deformation is solely responsible for the stretch and rotation of the lattice. If non glide sources of plastic deformation are to be taken into account which do not correspond dislocation accumulation on the lattice, then the definition of the plastic part of the velocity gradient must be altered in a more general sense

$$\mathbf{L}_0^p = \sum_{\alpha=1}^{N} \dot{\gamma}^\alpha \left(\mathbf{s}_0^\alpha \otimes \mathbf{m}_0^\alpha\right) + \mathbf{f}\left(\psi\right) \tag{2.12}$$

where for this definition to make physical sense with respect to the two part decomposition of the deformation gradient, $\mathbf{f}(\psi)$ must not perturb the regular lattice as plastic deformation accumulates. Examples of effects that this general function could account for include grain boundary sliding, dislocation climb, or other sources of anelastic deformation.

Crystalline Deformation Kinetics

With the mathematical kinematic definitions for the elastic-plastic decomposition of crystalline deformation in place, what is left in order to define a complete theory of crystalline deformation that depends on dislocation glide is the constitutive relation that relates how the shearing rate on each slip system evolves with respect to an applied stress.

First, it must be noted that there is a separation between the constitutive relations for rate-dependent and rate-independent materials. Even though for most materials there exists a region which can be idealized as rate-independent region over several orders of magnitude of applied loading rates, all materials at finite temperatures have some effect of loading rates on their response. Therefore a generalized relation will be rate-dependent and subject to stress-induced thermal activation.

With this in mind, a generalized formulation for the shearing rate on each individual slip system due to dislocation glide is generally written as

$$\dot{\gamma}^{\alpha} = \mathbf{f}^{\alpha}\left(\frac{\left|\tau^{\alpha} - \chi^{\alpha}\right| - \kappa^{\alpha}}{\mathbf{D}^{\alpha}}\right)\mathbf{sgn}\left(\tau^{\alpha} - \chi^{\alpha}\right) \tag{2.13}$$

where α represents each slip system, $\boldsymbol{\tau}^{\alpha}$ is the resolved shear stress (RSS), $\boldsymbol{\chi}^{\alpha}$ is the back stress, $\boldsymbol{\kappa}^{\alpha}$ is the threshold stress, $\mathbf{D}^{\alpha}$ is the drag stress, and $\mathbf{f}^{\alpha}$ is a general function which can depend on any number of constants. The interpretation and evolution equations for the back stress, threshold stress, and drag stress will be discussed later, but first the RSS must be defined.

Manipulation of the elastic-plastic decomposition of the deformation gradient gives

$$\mathbf{F}^{\mathbf{e}} = \mathbf{F}^{\mathbf{p}} \cdot \mathbf{F}^{-\mathbf{1}}. \tag{2.14}$$

From this, the St. Venant's elastic green strain can be calculated

$$\mathbf{E}^{\mathbf{e}} = \left(\mathbf{F}^{\mathbf{e}}\right)^{\mathbf{T}} \cdot \mathbf{F} - \mathbf{I} \tag{2.15}$$

which can then be used along with the 4th order elastic stiffness tensor ${}^{\mathbf{4}}\mathbf{C}$ to arrive at the 2nd Piola-Kirchhoff stress in the intermediate configuration, i.e.,

$$\boldsymbol{\sigma}^{\mathbf{PK2}} = {}^{\mathbf{4}}\mathbf{C} : \mathbf{E}^{\mathbf{e}}. \tag{2.16}$$

By mapping $\boldsymbol{\sigma}^{\mathbf{PK2}}$ to the current configuration using the elastic deformation gradient, the Cauchy Stress is found as

$$\boldsymbol{\sigma} = \frac{\mathbf{1}}{\mathbf{det}\left(\mathbf{F}^{\mathbf{e}}\right)} \cdot \mathbf{F}^{\mathbf{e}} \cdot \boldsymbol{\sigma}^{\mathbf{PK2}} \cdot \left(\mathbf{F}^{\mathbf{e}}\right)^{\mathbf{T}}. \tag{2.17}$$

In order to calculate the RSS, the 2nd Piola-Kirchhoff Stress is used because it is the stress in the intermediate configuration. Therefore, from the RSS acting on each slip system is

$$\boldsymbol{\tau}^{\alpha} = \boldsymbol{\sigma}^{\mathbf{PK2}} : \left(\mathbf{s}_{\mathbf{0}}^{\alpha} \otimes \mathbf{m}_{\mathbf{0}}^{\alpha}\right). \tag{2.18}$$

From the resolved shear stress in the intermediate configuration, the slip rate on each slip system is evaluated through the flow rule.

Numerical Integration Approaches

Because the derivation for the RSS hinges on the fact that the deformation gradient in the current configuration is specific at each increment in displacement-based finite element approximations, iterative numerical methods must be used to solve the boundary value problem. There are two general methods which can be used in order to find the elastic-plastic response for a given deformation path: implicit or explicit integration schemes.

In implicit integration schemes the solution to the set of finite element equations is iterated towards until a convergence criterion is satisfied for that increment; therefore, inversion of the global stiffness matrix must be performed. Explicit integration directly solves for displacements at the next time step by assuming constant velocity and acceleration over a small time step. Because the equations are highly non-linear in a crystal plasticity framework, the appropriate method can greatly depend on the goal and loading conditions of the simulation (Harewood and McHugh 2007). For a thorough review of these different schemes along with their implications on rate of convergence of the solution when applied to baseline problems consult (Ling et al. 2005) or any number of textbooks or papers on finite element schemes.

The integration scheme used in this work is a fully implicit backward Euler integration scheme by R.D. McGinty explained in further detail in (McGinty 2001). It is noted that this scheme follows the original work of Cuitino and Ortiz (1992).

Hardening Relationships in Rate-Dependent Crystalline Deformation

In macroscopic rate-independent incremental plasticity theories, a constitutive relation must be defined such that an increment in strain outside of the yield surface corresponds to an increment of stress such as

$$\mathbf{d\sigma} = {}^{4}\mathbf{C}^{ep} : \mathbf{d\varepsilon} \tag{2.19}$$

where ${}^{4}\mathbf{C}^{ep}$ is the incremental elastic-plastic stiffness tensor and can either be constant or can evolve with plastic deformation.

As in rate-independent macroplasticity, a relation must be introduced for rate-dependent response of dislocation glide on each slip system. A specific form of the general equation from (Mayeur 2004) is

$$\dot{\boldsymbol{\gamma}}^{\alpha} = \dot{\gamma}_0 \left\langle \frac{\left|\boldsymbol{\tau}^{\alpha} - \boldsymbol{\chi}^{\alpha}\right| - \boldsymbol{\kappa}^{\alpha}}{\mathbf{D}^{\alpha}} \right\rangle^{\mathbf{m}} \mathbf{sgn}\left(\boldsymbol{\tau}^{\alpha} - \boldsymbol{\chi}^{\alpha}\right) \quad , \quad \begin{matrix} \langle \mathrm{x} \rangle = 0 \ \text{ if } \ \mathrm{x} < 0 \\ \langle \mathrm{x} \rangle = \mathrm{x} \ \text{ if } \ \mathrm{x} \geq 0 \end{matrix} \tag{2.20}$$

where $\dot{\gamma}_0$ is the reference shearing rate, *m* is the strain rate sensitivity, and the other variables have been previously defined. Note as $m \to \infty$ the rate-dependent formulation is equivalent to a rate-independent framework.

Infinitely many forms of hardening laws can exist, and attempts to use them to model the evolution of the elastic-plastic response of crystals dates to works done on single crystal experiments. Effective hardening relations parameterize the fundamental hardening mechanisms that dominate deformation at the mesoscale. A review of many of these fundamental mechanisms are reviewed by Arzt (1998). Recent attempts to use hardening to model the evolution of the microstructure of crystalline materials generally follow the form

$$\dot{\mathbf{D}}^{\alpha} = \sum_{\beta=1}^{N} \left(H_{DIR} \mathbf{h}_{\mathbf{D}}^{\alpha\beta} - H_{DYN} \mathbf{D}^{\alpha} \right) \left| \dot{\gamma}^{\beta} \right| \tag{2.21}$$

for the evolution of the drag stress,

$$\dot{\boldsymbol{\chi}}^{\alpha} = A_{DIR} \dot{\boldsymbol{\gamma}}^{\alpha} - A_{DYN} \boldsymbol{\chi}^{\alpha} \left| \dot{\gamma}^{\alpha} \right| \tag{2.22}$$

for the evolution of the back stress, and

$$\dot{\boldsymbol{\kappa}}^{\alpha} = \sum_{\beta=1}^{N} \left(T_{DIR} \mathbf{h}_{\boldsymbol{\kappa}}^{\alpha\beta} - T_{DYN} \boldsymbol{\kappa}^{\alpha} \right) \left| \dot{\gamma}^{\beta} \right| \tag{2.23}$$

for the evolution of the threshold stress.

For the evolution of the drag stress $\dot{\mathbf{D}}^{\alpha}$, much attention has been devoted to the hardening matrix $\mathbf{h}_{\mathbf{D}}^{\alpha\beta}$, which contains the effects of hardening of each slip system with respect to slip on this system (self-hardening $\mathbf{h}_{\mathbf{D}}^{\alpha\alpha}$) and slip on other slip systems (latent hardening $\mathbf{h}_{\mathbf{D}}^{\alpha\neq\beta}$) (Bassani and Wu 1991). Values for the self-hardening of $\mathbf{h}_{\mathbf{D}}^{\alpha\beta}$ are usually assumed to be equal to one, but values for the off-diagonal terms of $\mathbf{h}_{\mathbf{D}}^{\alpha\beta}$ can be found in literature to range from zero for no latent hardening effect to values greater than one for slip systems that harden other systems more than the primary slip system. The simple case of only one active slip system shows that $\mathbf{D}^{\alpha}$ will eventually saturate to

$$D = \frac{H_{DIR}}{H_{DYN}} \tag{2.24}$$

if self-hardening is assumed to be unity and only one slip system is active.

As is seen in the evolution equation for the drag stress, there is no sign associated with a change in plastic strain. Therefore, if the drag stress has not reached its saturation value, then any increment in plastic deformation will cause an increase in the drag stress

for hardening behavior, or a directionless decrease in drag stress for softening behavior. This lack of sign will be a stark contrast to the behavior of the back stress.

The physical motivation of the drag stress is intrinsically tied to the evolution equations associated with it and the threshold stress. Because both of these terms cause an isotropic increase in the yield surface at the slip system level, they can be used to model similar phenomena. For example, if a non-evolving drag stress is assumed with an evolving threshold stress, the drag stress physically represents the effective dislocation force-velocity, and the threshold stress represents the energy penalty introduced by the long-range stress fields from forest dislocations throughout the grain. Therefore, the threshold stress corresponds to the directionless isotropic hardening at the slip system level due to the energy associated with the introduction of more dislocations. However, if only a drag stress is assumed and no threshold stress is introduced, the drag stress must correspond to both the energy penalty needed to introduce more dislocations due to the long-range stress fields and the effective dislocation force-velocity will be tied to the evolution equation of the drag stress. In the low strain rate sensitivity regime, a formulation using either a non-evolving drag stress and a threshold stress is equivalent to a formulation using an evolving drag stress with no self-hardening, and no threshold stress. While physical mechanisms may be assigned to these variables, the actual mechanisms they represent are tied to the definition of their evolution.

The evolution of the back stress is different from the drag stress and threshold stress in that it corresponds to a directional change in the plastic strain, and therefore makes it akin to kinematic hardening in macroplasticity. The overarching physical motivation for the back stress is the dislocation substructure's contribution to the

directional dislocation resistance (Mughrabi 1983); (Horstemeyer et al. 1999). Physically, McDowell (2008) explains that the back stress is due to actions at multiple length scales: the anelastic bowing of dislocations in cell structures from tens of nanometers; the disruption of the mean free path from dislocation anisotropy up to around 1μm; the creation of arrays of dislocations with net burgers vectors from pile-ups against grain boundaries or walls; and the differential yielding of grains with textured orientation distributions. All of these mechanisms are responsible, at different length scales, for the inability of inelastic deformations in one direction to be fully enforced in the reverse direction, as is the case with isotropic hardening.

Finite Element Implementation

The simulation of the finite-deformation rate-dependent crystal plasticity model is made possible by incorporation into the commercial finite element program Abaqus (Abaqus 2006) via a User MATerial subroutine, termed UMAT. A thorough discussion of the role of UMATs and their incorporation into Abaqus is presented in (McGinty 2001). The basic premise is that the finite element code input specifies the deformation gradient at the end of the time step, which is fed into the UMAT, which then calculates the tangent stiffness matrix. The tangent stiffness matrix is calculated using the crystal plasticity constitutive relations, and is fed back into Abaqus to check for global equilibrium at every node. If equilibrium is achieved below a specified tolerance, the deformation at the next time step can be calculated, and if not, then the time step is reduced. This process continues until the total deformation originally specified by the finite element model is complete for a given temperature.

CHAPTER 3: LIMITED SLIP CRYSTAL PLASTICITY MOTIVATION, FORMULATION, AND PARAMETRIC STUDY

Motivation

In most crystal plasticity formulations implemented into Finite Element schemes, displacement-based shape functions are used in order to ensure that displacements at all of the nodes are compatible. Rate-dependent crystal plasticity formulations assume that all of the slip systems can be active at each material point, which could result in up to 12 slip systems being simultaneously active.

To this point, there has not been a comprehensive parametric crystal plasticity study that examines the consequence of limiting the number of active slip systems that can occur at each material point on the macroscopic stress-strain response in single crystals and polycrystals. Before the formulation and results are presented, experimental motivation for a limited slip crystal plasticity formulation will be presented.

Experimental Evidence of Limited Slip

Numerous experimental and numerical efforts have been made in order to understand the consequence of dislocation substructure formation on the work hardening rate exhibited by a material. In FCC metals with low to medium stacking fault energies such as Cu, Ni, and Al, dislocations cooperate to create a network of low to medium angle sub-grain boundaries. There are different terminologies associated with cellular structure formations, but some of the most common are Dense Dislocation Walls (DDWs), Geometrically Necessary Boundaries (GNBs) (Hughes et al. 1998), Cell Blocks

(CBs) (Hughes et al. 1998), and Low Energy Dislocation Structures (LEDS) (Kuhlmann-Wilsdorf and Hansen 1991).

Regardless of nomenclature, there is experimental evidence that after stages of easy glide and single slip occur in the early stages of single crystal deformation, or after initial yielding in polycrystals, the substructure inside each grain evolves with increasing applied stress or strain. Not only does the substructure evolve, but at each material point inside of the grain, there are not actually five slip systems simultaneously active, but at most two or three (Kuhlmann-Wilsdorf 1998).

Mughrabi conducted tensile tests on single crystal OFHC Cu and observed the evolution of the microstructure from an initially stress-free configuration with few dislocations to a cellular structure as deformation progresses, as seen in Figure 3.1.

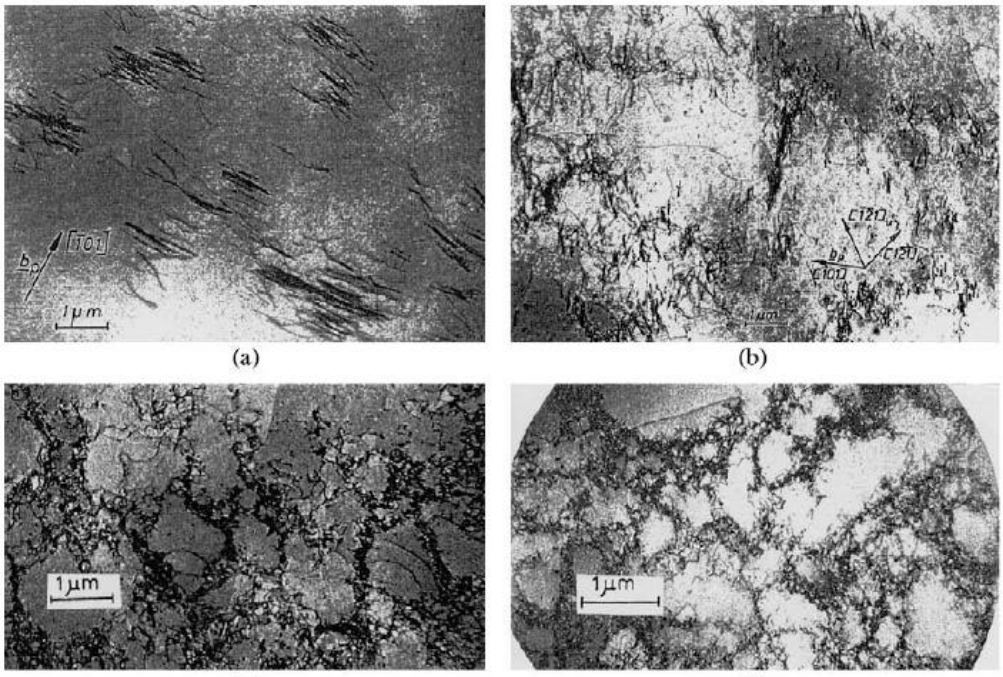

Figure 3.1. Single crystal tensile deformation at Room Temperature at a) 1.1 MPa b) 14 MPa c) 28 MPa d) 69 MPa from Kocks and Mecking (2003) reproduced from Mughrabi (1971).

Further experimental evidence of substructure formation is offered by Kawasaki and Takeuchi for single crystal tensile deformation of copper at both extremely low and elevated temperatures below. Cellular structures are observed at sufficiently high strain levels for single crystal monotonic deformation.

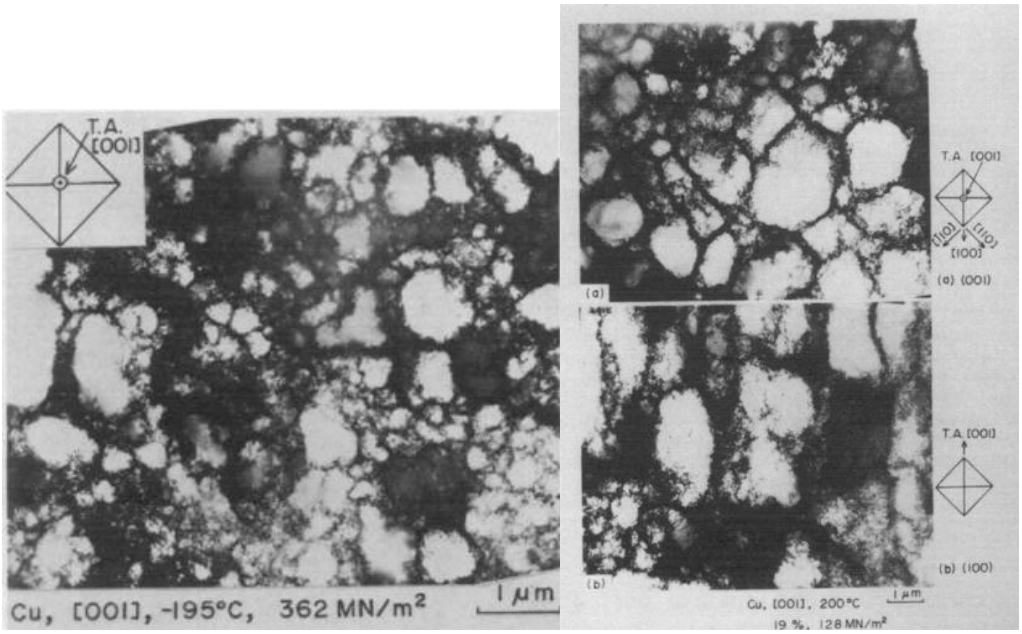

Figure 3.2. Cell structure formation in tensile deformation of Cu single crystals at 362 MPa and -195 C on the left and 128 MPa stress and 200 C on the right from Kawasaki and Takeuchi (1980).

In polycrystalline deformation, the same sort of cellular structures form at a variety of temperatures and strain levels for Cu. Pictures from (Kocks and Mecking 2003) show that for polycrystalline Cu deformed at different temperatures and different strain levels but at the same strain hardening rate, similar substructures are formed regardless of the varying temperatures and strain levels.

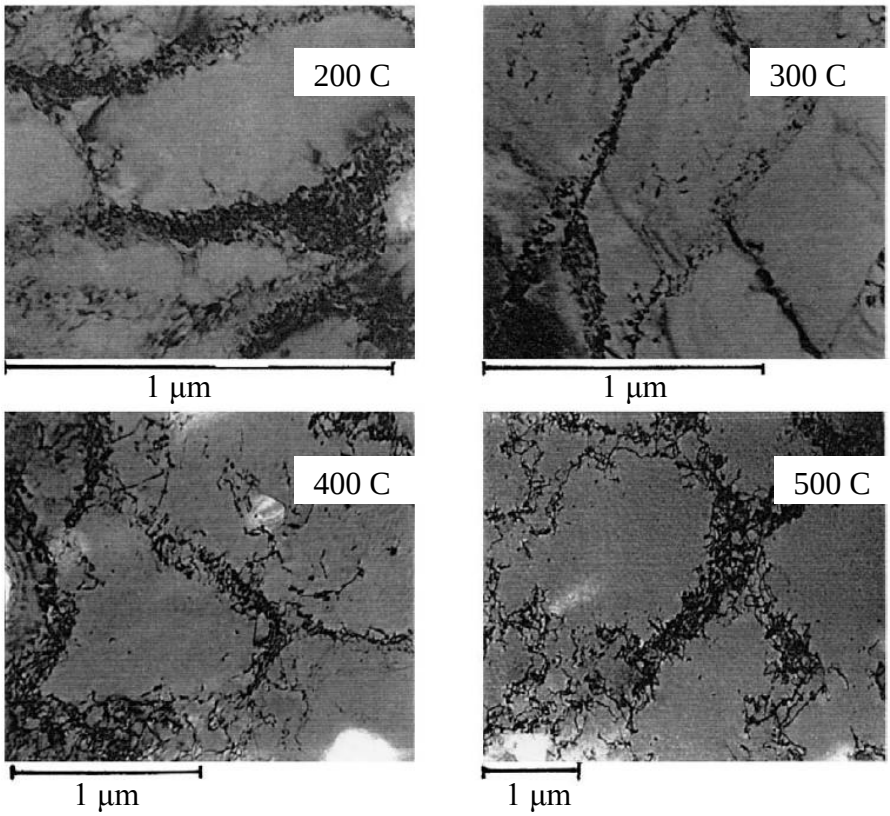

Figure 3.3. Polycrystalline OFHC Cu deformed to equivalent strain hardening rates at different temperatures from Kocks and Mecking (2003).

Further straining of polycrystalline Cu results in progressively more well-defined dislocation substructure formation. In a series of micrographs showing experiments on deep rolling of OFHC Cu with an initial grain diameter of 93 μm, Leffers showed the result of large straining on the substructure evolution.

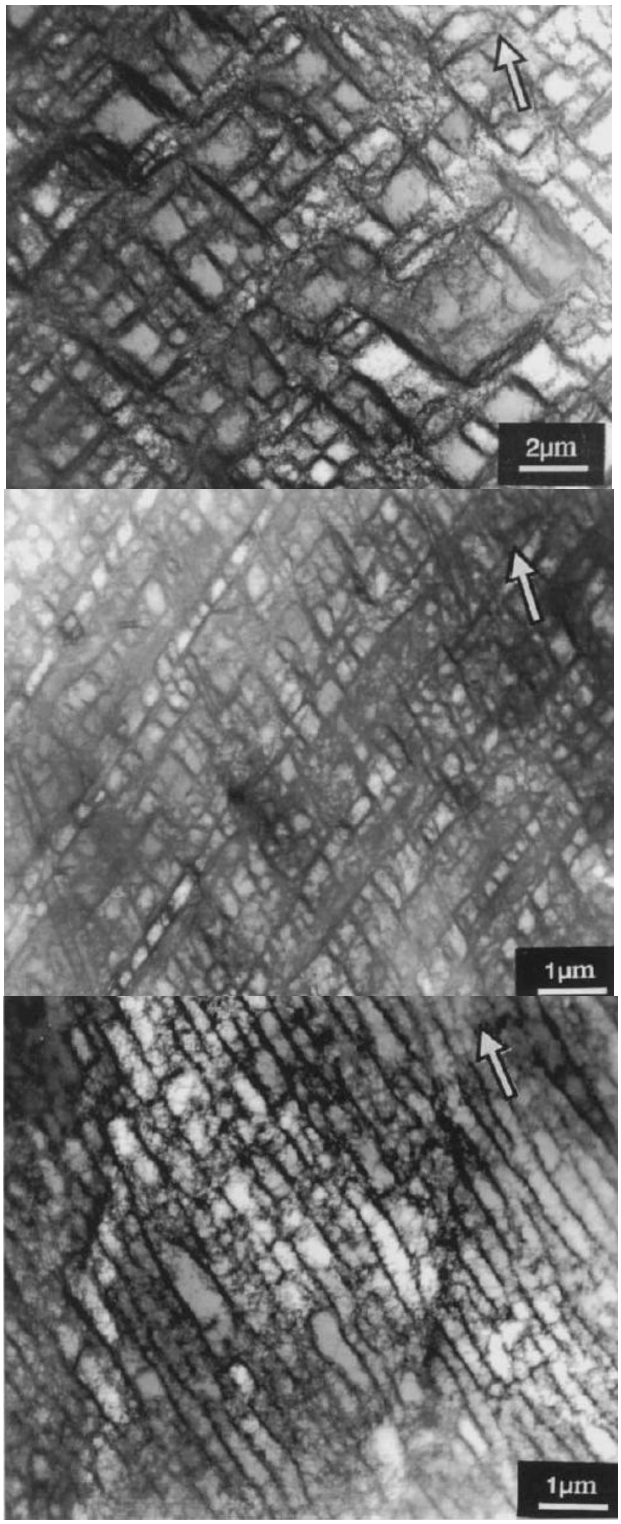

Figure 3.4. Large rolling deformation of polycrystalline Cu with initial grain size 93 μm, from top to bottom at 10%, 30%, and 39% reduction respectively from Christoffersen and Leffers (1998). The arrow indicates the rolling direction.

Not only is dislocation substructure formation prevalent in single and polycrystalline Cu, but it is also prevalent in other FCC pure metals with low to medium stacking fault energies such as Ni and Al, as evidenced in Figure 3.5 below.

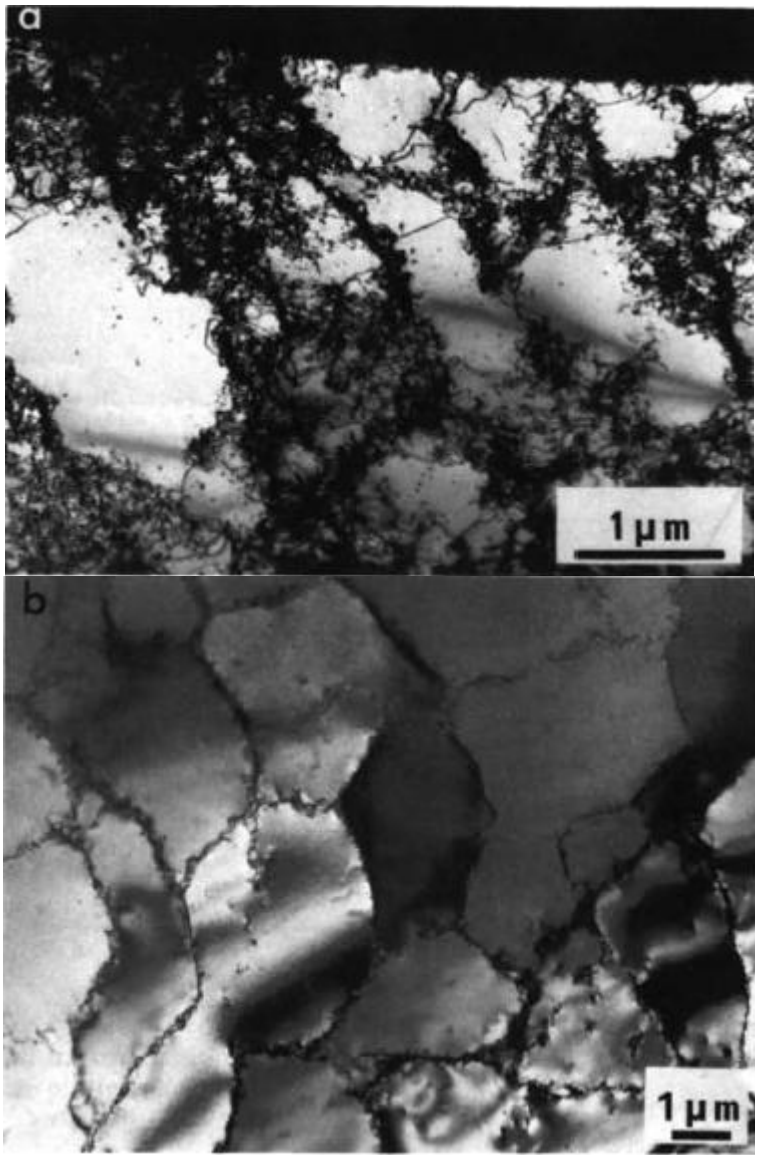

Figure 3.5. Dislocation substructure at 10% true strain in tension for a) Polycrystalline Ni and b) Polycrystalline Al from Barker et al. (1989).

Clearly, for single or polycrystalline FCC pure metals with low to medium stacking fault energy over a large range of temperatures, dislocation substructure formation is prevalent as straining continues. Also, from viewing the previous micrographs, there are not 5 slip systems active at each material point, as would be required from incompressibility applied to the compatibility condition. Instead, what is seen is a network less than 5 active slip systems active at each point combined with relatively dislocation-free areas, which cooperate as a network to accommodate plastic strain.

In crystal plasticity, the goal is to model the physical mechanisms responsible for elastic-plastic deformation. We will look at the consequences of creating a limited-slip model that does not admit five or more active slip systems at each material point. This parametric study of the limited slip model will explore the macroscopic stress-strain consequences on the assumption that fewer than 5 slip systems are active at each material point, which is the case as seen in actual experiments on FCC pure metals with low to medium stacking fault energy.

Single Slip Crystal Plasticity Formulation

A more specific version of the generalized crystal plasticity formulation is used in the following parametric study, and the derivation can be followed fully from R. D. McGinty's PhD thesis (McGinty 2001). In this formulation, the threshold stress κ and a back stress χ are both set to zero for each slip system, and the only evolving part of the formulation comes from the evolving drag stress for each slip system.

The physical justification for the drag stress was introduced in the previous section as the lattice resistance to dislocation motion; however, in the low strain rate

sensitivity regime (large strain rate sensitivity exponent *m*), the numerical implementation of an evolving drag stress or evolving stress are equivalent. Therefore, the drag stress formulation used herein effectively models the threshold stress and subsequent hardening due to forest dislocations. The strain rate sensitivity on each slip system α is

$$\dot{\boldsymbol{\gamma}}^{\boldsymbol{\alpha}} = \dot{\gamma}_0 \left(\frac{\left| \boldsymbol{\tau}^{\boldsymbol{\alpha}} \right|}{\mathbf{D}^{\boldsymbol{\alpha}}} \right)^m \mathbf{sgn}\left(\boldsymbol{\tau}^{\boldsymbol{\alpha}} \right). \tag{3.1}$$

Numerically the ability for a slip system to become active in this crystal plasticity formulation is associated with $\boldsymbol{\tau}^{\boldsymbol{\alpha}}$ exceeding $\mathbf{D}^{\boldsymbol{\alpha}}$. A limited slip formulation can be achieved by assigning a slip system as able to accumulate plastic slip by artificially inflating $\mathbf{D}^{\boldsymbol{\alpha}}$ until a specified fraction of the threshold stress is reached, at which time $\mathbf{D}^{\boldsymbol{\alpha}}$ is reassigned back to $\mathbf{D}_{\mathbf{0}}^{\boldsymbol{\alpha}}$. This is represented as

If slip system is already active:
$\mathbf{D}^{\boldsymbol{\alpha}}$ does not change
Otherwise: (3.2)
$\mathbf{D}^{\boldsymbol{\alpha}} = \mathbf{D}_{\infty}^{\boldsymbol{\alpha}}$ if $\left| \boldsymbol{\tau}^{\boldsymbol{\alpha}} \right| < \boldsymbol{\eta}^{\boldsymbol{\alpha}}$ or $N_{active} \geq N_{max}$
$\mathbf{D}^{\boldsymbol{\alpha}} = \mathbf{D}_{\mathbf{0}}^{\boldsymbol{\alpha}}$ if $\left| \boldsymbol{\tau}^{\boldsymbol{\alpha}} \right| \geq \boldsymbol{\eta}^{\boldsymbol{\alpha}}$ and $N_{active} < N_{max}$

where $\boldsymbol{\eta}^{\boldsymbol{\alpha}}$ is the threshold stress for the α^{th} slip system, N_{active} is the number of currently active slip systems, and N_{max} is the maximum number of slip systems that can be active at that point. Once a slip system becomes active, it is assumed to be active throughout the course of deformation even though it may only accumulate negligible slip.

The definition of the threshold stress $\boldsymbol{\eta}^{\boldsymbol{\alpha}}$ is non-trivial as it must be a fraction of the actual threshold drag stress represented by $\mathbf{D}_{\mathbf{0}}^{\boldsymbol{\alpha}}$ such that

$$\boldsymbol{\eta}^{\boldsymbol{\alpha}} = \lambda \mathbf{D}_{\mathbf{0}}^{\boldsymbol{\alpha}} \tag{3.3}$$

where $\lambda < 1$ and depends the reference shearing rate, strain rate-sensitivity exponent, and minimum error δ for which equilibrium can be satisfied in the numerical implementation. The difference between the drag stress implementation with an artificially inflated drag stress and the original drag stress implementation must be below δ, i.e.,

$$f(\lambda, m, \dot{\gamma}_0) - f(\mathbf{D}_{\mathbf{0}}^{\boldsymbol{\alpha}}, m, \dot{\gamma}_0) \leq \delta \tag{3.4}$$

where δ can be very small for implicit integration algorithms. For the cases in this parametric study done in the rate-independent regime which corresponds to a large strain rate sensitivity, $\lambda = 0.90$ has been used and has not led to finite element convergence issues. Regimes with a lower strain rate sensitivity exponent or smaller minimum error in the numerical scheme implemented would necessitate a lower λ.

The evolution of the hardening of the drag stress on each system $\mathbf{D}^{\boldsymbol{\alpha}}$ will assume two forms, namely

$$\dot{\mathbf{D}}^{\boldsymbol{\alpha}} = H_{DIR} \left| \dot{\boldsymbol{\gamma}}^{\boldsymbol{\alpha}} \right| \tag{3.5}$$

in which hardening is linear with respect to shearing rate,

$$\dot{\mathbf{D}}^{\boldsymbol{\alpha}} = H_{DIR} \left| \dot{\boldsymbol{\gamma}}^{\boldsymbol{\alpha}} \right| - H_{DYN} \cdot \mathbf{D}^{\boldsymbol{\alpha}} \sum_{\boldsymbol{\beta}=1}^{N} \left| \dot{\boldsymbol{\gamma}}^{\boldsymbol{\beta}} \right| \tag{3.6}$$

in which hardening does eventually saturate by direct hardening and dynamic recovery. Both of these equations are specific forms of the generalized crystal plasticity formulation in which the latent hardening matrix is assumed to be the identity matrix, i.e., $\mathbf{h}_{\mathbf{D}}^{\boldsymbol{\alpha\beta}} = \boldsymbol{\delta}_{\boldsymbol{\alpha\beta}}$.

Finite Element Model for Single Crystal Deformation

The following finite element models all consist of uniaxial tension and compression simulations using crystal plasticity code implemented into an Abaqus UMAT. For single crystal deformation, two different constraints are used. The "unconstrained" case, seen in Figure 3.6, consists of a single crystal represented by one cubic C3D8R Abaqus element where the faces are allowed to transverse and contract.

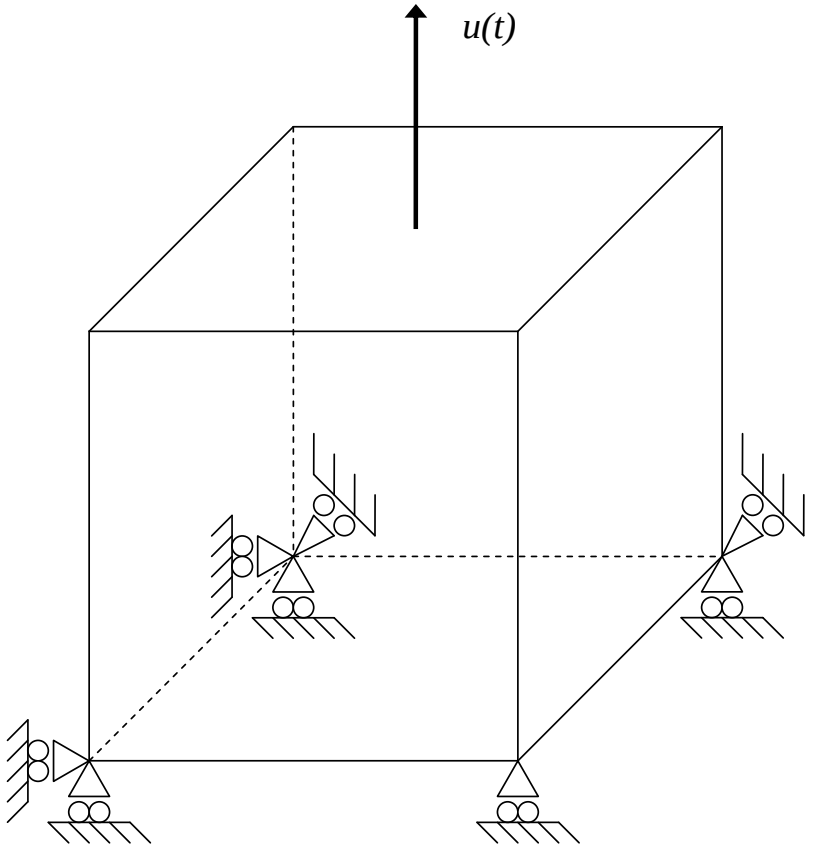

Figure 3.6. Single crystal finite element model in "unconstrained" configuration.

The "constrained" case is the same geometry as the cubic single crystal model, but consisting of 216 cubic C3D8R elements where the specimen is not allowed to

contract or move laterally on the base and the face in tension, shown schematically in two dimensions in Figure 3.7 below.

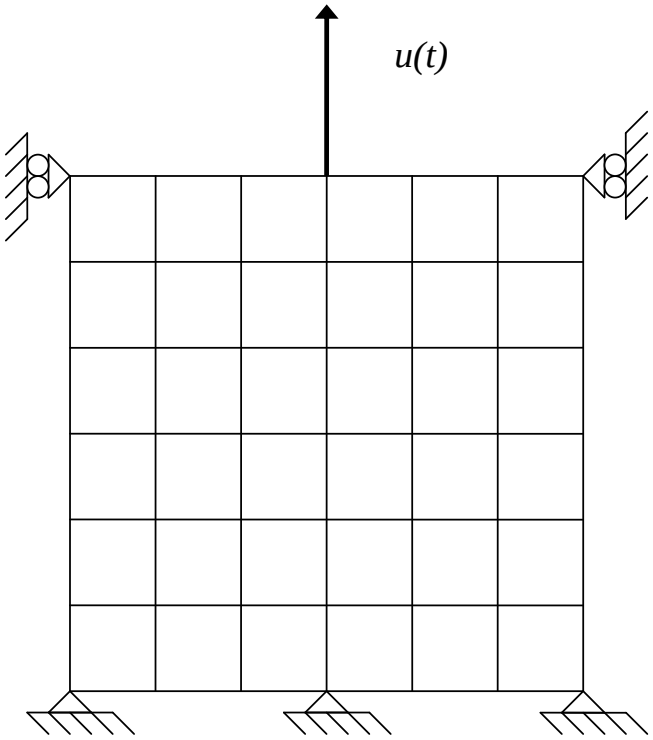

Figure 3.7. Two-dimensional single crystal finite element model in "constrained" configuration. The same illustration can be used for the side view, thus defining the three-dimensional model.

To study of the effect of limited slip system activation and different hardening parameters on the overall macroscopic response of the material, three different material parameter sets will be used, labeled as hard, soft, and hard with recovery. The crystal plasticity parameters that correspond to these material sets is seen in Table 3.1 below,

Table 3.1. Material Parameters for Limited Slip Parametric Study

Parameter	**Units**	**Hard**	**Soft**	**Hard With Recovery**
C_{11}	GPa	150	150	150
C_{12}	GPa	75	75	75
C_{44}	GPa	37.5	37.5	37.5
$\dot{\gamma}_0$	s^{-1}	0.001	0.001	0.001
m	-	30	30	30
D_0	MPa	50	50	50
λ	-	0.9	0.9	0.9
H_{DIR}	MPa	300	1	300
H_{DYN}	MPa	0	0	1.5
Ψ	Rads	0-2π	0-2π	0-2π
θ	Rads	0-π	0-π	0-π
ϕ	Rads	0-2π	0-2π	0-2π

where Ψ, θ, ϕ and are the Euler angles in Roe convention. Note that for the Euler angles in Roe convention to give a completely random orientation, the angles are assigned such that

$$\begin{aligned} \psi &= 2\pi\xi_i \\ \theta &= \cos^{-1}(2\xi_{i+1} - 1) \\ \phi &= \pi\xi_{i+2} \end{aligned} \tag{3.7}$$

where ξ_i is a series of random numbers such that $0 \le \xi_i \le 1$ (McGinty 2001).

Both of the models “hard” and “soft” do not have any dynamic recovery for the drag stress, and will manifest purely isotropic hardening at the slip system level.

Single Crystal Limited Slip Simulations and Results

The first parametric simulation was a full cycle of eight randomly oriented grains with the “hard” parameters and the “unconstrained” boundary conditions where only one slip system was allowed to be active. The results of this simulation are seen in Figure 3.8 below.

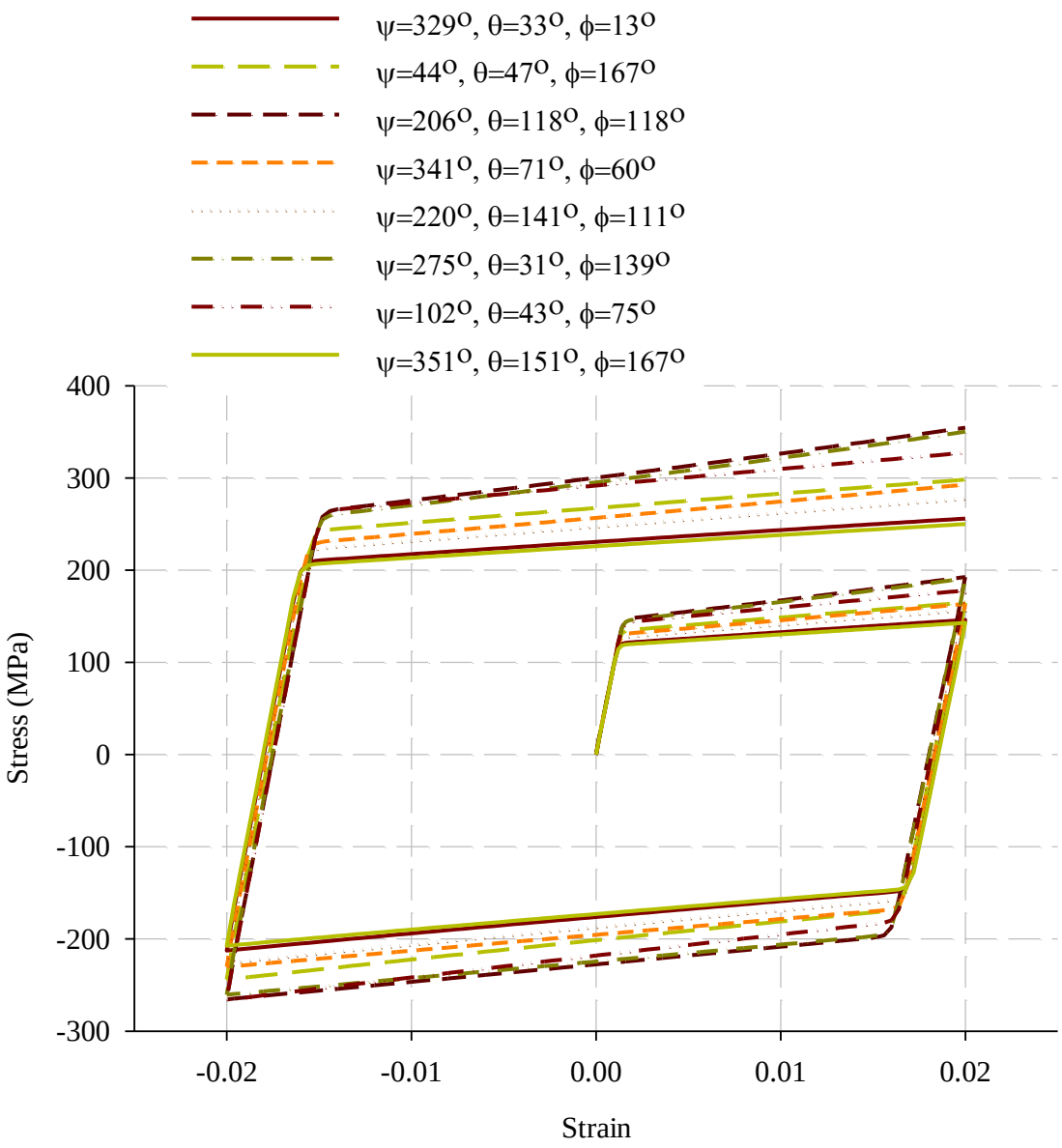

Figure 3.8. Stress-strain response of single crystal with one active slip system, "hard" material properties, and in the "unconstrained" configuration for eight random orientations.

The results from Figure 3.8 are exactly what is predicted from analytical solutions, as a single slip system can accommodate all of the deformation once plastic yielding occurs. The unfavorably oriented configurations have a larger macroscopic stress than the favorably oriented crystals, but the hardening mechanism is the exact same.

To determine whether or not single slip affects the overall hardening response, the number of slip systems was allowed to vary between one and twelve, for one configuration and the macroscopic stress-strain response is shown in Figure 3.9 below.

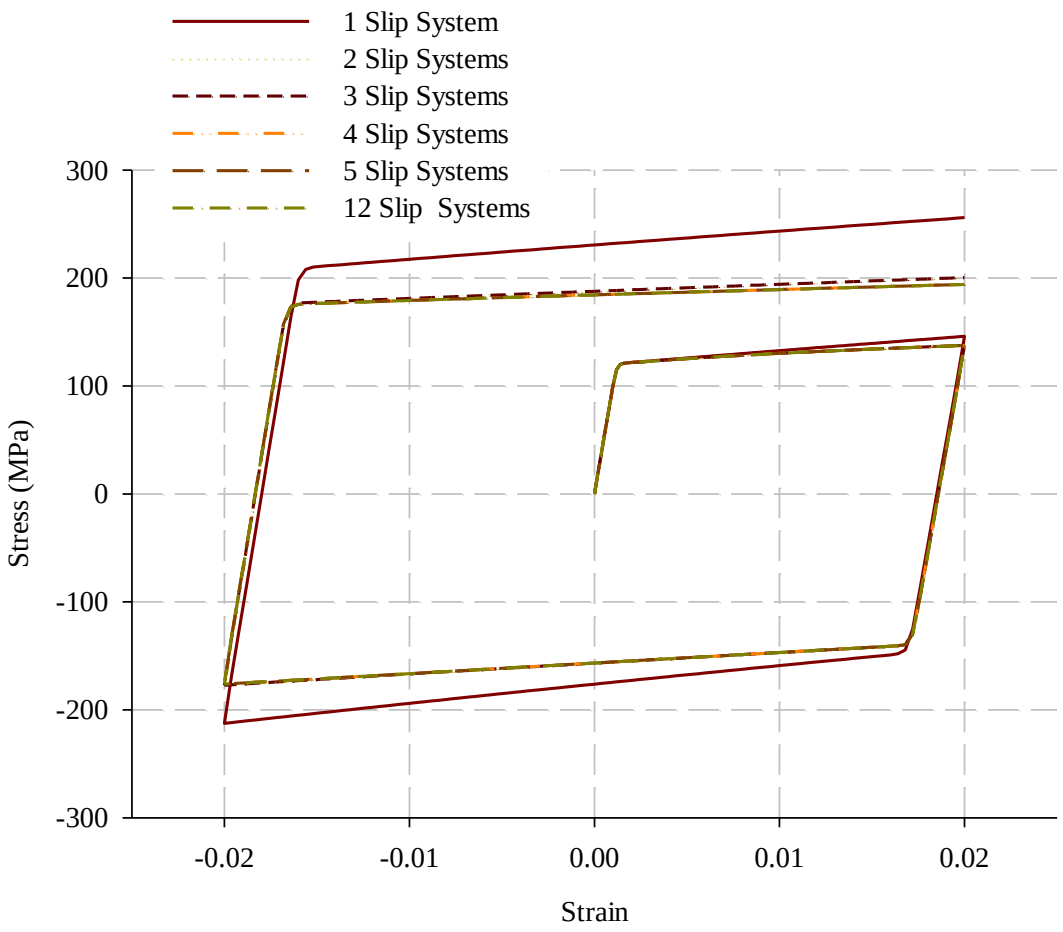

Figure 3.9. Stress-strain response of a single crystal with different numbers of slip systems active and "hard" material properties with "unconstrained" boundary conditions. Euler angles in Roe convention for each simulation are ψ=329°, θ=33°, ϕ=13°.

From the stress-strain response, it is evident that limiting the number of active slip systems decreased the ability for the second slip system to activate. Beyond allowing two active slip systems to activate, there was no consequence for limiting the number of slip systems to accommodate the deformation, as the other slip systems never overcome the critical resolved shear stress to activate slip. It is also noted that plastic deformation was able to accommodate all of the deformation beyond yielding, as the isotropic hardening at

the slip system level manifests itself through isotropic hardening on the macroscale deformation response.

In order to understand the effect of the material properties on the overall macroscopic response for the single slip case, the “hard”, “soft”, and “hard with recovery” material properties were used for the same orientation and loading conditions as in the previous case, and the macroscopic response is shown in Figure 3.10 below.

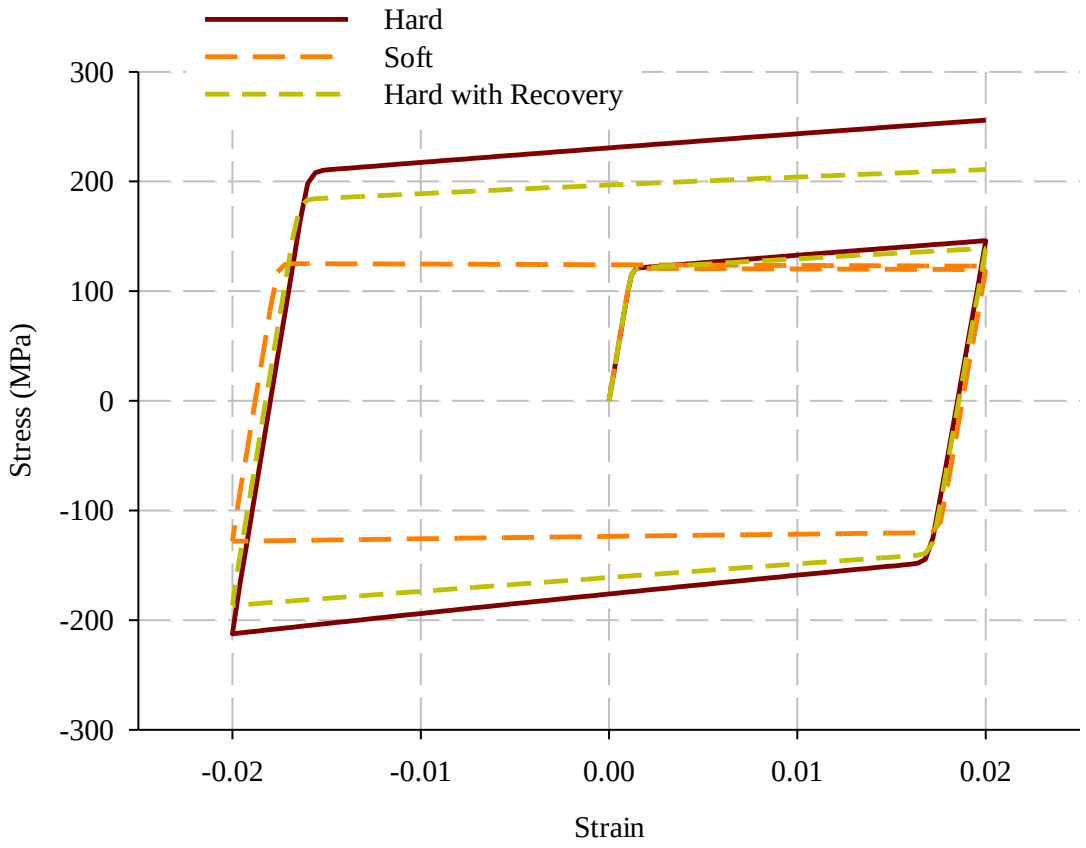

Figure 3.10. Stress-strain response of a single crystal with “hard”, “soft”, and “hard with recovery” material properties with “unconstrained” boundary conditions. Euler angles in Roe convention for all three cases are ψ=329°, θ=33°, ϕ=13°.

The set of “soft” material properties shows insight into the fact that in the “unconstrained” case, a single slip system can accommodate all of the deformation. Also,

the “hard with recovery” material properties behave as expected, where the stress for subsequent hardening decreases as deformation proceeds.

To see whether or not the boundary conditions played a role in the single crystal studies, the “constrained” boundary conditions were applied to the “hard” material parameters with only one slip system active and compared to the macroscopic stress-strain response of the “hard” material parameters for the “unconstrained” boundary conditions with only one slip system active, seen in Figure 3.11 below. For both cases, the same crystal orientation was used.

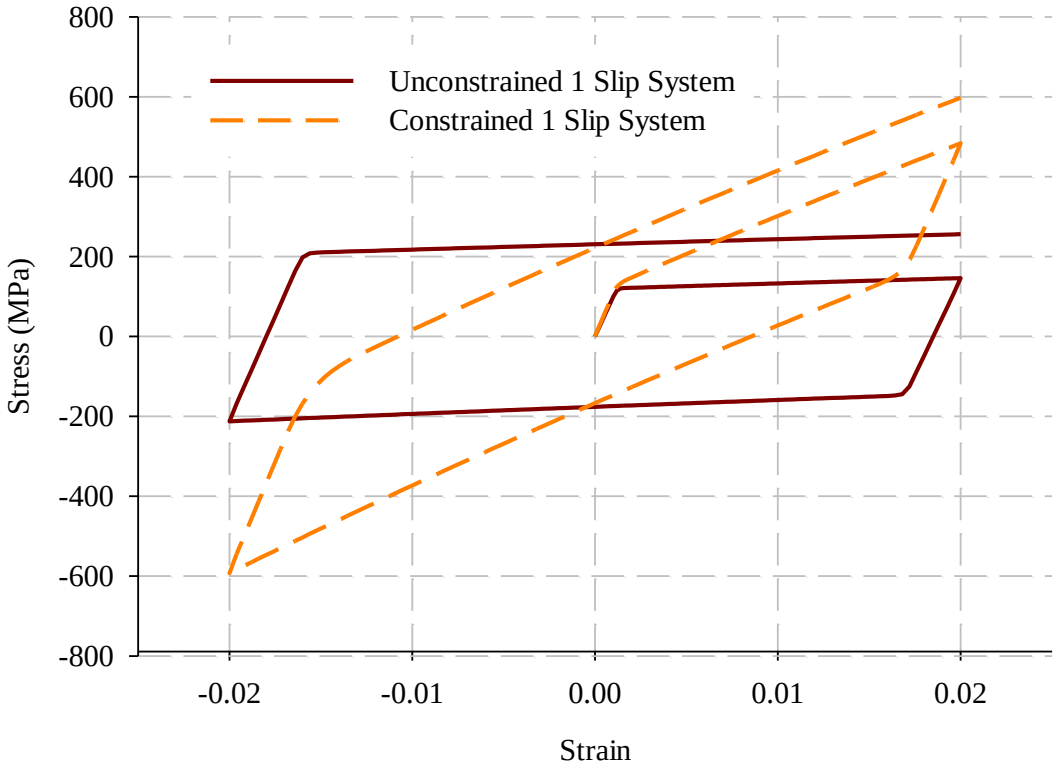

Figure 3.11. Stress-strain response of a single crystal with "constrained" and "unconstrained" boundary conditions, "hard" material properties, and single slip. Euler angles in Roe convention for both cases are ψ=329°, θ=33°, ϕ=13°.

From the overall response, it is clear that boundary conditions play a significant role in the deformation of the single crystal. Despite the same material properties being used, the responses are fundamentally different. Even though hardening is isotropic on the slip system level, the macroscopic response of the constrained 1 slip case is macroscopically a combined isotropic-kinematic hardening. This is combined isotropic-kinematic hardening is due to the inability of a single slip system to satisfy compatibility for the non-uniform deformation imposed by the boundary conditions. The kinematic part of hardening is due to elastic stresses developed to satisfy compatibility, and the isotropic part of the hardening is due to the isotropic hardening at the individual slip system level.

To understand the effect that limiting the number of available slip systems for the "constrained" boundary conditions, the number of available slip systems is varied with the "hard" material parameters, and the macroscopic stress-strain response is included in Figure 3.12 below.

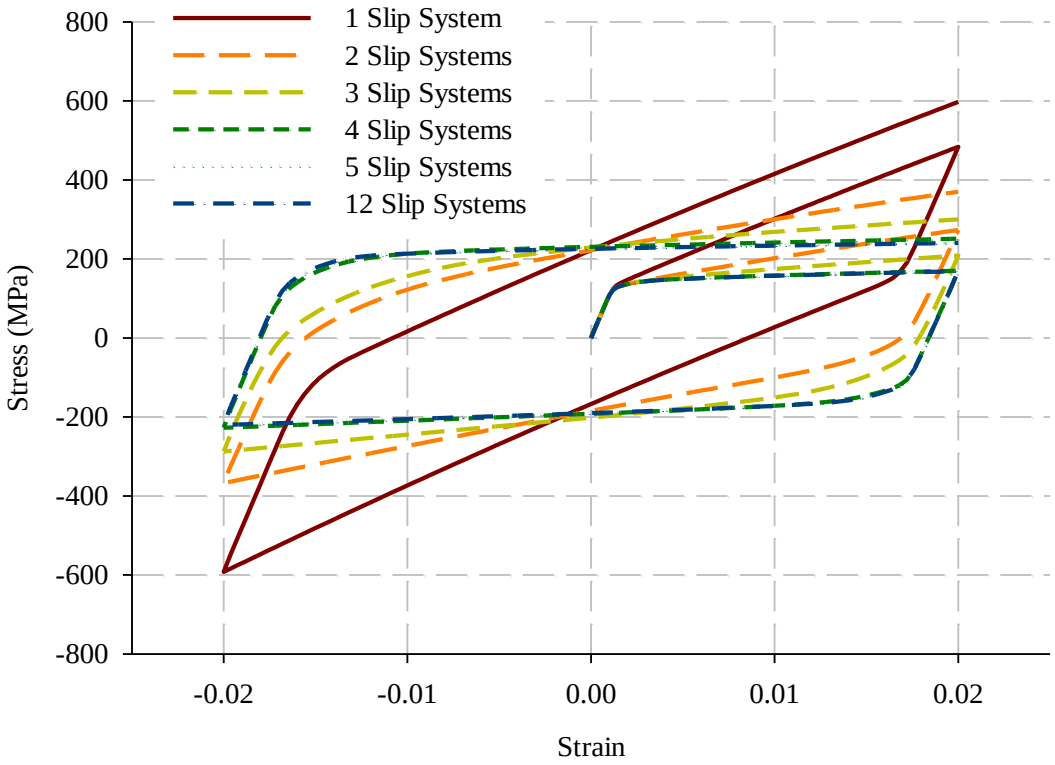

Figure 3.12. Stress-strain response of a single crystal with "constrained" boundary conditions, "hard" material properties, and varied numbers of slip systems allowed to be active. Euler angles in Roe convention for all cases are ψ=329°, θ=33°, ϕ=13°.

From the simulations it is evident that as the number of slip systems is allowed to increase, the amount of overall deformation that is accommodated plastically increases, as evidenced by both the decrease in the macroscopic stress associated with a given strain for increasing slip availability and the increase in the hardening from being combined

isotropic-kinematic to purely isotropic at the macroscale where slip can accommodate all of the plastic deformation.

To further verify that the inability for limited slip availability to accommodate non-uniform deformation, simulations were performed on the same geometry, varied numbers of slip systems, and boundary conditions, but with "soft" material properties. The results of these simulations are seen in Figure 3.13 below.

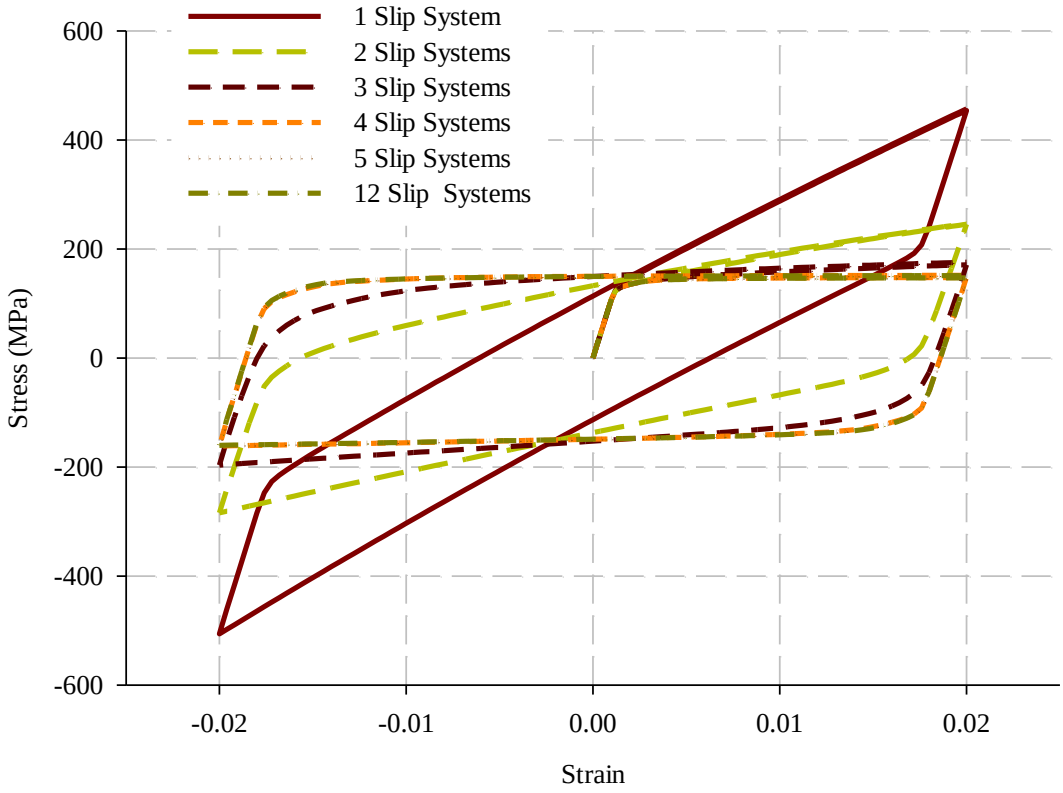

Figure 3.13. Stress-strain response of single crystal with "constrained" boundary conditions, "soft" material properties, and varied numbers of slip systems allowed to be active. Euler angles in Roe convention for all cases are ψ=329°, θ=33°, ϕ=13°.

The simulations with “soft” material properties are conclusive in that even with an elastic-perfectly plastic response at the slip system level, the macroscopic response of the material is akin to kinematic hardening at the macroscale. No expansion of the yield surface occurs due to the inability for hardening at the slip-system level.

Finally, the number of slip systems available was varied with “hard with recovery” material properties and “constrained” boundary conditions, and the result of varying the number of available slip systems on the macroscopic stress-strain response is included in Figure 3.14 below.

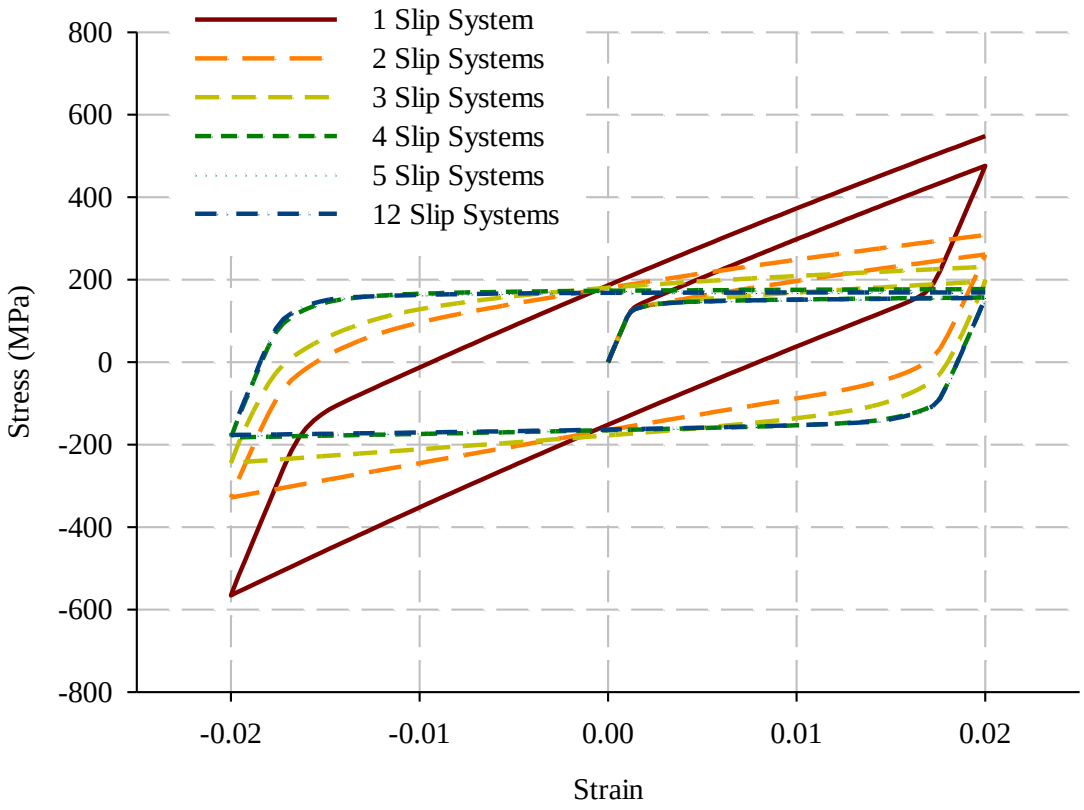

Figure 3.14. Stress-strain response of a single crystal with “constrained” boundary conditions, “hard with recovery” material properties, and varied numbers of slip systems allowed to be active. Euler angles in Roe convention for all cases are ψ=329°, θ=33°, ϕ=13°.

From the above simulations and inferred from the constitutive relations, the ability for decrease its hardening rate coincides with the ability to accumulate plastic deformation. For cases of increased slip systems, a more pronounced effect on the dynamic recovery is observed.

Along the lines of historical developments in understanding plasticity where single crystal experiments were first characterized and then used to predict behavior of polycrystalline ensembles, the same methodology will be applied to the limited slip studies of single crystals.

From the single crystal models for limited slip, it is clear that putting further constraints on the deformation caused more demanding compatibility requirements, and therefore an elastic strain was introduced to ensure compatibility for the "constrained" case. For a single crystal with no boundary condition constraints, i.e. the "unconstrained" case, deformation proceeded in similar fashion regardless of the number of active slip systems.

From the above study, it is predicted that the effect of limiting slip on polycrystal ensembles will be similar in character to the macroscopic stress-strain response of the "constrained" boundary conditions case, and have little resemblance to the "unconstrained" case due to the increased compatibility requirements introduced by deformation of neighboring grains.

Finite Element Model and Model Justification for Polycrystal

The same Abaqus crystal plasticity finite element UMAT used to model single crystal deformation was used to model polycrystal deformation. Because of the large number of grains that comprise most components, a representative volume element

(RVE) of 216 grains was constructed in order to model the response of the bulk material with respect to a fully reversed deformation path. In order to do this, periodic boundary conditions in all three directions were prescribed in which the displaced faces' displacements were defined by a control node. This method is a three-dimension extension of the two-dimension method employed by van der Sluis et al. (2000). The C++ code created by Przybyla and McDowell (2010) used to develop the three-dimensional microstructures utilized the program QHULL when multiple elements were used per grain.

In order to understand the validity of the model, the effect of the number of grains and the number of elements had to first be examined.

The change in the overall macroscopic response was modeled for the tension-compression response of three realizations of 216 randomly oriented grains with "hard" material properties and 12 active slip systems, as seen in Figure 3.15 below.

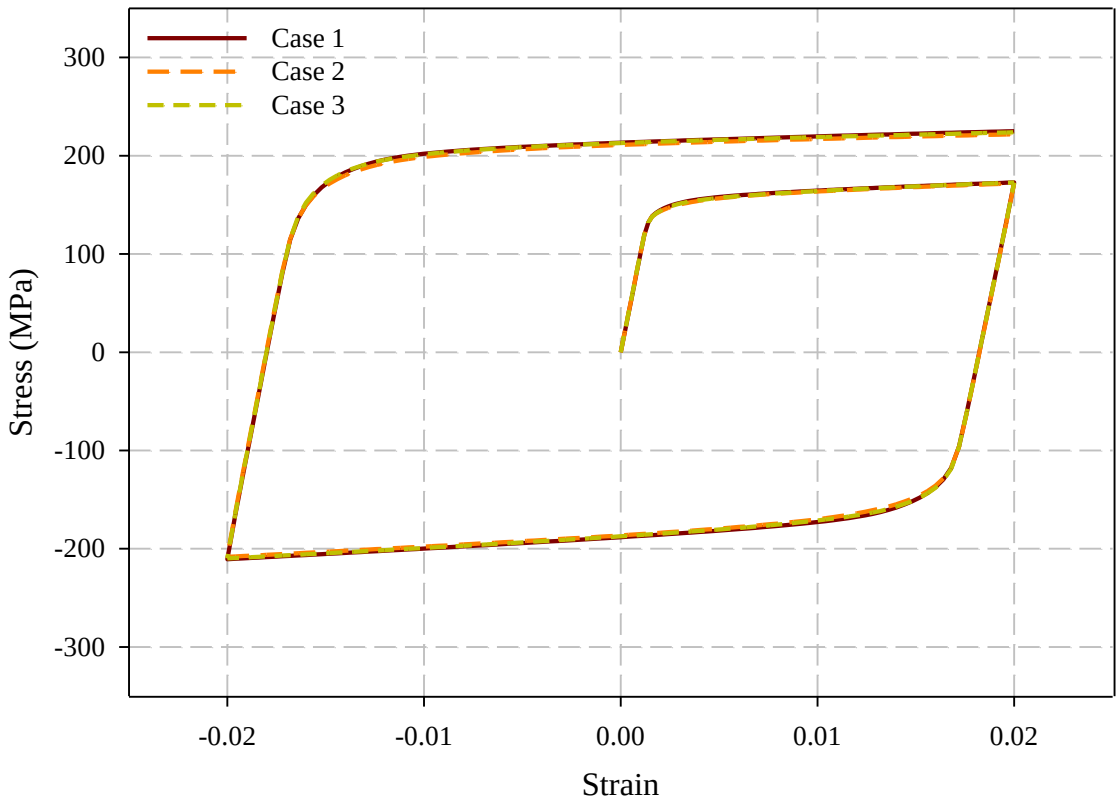

Figure 3.15. Stress-strain response of three different realizations of random grain orientations for cyclic loading of 216grains represented by 216 elements with “hard” material properties and 12 slip systems active.

From the three different cases of cyclic loading with “hard” material properties and random grain orientations, with as many grains are in the model there is little to no effect on the overall macroscopic stress-strain response. Therefore, number of grains used is deemed as sufficient in order to model the heterogeneity due to the individual grains.

The other primary assumption that must be justified is the role of the number of elements used to model each grain. The case in which the most intragranular heterogeneity develops is in the single slip case, so three realizations of 216 grains with

"hard" material properties and different numbers of elements per grain were constructed, and their overall macroscopic stress-strain response is included in Figure 3.16 below.

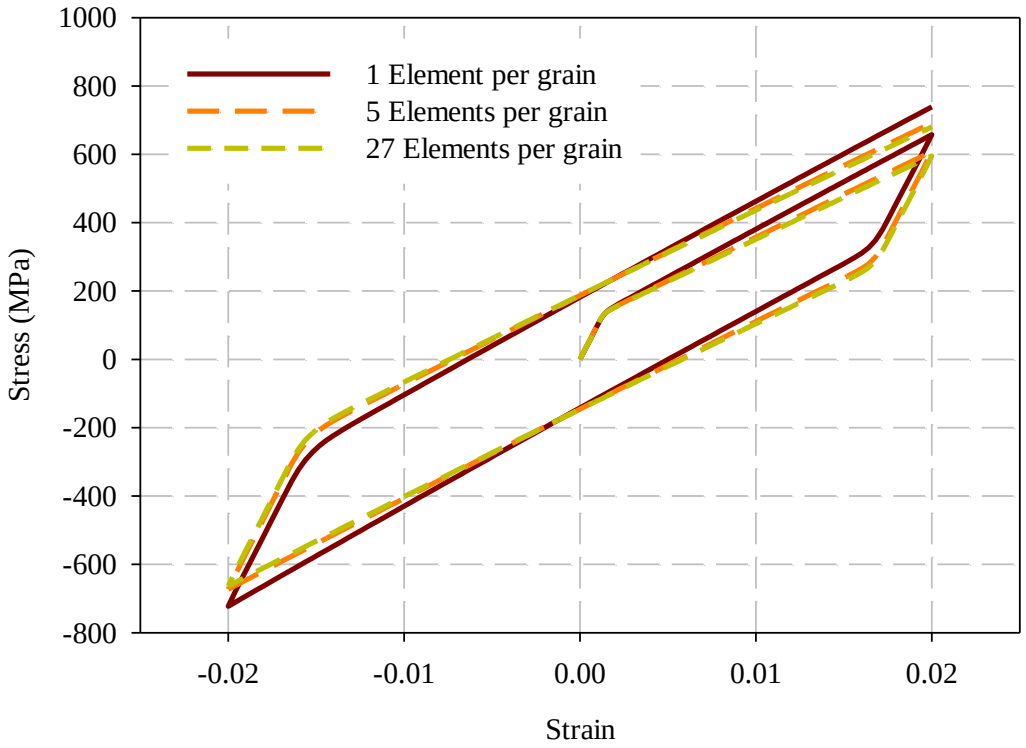

Figure 3.16. Stress-strain response of three realizations, each with varying numbers of elements per grain, of a 216 grain polycrystal with "hard" material properties and random grain orientations.

While there is some deviation from the multiple elements per grain case compared to the single element per grain case, the overall hardening behavior remains similar for all of these cases, and it is therefore acceptable to use a single element per grain to study the effect of limiting the number of slip systems on the hardening behavior. If non-uniform material properties were introduced, this would create more of a dependence on the number of elements per grain used, as the non-uniform compatibility constraint inside of the grain would be greater.

Limited Slip System and Hardening Law Results on Polycrystal

A 216 element cube was created; however, this time each of the elements corresponded to a single grain. Therefore, the 216 element cube is actually a simulation of 216 randomly oriented grains. Each of the grains has the same material properties as the other grains, which are either “hard”, “soft”, or “hard with softening”. The only difference in the grains is that they are randomly oriented, and therefore will see different resolved shear stresses on each slip system.

For the first case of uniaxial tension on the “hard” polycrystal, the same material properties were used except that the angles were randomly oriented for each different slip case. The number of slip systems was varied, and the resulting stress-strain behavior is included in Figure 3.17 below. It should be noted that all grains are assigned the same specified number of active slip systems.

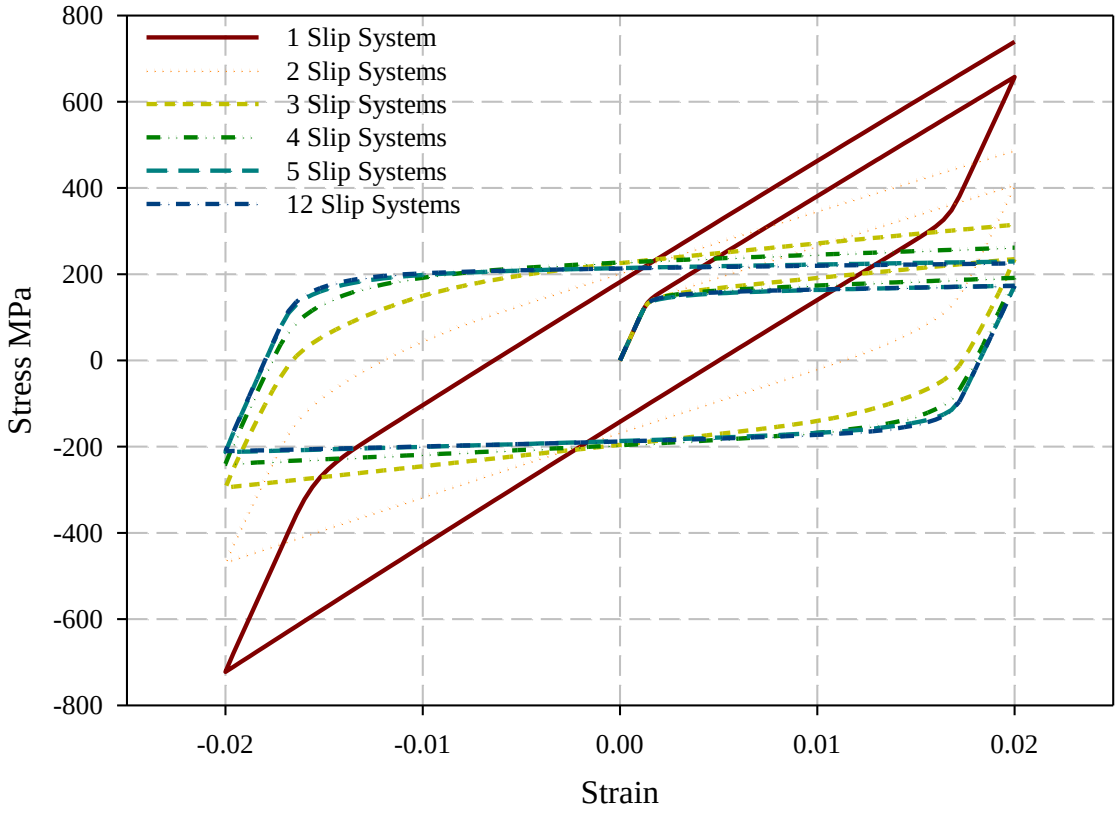

Figure 3.17. Stress-strain response of a 216 grain polycrystal with varying numbers of active slip systems and "hard" material properties.

From the plot above, it is apparent that for the polycrystal with limited slip, it has a similar response to that of the "constrained" single crystal. The same overall behavior still holds in that the transition between the elastic and plastic region is well defined, but the inability for all of the deformation in the limited slip cases to be accommodated by plastic deformation contributes to the apparent macroscopic kinematic hardening.

To better understand how kinematic hardening is manifested through a limited slip formulation, a simple example is considered. It is well known that the Mroz multi-surface model can be constructed in a one-dimensional sense by reversed loading of a multi-bar assembly where each bar has a different yield strength, is elastic perfectly-

plastic, and displacement compatibility is enforced. In crystal plasticity where each slip system behaves elastic perfectly-plastic, the different yield strengths for uniform material properties are manifested through different resolved shear stresses on the different slip systems. However, once five or six slip systems become active, the material can behave perfectly plastically, due to enough independent plastic deformation sources being active. Therefore, until the point where plasticity can account for the enforced displacement compatibility, kinematic hardening is manifested on the macroscale.

The limited slip formulation with no hardening is similar to the elastic perfectly-plastic multi-bar assembly with different yield strengths, except that in this case limiting the number of active slip systems corresponds to requiring that after a certain number of slip systems has yielded, no more are allowed to yield. Therefore, the compatibility requirements mandate an elastic stress be created in the bars that cannot yield in order to satisfy displacement compatibility.

For materials with purely isotropic hardening at the slip system level, limiting the number slip systems that can be active is similar to specifying the number of bars that can yield in the multi-bar assembly. Therefore, the isotropic part of the hardening at the macroscale is manifested through hardening at the slip system level, but kinematic hardening on the macroscale is manifested through the elastic stress required for displacement compatibility in the unyielded bars.

To verify the conclusions made from the previous simulations that the component of kinematic hardening at the macroscale is manifested through limited plastic deformation, and isotropic hardening results from isotropic hardening at the slip system

level for polycrystals, the macroscale response of a polycrystal "soft" material parameter is performed, and included in Figure 3.18 below.

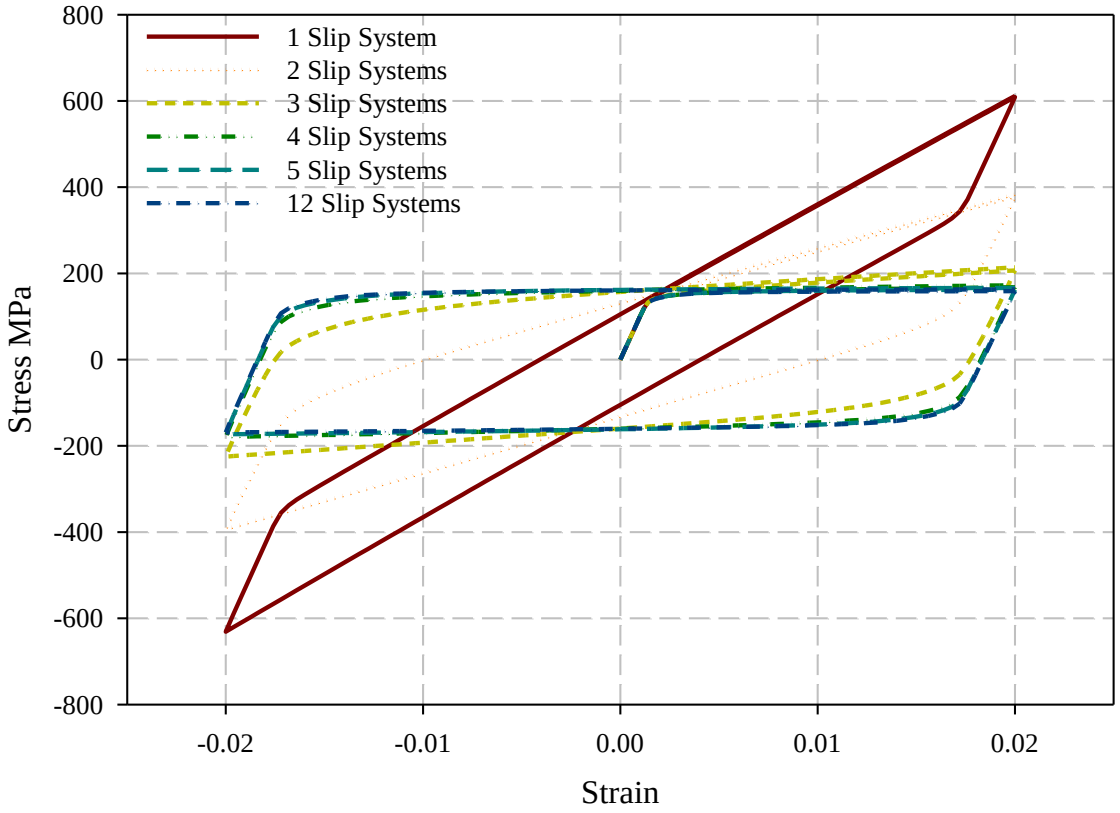

Figure 3.18. Stress-strain response of a 216 grain polycrystal with varying numbers of active slip systems and "soft" material properties.

As happened in the "constrained" single crystal case, the response of the polycrystal with "soft" material properties with no hardening reveals that limited slip combined with displacement compatibility is responsible for the observed macroscale kinematic hardening behavior.

Finally, for the case in which slip can saturate on different systems with the "hard with recovery" material parameters, the uniaxial cyclic loading was run with the same microstructures as was previously mentioned, and the overall macroscopic stress-strain response is found in Figure 3.19 below.

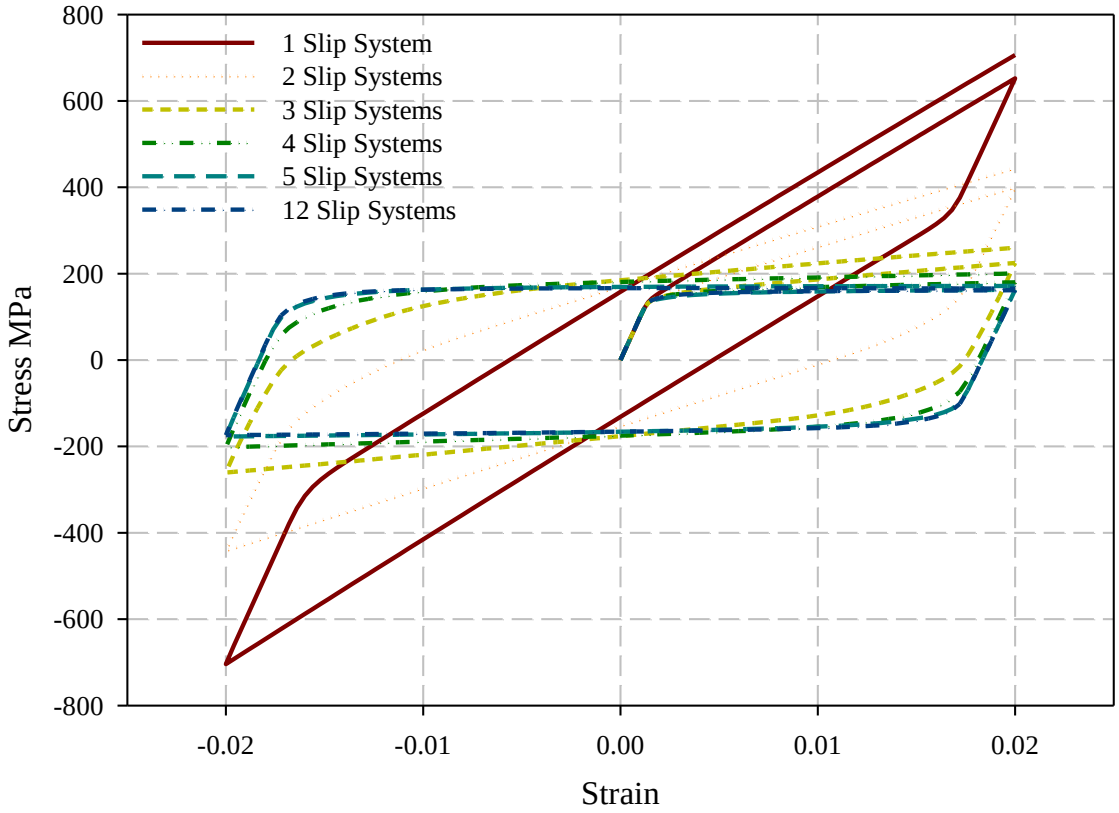

Figure 3.19. Stress-strain response of a 216 grain polycrystal with varying numbers of active slip systems and "hard with recovery" material properties.

Figure 3.19 shows that there is not a significant effect of the dynamic recovery with respect to the limited slip cases, but does have an effect on the 5 and 12 available slip system cases, as seen by the stabilized hardening response for both the 5 and 12 slip system cases. This is due to the fact that more total plastic deformation can accumulate for the cases of multiple active slip systems, as was also the case in the "constrained' single crystal simulations.

Discussion of Limited Slip Model Results

A theme from both the "constrained" single crystal and polycrystal limited slip simulations is that the macroscopic kinematic hardening is quite sensitive to compatibility if plastic compatibility is not satisfied everywhere in the material.

Where the limited slip model diverges from experimental observations is the ability for the material to soften with increased loading. Micrographs of material microstructures during progressive amounts of deformation as was shown in the experimental evidence of limited slip section show that the microstructure continues to refine as deformation progresses. From the micrographs of Mughrabi (1971), it is apparent that initially the material has small amounts of localized slip and as deformation progresses then the slip on some systems can cross-slip or develop onto other systems, creating a network of dislocations. As deformation proceeds, these dislocation substructure networks align to accommodate the most highly strained orientations.

Because the material properties in this formulation are defined in a uniform manner a priori and do not update with respect to the localized structures that are formed during deformation, a limited slip model cannot connect with realistic material response. Furthermore, experimental observations from Zaiser et al. (1999) show that there is a characteristic fractal dimension which defines the self-similarity of dislocation substructures over two orders of magnitude, from 10nm – 700nm. Consequently, a formulation that allows for limited slip to define the areas in which slip can occur in "patchy" fashion would have to be refined down to this scale.

The degree of kinematic hardening, self similarity, and cellular structure formation would have to be a function of strain, strain rate, initial structure, temperature, and other material parameters. The parametric study of limited slip formulations is merely a tool to understand the consequences of limiting slip on the aggregate grain-scale stress-strain response of materials.

Conclusions of Limited Slip Simulations

Insight into the effect of the constraints imposed on single crystals has been gained due to the fact the fact that if the crystal is unconstrained and free to deform, then one slip system will be primarily responsible for deformation, whereas for a more constrained boundary condition imposed on the same single crystal, multiple slip systems must be active to accommodate the deformation. If these systems are unable to activate, then imposed displacements will be satisfied with an elastic stress. This idea of insufficient deformation sources in a crystal plasticity formulation was first presented in (Parks and Ahzi 1990).

After looking at the single crystal case, the polycrystal case is evaluated and a methodical presentation of limiting the number of active slip systems for polycrystals is given. Because the number of active slip systems is intrinsically tied to the ability for the material to accommodate arbitrary deformation, violating the Von Mises criterion causes an increase in the elastic stress in order to satisfy compatibility. While the macroscopic stress-strain responses of the simulations should not be compared to actual experimental responses, insight is gained into the role of the inability for arbitrary plastic deformation to satisfy compatibility at everywhere in the material, as is experimentally observed through formation of dislocation substructure.

The idea of considering the role of boundary conditions with respect to the number of required slip systems has already been observed by Haldrup et al. (2009), where the number of required slip systems is simulated for periodic and free boundary conditions for polycrystals. Also, the work of Clausen et al. (1998) quantified the number

of required slip systems as a function of strain in polycrystals for a self-consistent numerical scheme.

Another aspect introduced by the limited slip constraint not yet discussed is that compatibility requirements in the presence of limited slip demand that the elastic part of the deformation gradient increases, thus driving grain and subgrain rotation. In order to illustrate this point, monotonic deformation of similar polycrystalline metals was simulated and is shown in Figure 3.20 below.

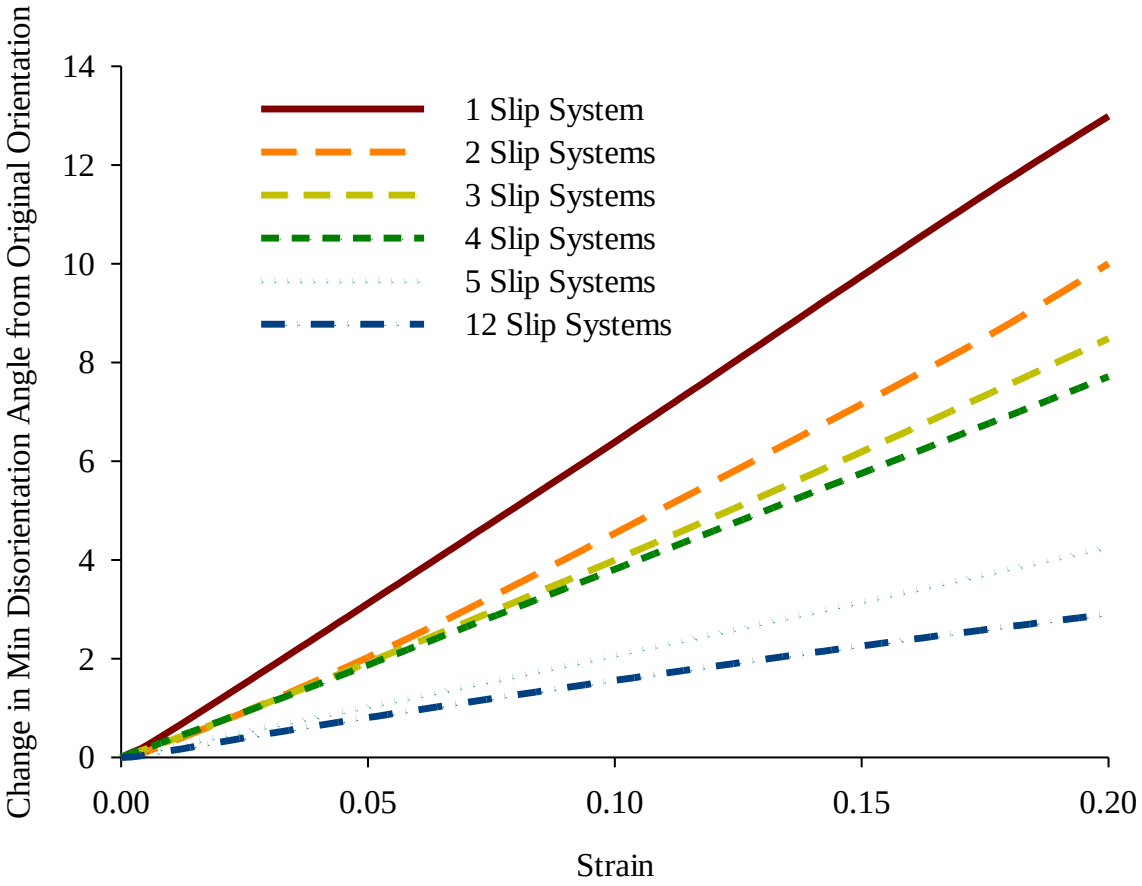

Figure 3.20. The average change of the minimum disorientation angle between the final orientation and initial orientation for a 216 grain polycrystal with varying numbers of potentially active slip systems and “hard” material parameters.

Rotations induced by limiting the number of active slip systems can be used to understand the effect of the compatibility constraints imposed on individual grains in polycrystals.

First, to understand how the calculated average rotation angles compare to experimental rotation angles seen inside of grains, the theoretical average minimum disorientation angle with respect to number of active slip systems is compared to EBSD experiments of FCC polycrystals inside individual grains that measured the change in disorientation angle from the deformed orientation to the original orientations at 10% tensile strain, and are included in Figure 3.21 below.

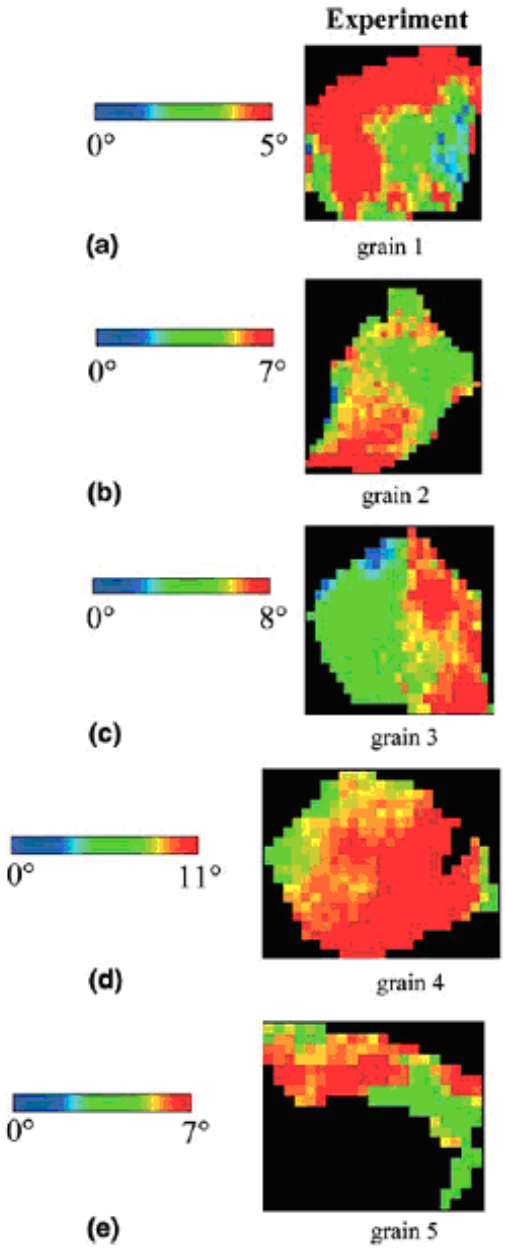

Figure 3.21. Experimentally measured misorientation angle between final orientation and initial orientation in OFHC Cu at 10% tensile strain using EBSD measurements from Buchheit et al. (2005).

While a one-to-one mapping of disorientation angle to strain cannot be made due to the non-uniform strain inside of the grain, qualitatively, the ability for limited slip deformation to drive sub-grain rotation is evident. The most prominent scaling

relationship between plastic deformation and misorientation angle was set forth by Hughes et al. (1997)

$$M_E = \alpha E_p^{2/3}, \tag{3.8}$$

where M_E is the minimum misorientation angle, E_p is the plastic strain, and α is a fitting parameter. Like the average misorientation angle dependence of limited slip with respect to remote strain, the fitting parameter in this scaling relationship is intrinsically tied to compatibility constraints imposed on the material. For example, in torsion tests α is larger due to the increased compatibility requirements.

Experimental results presented by McDowell (2010) verify the α dependence by presenting the experimental relationship between the misorientation angle formed between subgrain boundaries for compression and torsion and the plastic strain, as seen in Figure 3.22 below.

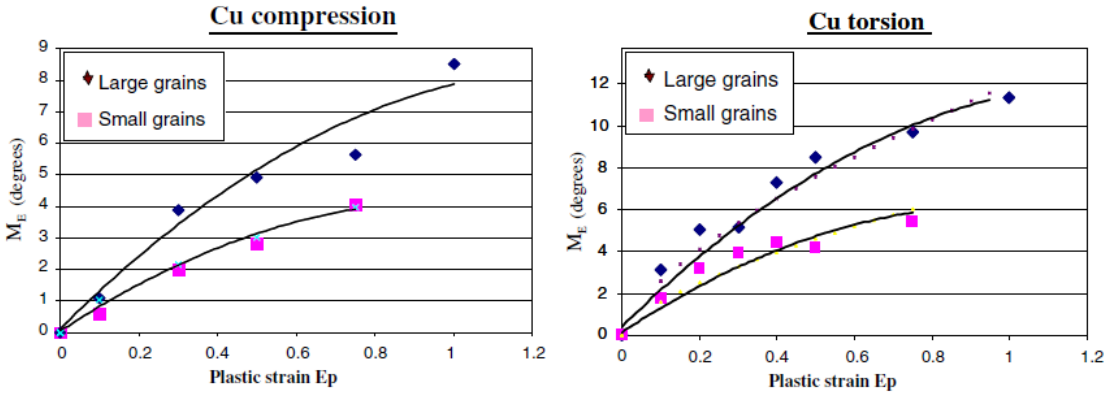

Figure 3.22. Minimum misorientation angle between subgrain boundaries for large and small surface grains in OFHC compression and torsion tests from McDowell (2010).

Larger grains have a higher average misorientation angle for subgrain boundaries due to the increased compatibility requirement to satisfy displacement compatibility throughout the grain. While the misorientation angle measured in Figure 3.22 is different

from Figure 3.21 in that the former measures the relative orientation change of subgrain boundaries, instead of the latter that measures the change in misorientation angle from final and initial configurations, the underlying theme between these experiments that increased compatibility constraints and decreased ability to satisfy compatibility constraints combine to drive subgrain rotation.

CHAPTER 4: COMBINED TOP-DOWN, BOTTOM-UP, LENGTH-SCALE DEPENDENT CRYSTAL PLASTICITY MODEL

The ability for crystal plasticity to model the onset of deformation and the subsequent localized hardening response in problems where localized plastic deformation is of primary importance such as high cycle fatigue, notch root yielding, or crack initiation in monotonic or cyclic loading depends on the amount of initial information given for the problem. Due to the large number of parameters in crystal plasticity models, two methods can be used in order to extrapolate the model's behavior onto other problems. The first method, which is the most effective when it is available, is to use the minimum number of material parameters needed to match the macroscopic stress-strain response of complex loading histories which should include multi-axial, multi-path, and multiple strain rate loading histories. The second method is to justify the evolving material parameters based on analytical and experimental models, and to match the behavior for a given set of data, such as monotonic or fully reversed loading.

A clear example of this is presented in Figure 4.1 below where two periodic polycrystalline 216 grain models have seemingly the same macroscopic stress-strain behavior in monotonic tensile loading. Both models have a grain-size dependence on their material properties, but the first model assumes that increasing the grain size leads to decreasing yield strength, an increased hardening rate, and has no effect on the number of active slip systems, whereas the second model assumes increasing the grain size leads to decreasing yield strength, decreasing hardening rate, and a decreased number of active slip systems.

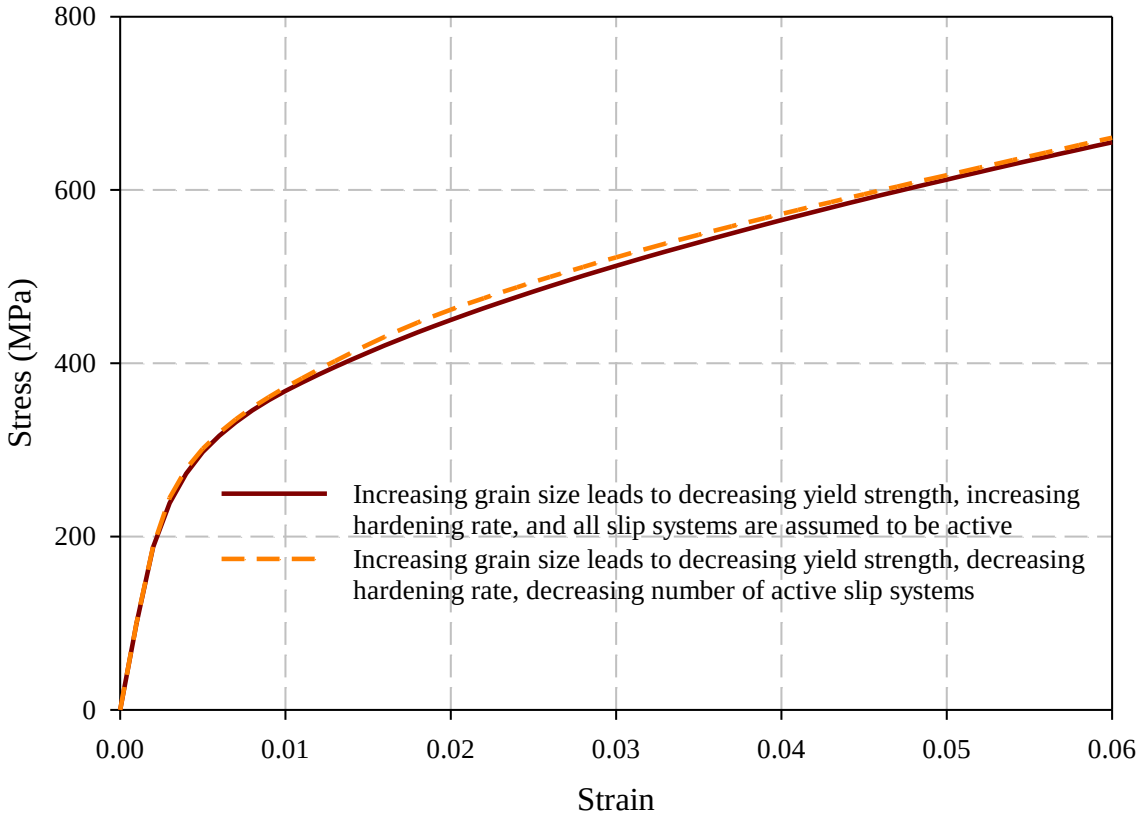

Figure 4.1. Macroscopic stress-strain behavior for monotonic tensile loading of a polycrystalline material with 216 grains but different hardening dependence on grain size.

Because of the large number of material parameters, these models can be made to yield the same monotonic tension loading paths; however, when the same two models are cyclically loaded instead of monotonically loaded, the two different grain size dependencies responsible for hardening become immediately apparent, and their macroscopic response to a fully reversed cycle is seen in Figure 4.2 below.

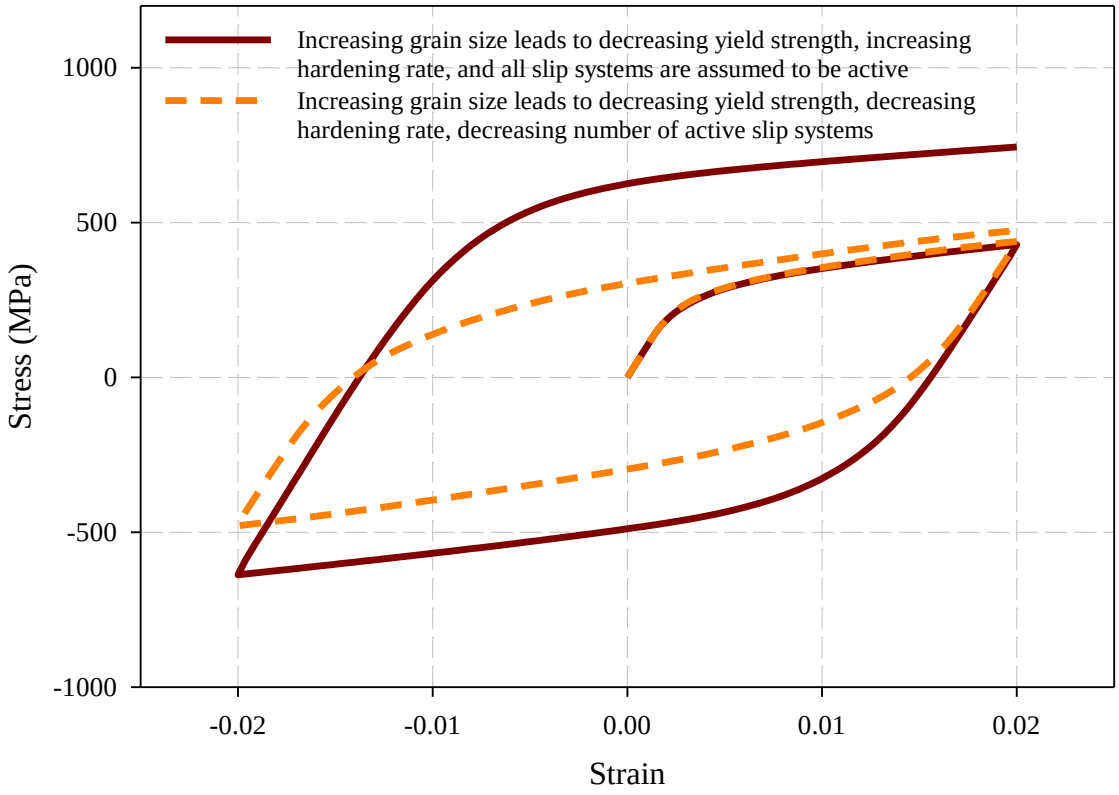

Figure 4.2. Macroscopic stress-strain behavior for fully reversed loading of a polycrystalline material with 216 grains but different hardening dependence on grain size.

Even though both of these models had similar monotonic loading responses, their response to a fully reversed load is strikingly different. Clearly, if either of these models were used for cases of multi-axial or fully reversed responses, they would yield highly different results, thus justifying the need for either an extensive matching to experimental data, or a physical underpinning of each crystal plasticity parameter based on analytical or experimental insight of mesoscale deformation processes. Also, each of these parameters should depend on grain-scale attributes such as slip line length, proximity to grain boundary, or other physical measures inside of the grain in order to more accurately

model deformation at the mesoscale while still maintaining the simplicity of numerical implementation of a local model.

Experimental and Computational Results of Yield Strength Dependence on Grain Size at the Mesoscale

The most historically significant yield strength formulation is the Hall-Petch relationship. The classical inverse square dependence of yield strength of grain size, however, is formulated with respect to coarse grains. For a complete perspective, the Hall-Petch relationship needs to be viewed at multiple scales.

At the nanometer scale, Chokshi et al. (1989) were the first to note the breakdown of the Hall-Petch relationship in OFHC Copper and Pd polycrystals. In their work, they examined hardness dependence on grain size and observed both the classical Hall-Petch relationship for coarse grained copper down to around 1μm with good agreement to experiments, but saw an inverse Hall-Petch relation around the 20nm scale, as seen in Figure 4.3 below.

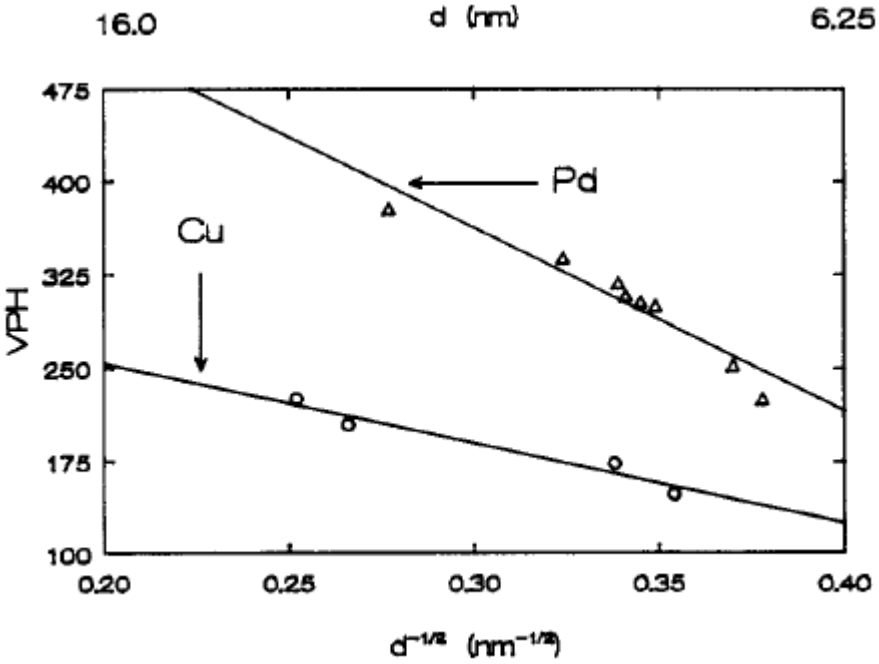

Figure 4.3. Inverse Hall-Petch relationship as a function of hardness for polycrystalline Cu and Pd reproduced from Chokshi et al. (1989).

This experimental evidence shows that clearly the Hall-Petch relationship breaks down in the nano-crystalline regime. While this does not bear much of an effect on yield strength dependence of grain size at the mesoscale, it serves as motivation for investigating yield strength dependence at the 100nm-10μm range. Molecular dynamics (MD) simulations by Schiøtz (2004) showed that in the inverse Hall-Petch regime of 15-50nm that dislocation mediated plasticity is hindered by a lack of Frank-Read sources and pile-ups, and is instead the yield strength is controlled by grain boundary sources, grain boundary sliding, and other non-Schmid plasticity sources.

Compression experiments on Focus Ion Beamed (FIB) single crystals were tested in compression by Uchic et al. (2004) and revealed a large sample diameter dependence on yield strength in the 500 nm to 20 μm range. While there is a range of scatter with yield strengths at this point, there was a larger than inverse square dependence of bulk

yield strength on sample size. While these experiments remain somewhat controversial due to the lack of knowledge of the residual stresses and stress concentrations that the FIB imposes on the samples, it is clear that in the 500nm-5μm regime that yield strength dependence is not modeled correctly by a classical Hall-Petch relationship.

The initial yield strength dependence in the larger grain regime of 10-175μm of polycrystalline OFHC Cu was characterized by Gourdin and Lassila (1991), who observed close agreement with the classical Hall-Petch relationship.

In summary, the classical Hall-Petch relationship is experimentally verified for grains larger than 10μm; however, for grain sizes below this, the inverse square root relationship does not correctly model the yield strength dependence on grain size. In order to understand the reasons behind the breakdown of the Hall-Petch at smaller scales, multiple concepts will be explored that characterize the yield strength dependence in the mesoscale regime. For a review of length-scale dependence on yielding and other mechanical properties, the reader is referred to Arzt (1998).

Models for Yield Strength Dependence on Grain Size

For a large range of strain rates, homologous temperatures, and grain sizes, dislocation glide is the primary mechanism responsible for plastic deformation of metals (Ashby 1972). The models that will be presented below for yield strength dependence on grain size as per the Hall-Petch relation that will follow rely on the fact that yielding is a function of dislocation nucleation, multiplication, and annihilation. This assumption; however, has limitations at very small length scales.

According to Ashby's deformation mechanism map for average grain sizes on the order of 10μm-100μm and homologous temperatures $T_H < 0.4$, plasticity is attributed to

dislocation glide. Also, because there is no change in the dislocation glide part of the deformation map for larger grains and the Hall-Petch relation holds for larger grains, dislocation glide is assumed to be the primary mediator of plasticity for larger grains. Due to the small grain sizes in nanostructured materials, plastic deformation transitions from dislocation nucleation to grain boundary sliding and twinning in the area of grain sizes around 20nm or less (Schiøtz 2004). Therefore models that predict yield strength dependence on dislocation motion should be limited to grains larger than 50nm.

Another aspect to examine is yield strength dependence on strain rate. Initial yield strengths were analyzed for a range of strain rates from OFHC Cu, 4340 Steel, and Iron, and no significant initial yield strength dependence was seen for strain rates on the range of $10^{-3} - 10^{4} s^{-1}$ (Johnson and Cook 1985). Therefore, over seven orders of magnitude of strain rates, dislocation glide is seen as the dominant mechanism for plastic deformation, which therefore governs the onset of yielding.

Now that the limitations of models that use dislocation nucleation as the primary form of plastic deformation have been explored with respect to grain size, homologous temperature, and strain rate, different models will be presented below.

Ohno and Okumura Model

An analytical approach which uses the self energy of Geometrically Necessary Dislocations (GNDs) was incorporated into the higher order stress in a slip gradient formulation to calculate the necessary average resolved shear stress in order to activate slip in model 3D spherical grain in single slip (Ohno and Okumura 2007). From calculations on circular, spherical, and Tetrakaidecahedral grains, a generalized form for the initial yield strength is

$$\frac{\sigma_Y}{\mu b} = \frac{M\theta a}{D}, \tag{4.1}$$

where M is the Taylor Factor, θ is a geometrical factor, and a is a coefficient corresponding to the self energy of a dislocation in an infinite medium, μ is the shear modulus, and D is the grain diameter. Further simplifying with a first order approximation of the Taylor Factor $M = 3$, $\theta = 5$ for different geometries that were done in the study, and an approximation of $a \approx 0.10 \times \ln\left(6.5 \times 10^3 D\right)$ in μm, the relation

$$\sigma_Y = f\left(E, \mu, \frac{1}{D}, b\right) \tag{4.2}$$

with an inverse relation between the initial yield strength and the grain diameter D. When the relation is plotted for multiple materials in Figure 4.4 below, it is seen that there is good relation in the grain diameter range of 1μm-10μm, but begins to break down at greater than 10μm down to the conventional $\frac{1}{\sqrt{D}}$ yield strength dependence as seen in the Hall-Petch relation.

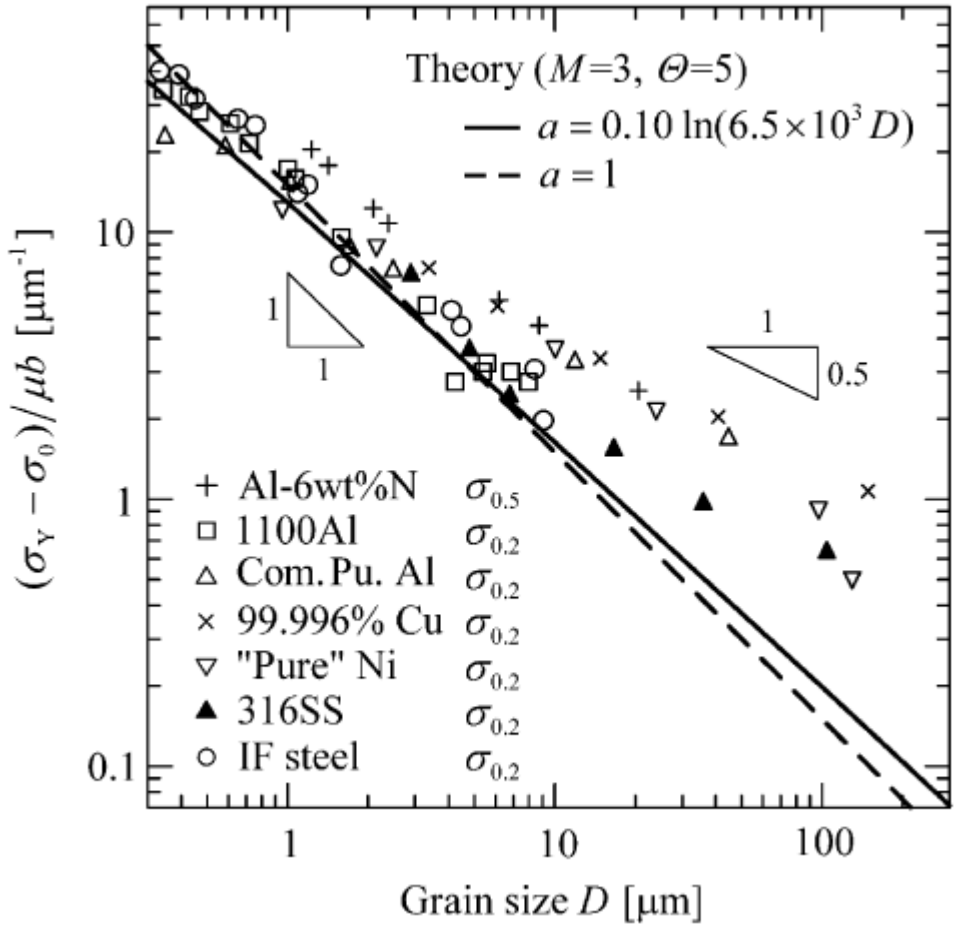

Figure 4.4. Initial yield strength dependence plotted for different materials and alloys for different grain sizes with two approximations for dislocation self energy coefficient *a* (Ohno and Okumura 2007).

Ohashi, Kawamukai, Zbib Model

Considering a Frank Read source embedded in an infinite crystal with no lattice friction, the resolved shear stress required to activate a closed dislocation on that loop is

$$\tau_{CRSS} = \frac{\mu b}{\lambda} \tag{4.3}$$

where μ is the elastic shear modulus, b is the magnitude of the burgers vector, and λ is the dislocation source length. In a real material, not only is the grain of finite size, but there is also a finite lattice friction due to existing dislocations in the material. The effect of the grain boundary is highlighted in Discrete Dislocation Dynamics (DDD) simulations in which a constant source size was varied over different grain sizes and the critical resolved shear stress required to emit a full dislocation loop was calculated (Ohashi et al. 2007).

While this model does not consider source-source interactions inside of the grain, it asserts that this interaction was considered for a sample case and had a negligible effect on τ_{CRSS}. The results of their DDD simulations show a significant dependence of τ_{CRSS} on grain diameter D, as shown in Figure 4.5.

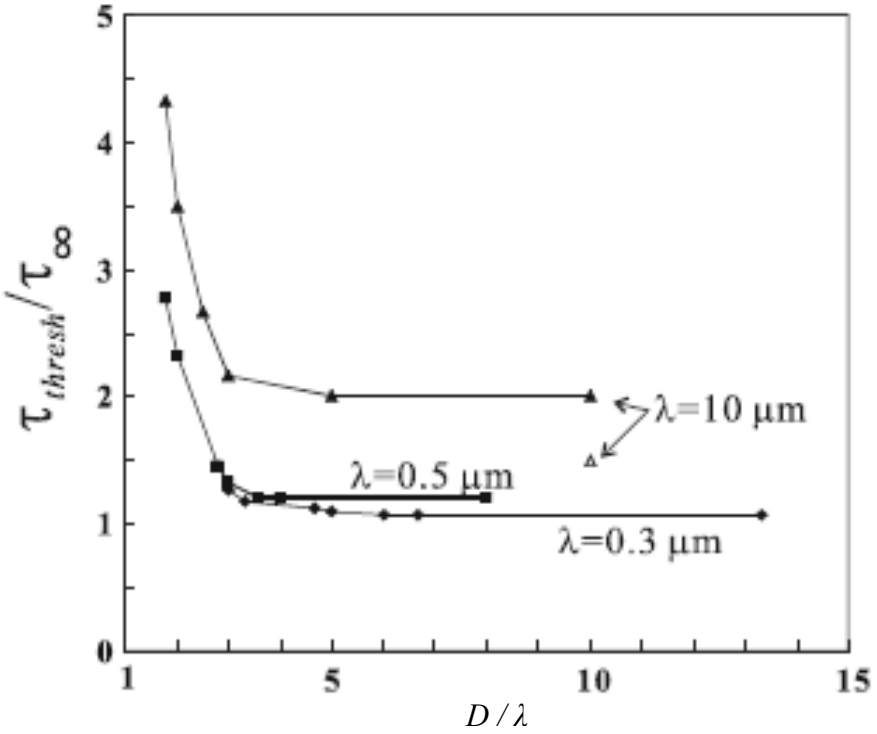

Figure 4.5. Threshold stress plotted with respect to source length, λ and grain diameter, D

It is noted from Figure 4.5 that there is a critical ratio of $\frac{D}{\lambda} \approx 3$ that the threshold stress increases without bound for, which implies that if a uniform distribution of dislocation sources of equal length λ are contained in the material, then this will yield $\tau_{CRSS} = \frac{3\mu b}{D}$ for the onset of yielding in the grain. It should be noted that the probability of a large source being a large grain due to the increased grain volume, which would therefore yield an even greater dependence of τ_{CRSS} on D according to the assumptions of this model.

Conclusions from Analytical Models

Both of these models present somewhat complicated methodologies to calculate the yield strength dependence on grain size. A further look into the studies of Ohno and Okumura (2007) reveal that the simplification of assuming a geometrical factor of 5 is acceptable for the overall yield strength response, but in reality the calculation depends on the projection of the slip plane onto the pierced area and pierced perimeter of the grain. Therefore, a more accurate dimension that should be considered is the projection length of the slip line, and not the overall average grain diameter.

Experimental and Computational Results of Strain Hardening at the Mesoscale

From earlier discussions on yield strength dependence of grain size, dislocations are not the fundamental source of irreversible deformation in the very high strain rate, very high/low homologous temperature, or nanoscale (50nm or less) grain regimes. Most applications do not fall into this regime. Furthermore, experimental and computational studies are needed in order to understand strain hardening dependence on grain size in order to understand mesoscale hardening behavior.

In the submicron regime (greater than 50nm) to micron regime three-dimensional Discrete Dislocation Dynamics (DDD) simulations were performed on strain-controlled, cube-shaped, Al specimens in order to reveal dislocation avalanches which are the fundamental mechanism for the accumulation of dislocations, and therefore govern dislocation mediated plasticity at any scale where dislocations are the primary source of irreversible deformation (Csikor et al. 2007). Fundamentally, these dislocation avalanches occur in single steps in single slip, even in the case of multiple slip systems being seen as simultaneously active. The things that stop a dislocation avalanche from

continuing are the increased stress due to the introduction of additional dislocations, the source-obstacle interactions, and, in displacement control, the overall decrease in stress level with respect to an applied strain. When a dislocation avalanche extends across the entire characteristic dimension in polycrystals, which is the grain, it corresponds to the projected slip line length of the avalanche. In the continuum sense, dislocation avalanches are not discrete events, but rather a sum of statistical processes that are idealized to act in a continuous manner. Therefore, the fundamental length scale at the mesoscale according to the dislocation avalanche should be the projected slip line length to the next barrier.

Assuming that mean dislocation spacing governs work hardening, the Taylor relation is given by

$$\tau = \alpha \mu b \sqrt{\rho}, \tag{4.4}$$

where μ is the shear modulus, b is the magnitude of the burgers vector, α is an evolving parameter that is a function of the structure of the material, and ρ is the dislocation density. The dislocation density is sometimes divided as

$$\rho = \rho_S + \rho_G, \tag{4.5}$$

where ρ_S is the statistically stored dislocation distribution (SSD), and ρ_G is the geometrically necessary dislocation distribution (GND) (Ashby 1970). Statistically stored dislocations do not change the lattice curvature, as they have no net burgers vector, while geometrically necessary dislocations have a net burgers vector. Therefore, for uniform deformation, the statistically stored dislocation density is relatively higher, but for non-non-uniform deformation with large strain gradients, a higher geometrically necessary dislocation density is predicted.

Experiments on OFHC Cu show that the Taylor relation holds true for a variety of ranges of flow stress regardless of internal structure, as seen in Figure 4.6 below

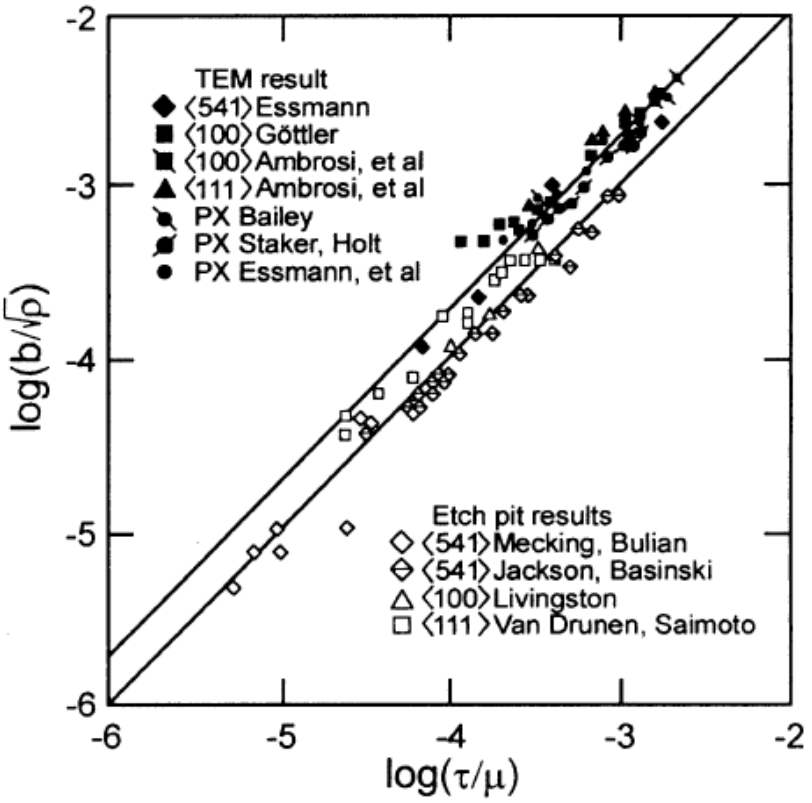

Figure 4.6. Flow stress dependence on dislocation density for a variety of tests on Copper single and polycrystals at room temperature from Mecking and Kocks (1981).

due to the fact that both SSDs and GNDs have a self-energy associated with their increased densities, and therefore add to the CRSS required for subsequent yielding.

Over several orders of magnitude it is apparent that the dislocation density is the primary variable controlling the flow stress, but this does not address the actual evolution of the dislocation density with respect to a change in applied stress. Even though the role of GND and SSD densities is well understood with respect to their geometric implications, the ability to translate these definitions into meaningful density evolution equations remains elusive (Fleck et al. 2003). It is clear that hardening is due to trapping

of mobile dislocations with other mobile and immobile dislocations that form jogs, locks, and sessile junctions, thus increasing the dislocation density. However, it is not clear to what extent this occurs, and how it should be incorporated into the evolution of the isotropic and kinematic hardening of a spatially-dependent crystal plasticity model at each material point inside of the grain.

On the level of the grain, it is clear that there is a different strain hardening response associated with different grain sizes, as seen in Figure 4.7 below.

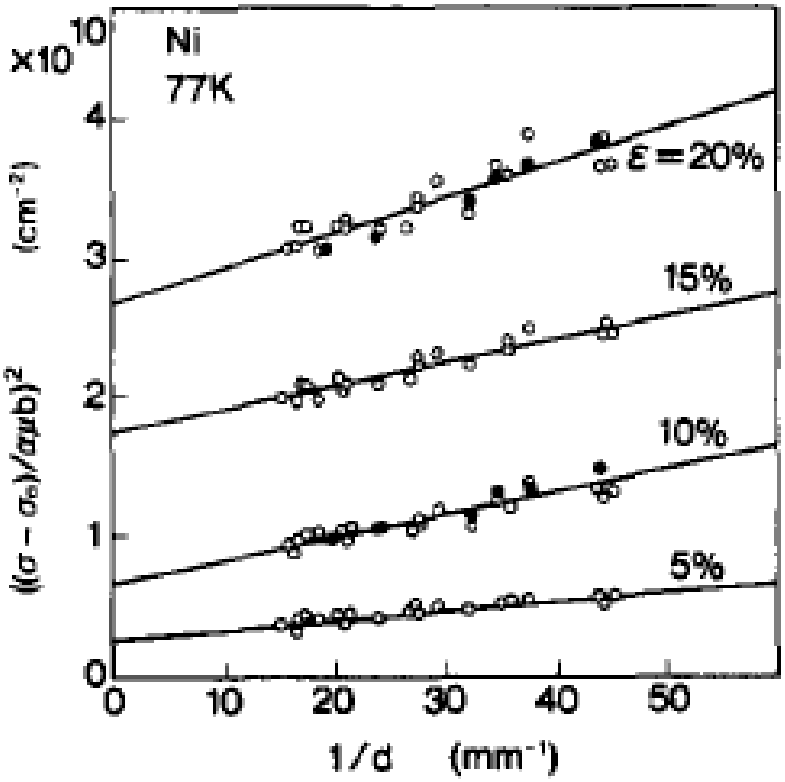

Figure 4.7. Increased normalized flow stress response of Ni at 77k as a function of inverse grain size at different strain levels from Narutani and Takamura (1991).

As straining increases, the effect of grain size becomes more pronounced on the hardening effect on flow stress. Specifically, as grain size decreases, the rate-independent work hardening increment increases.

Clearly, strain hardening after initial yielding is a multi-faceted issue whose origin extends from dislocation avalanches at the nanometer scale to accumulated plastic deformation at the macroscale. The statistical ensemble response of these dislocation avalanches manifest themselves in terms of average dislocation densities at each material point, which serve to increase the flow stress regardless of being geometrically necessary or statistically stored. Finally, the overall response of these dislocation densities and their response to an applied stress is governed by the crystallographic lattice and restrictions imposed on them by individual grains. In order to understand how the grain scale affects hardening rates, simple analytical models are used.

Analytical Hardening Models as a Function of Slip Line Length

Models describing the physical basis for strain hardening dependence on grain size stem from two historical models coined the "dislocation pile-up model" and the "work hardening model".

The dislocation pile-up model introduces the effect of the grain boundary on hardening by relating the number of dislocations that can pile up against a grain boundary to the size of the grain from which the dislocations are emitted. The long range stresses associated with the piled up dislocations induce an elastic stress on the neighboring grain, which therefore decreases the amount of stress required to nucleate dislocations in the neighboring grain, as seen in Figure 4.8 below.

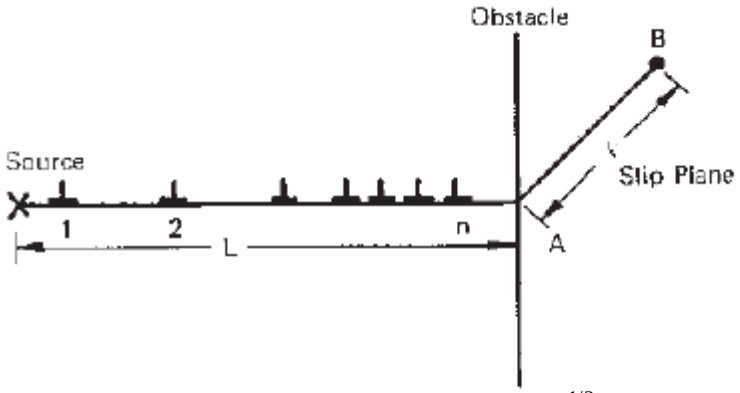

$$\sigma_{FLOW} = \sigma_0(\varepsilon, T, \dot{\varepsilon}) + K_1(\varepsilon, T, \dot{\varepsilon}) D^{-1/2}$$

Figure 4.8. Dislocation pileup model showing increased hardening due to piled up dislocations at grain boundary which acts as an obstacle (Conrad 2004).

In this form, a generalized Hall-Petch equation is derived as a function of the stress state, temperature, strain rate, and grain boundary length, all of which affect the evolution of the hardening.

While dislocation pile-ups are not widely experimentally observed, it is often used to justify a general version of the Hall-Petch relation for rate-independent low homologous temperature regimes at different strain levels

$$\sigma_{FLOW}(\varepsilon) = \sigma_0(\varepsilon) + K_1(\varepsilon) D^{-1/2} \tag{4.6}$$

where σ_0 is the flow stress derived from single crystals or coarse polycrystals which reflects yielding on the grain interior, and $K_1(\varepsilon)$ is the additional strengthening due to the presence of the grain boundary (Hansen 2004). The exponent on the grain diameter term is most widely represented as 0.5, but can range anywhere from 0.3 to 1.0 (Kocks and Mecking 2003).

The other main model used to justify grain size dependence of the work hardening rate is Ashby theory, which can be combined with the ideas of Conrad with respect to the slip line length to come up with a Conrad-Ashby (C-A) model of grain boundary hardening. In this model, the grain boundary has two major effects on the hardening (Conrad 2004). The first effect was introduced by Conrad and follows that with decreasing grain size the mean free path of dislocations decrease, thereby increasing the chance of becoming a *stored* dislocation due to the obstacle interaction. The second effect introduced by Ashby is that due to incompatibility that arises from the anisotropy of individual grains, GNDs must be created in order to satisfy compatibility across the grain boundary (Ashby 1970). For a smaller grain size, the compatibility requirements increase, therefore increasing the overall increase in dislocation density due to creation of GNDs. These ideas are illustrated together in Figure 4.9 below.

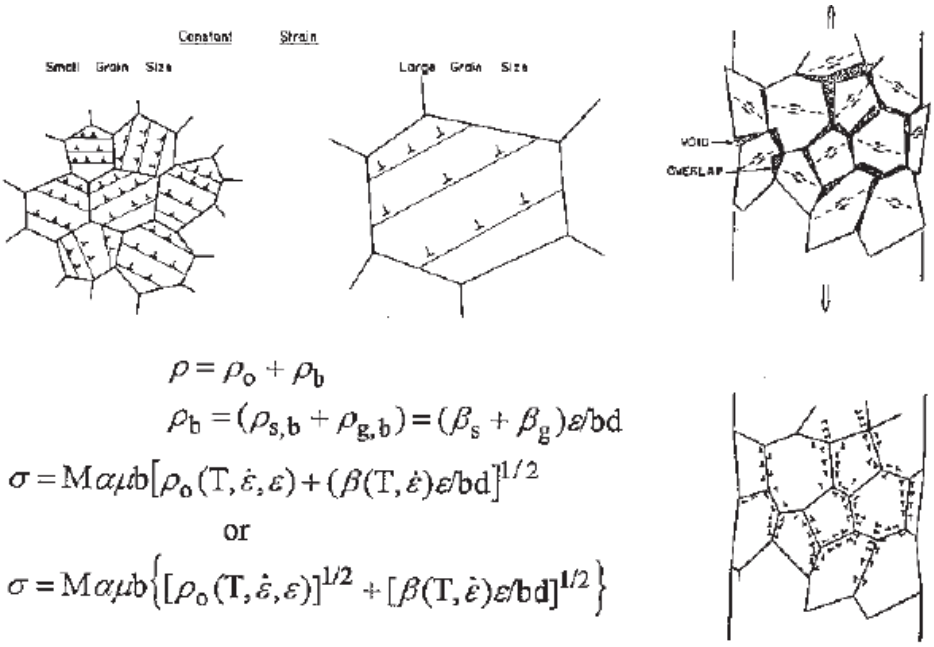

Figure 4.9. Conrad-Ashby (C-A) model used to predict grain boundary strengthening effect on strain hardening from Conrad (2004).

As was the case for the dislocation pileup model, the C-A model uses a combination of both grain boundary dependent and grain boundary independent terms that define the evolution of the strain hardening. Because the Conrad model states that the initial hardening rate is a function of slip line length, it is assumed that the general model for strain hardening should have a minimum initial value of hardening that is a function of single crystal or coarse grained polycrystalline tests and a separate term which has an inverse dependence with an indeterminate exponent that depends on the slip line length.

Further experimental evidence for the Conrad model that dislocations are stored more rapidly for decreased mean free path are shown in Figure 4.10 below.

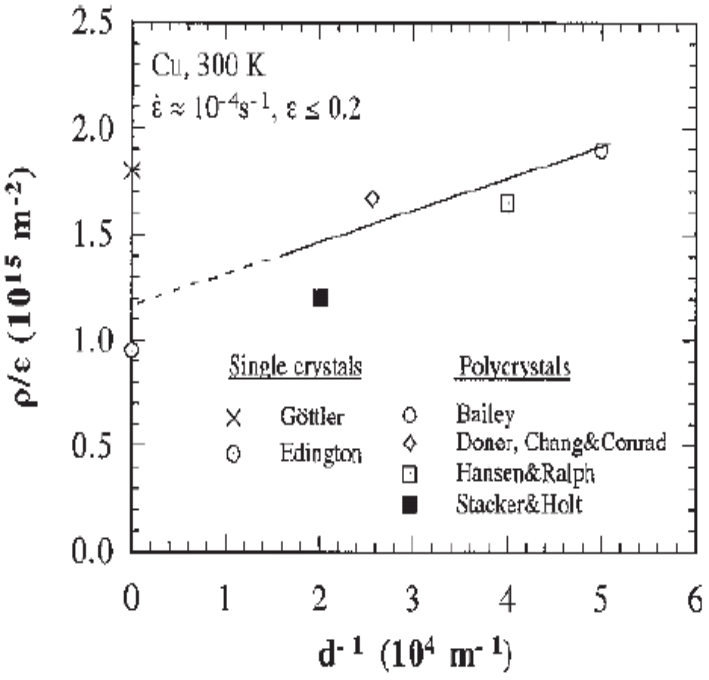

Figure 4.10 Experimental evidence of increased dislocation density accumulation to strain ratio for room-temperature, rate-independent deformation in copper polycrystals from Conrad (2004).

Also, the analytical model of Ohno and Okumura can be generalized for a flow stress dependence after yielding and cellular substructure formation dictates the dominant characteristic dimension in the polycrystals. When cellular sizes were mapped against the flow stress using the same equation from equation 4.1, the line Figure 4.11 was generated

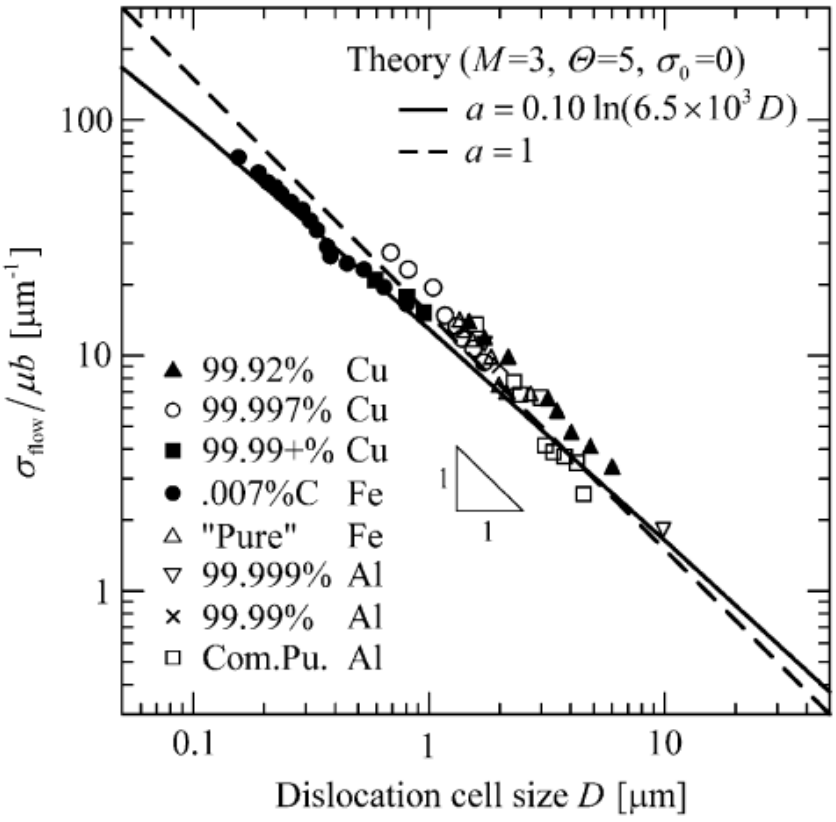

Figure 4.11. Flow stress plotted versus cell size from Staker and Holt (1972).

which justifies the use of the self energy of dislocations inside a grain as an appropriate measure of the flow stress for two orders of magnitude from 100nm - 5μm even after the material has deformed.

Clearly, there is a dependence of the hardening rate on the slip line length as has been shown from experimental, computational, and analytical observations, which needs to be implemented into a non-local crystal plasticity model in order to more accurately model the hardening dependence on slip length.

Because the slip line length is the projected length of a slip system and its intersecting obstacles, hardening relations must be used due to the inability predict the substructure formation and evolution, and therefore the projection of the slip line length and Dense Dislocation Walls, Geometrically Necessary Boundaries, and other obstacles to dislocation motion.

Slip Line Length Calculation

To calculate the mean free path of dislocations from the initial grain structure, a Voronoi Tessellation was used to construct a microstructure as was done during the parametric study of limited hardening. After the three-dimensional grains were constructed with random orientations, the free length of each slip system constrained by the grain boundary was found as shown in Figure 4.12 below.

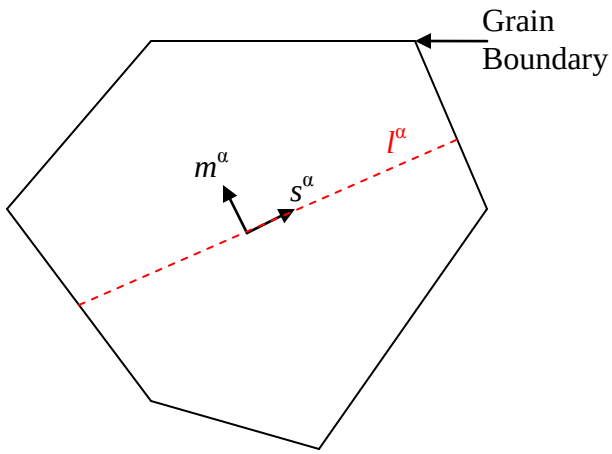

Figure 4.12. Schematic drawing showing slip projection length l^{α} from the grain center which is constrained by the grain boundary.

The projected slip line length for each grain is calculated from the center of the grain for all of the slip systems. The calculation of the length is done by finding the sum of the minimum lengths of intersection distances between a line projected in the positive and negative s^{α} direction from the grain center and all of the planes that defined the grain boundary planes. This is done using by using the equation for the location of an intersection between a line and a plane defined by three points at (Weisstein 2010).

Material parameters that have been justified to have a length scale dependence on l^{α} can be reformulated in the crystal plasticity framework such that they are all defined as some function of the slip line length. It should be noted that in the evolution of the drag stress according to a hardening-dynamic recovery law, both the initial hardening and saturation can be a function of l^{α}. Clearly, if a back stress and threshold stress are used in the crystal plasticity formulation, they can also be function of l^{α}.

Polycrystal Model Parametric Study and Motivation for Length Scale Dependent Model

From experimental and analytical observations, it is clear that initial yield strength and subsequent hardening are a function of not only grain size, but free mean path for dislocation glide. Before a crystal plasticity model is made with the analytical relations for hardening parameter dependence on mean free path for dislocation glide, a useful exercise is to enumerate the overall effect of using direct and inverse slip length dependencies on each of the material parameters, and to see what their effect is on the overall macroscopic stress-strain response for monotonic loading.

A microstructure with 50 grains is monotonically loaded in tension, has periodic boundary conditions, and is represented by 216 elements, and dependencies on these variables is explored and their overall macroscopic consequences will be shown with respect to a baseline case. The flow rule is

$$\dot{\boldsymbol{\gamma}}^{\alpha} = \dot{\gamma}_0 \left(\frac{\boldsymbol{\tau}^{\alpha}}{\mathbf{D}^{\alpha}} \right)^{m} \operatorname{sgn}\left(\boldsymbol{\tau}\right) \tag{4.7}$$

where different hardening relations for the drag stress that depend on the slip line length are used. The baseline variables are included in Table 4.1 below and are taken from (McGinty 2001).

Table 4.1. Material parameters for slip line length parametric study at room temperature

Parameter	**Units**	**Value**
C_{11}	GPa	150
C_{12}	GPa	75
C_{44}	GPa	37.5
$\dot{\gamma}_0$	s^{-1}	0.001
M	-	30
D_0	MPa	13
H_{DIR}	MPa	225
H_{DYN}	MPa	2.05
Ψ	Rads	0-2π
θ	Rads	0-π
ϕ	Rads	0-π
$q^{\alpha\beta}$	-	*1* for any *α,β*

First, the baseline variables were tested in monotonic tension with no slip line length dependence, and will be used to compare other responses of other hardening relations with. The effect of varying the direct hardening directly or inversely proportional to slip line length is parametrically studied for different values of the evolution of the drag stress

$$\dot{\mathbf{D}}^{\alpha} = \left(A + Bl^{\alpha} + \frac{C}{l^{\alpha}} \right) H_{DIR} \sum_{\beta=1}^{N} \mathbf{q}^{\alpha\beta} \left| \dot{\boldsymbol{\gamma}}^{\beta} \right| - H_{DYN} \mathbf{D}^{\alpha} \sum_{\eta=1}^{N} \left| \dot{\boldsymbol{\gamma}}^{\eta} \right| \tag{4.8}$$

where A, B, and C are used to control the dependence of the slip line length on the dependency of direct hardening on the slip line length. For example, with *A=1*, *B=0*, and *C=0* then the equation reduces to typical hardening with dynamic recovery. Two different sets of parameters were compared against the baseline in order to show the

effect of direct and inverse hardening dependence on slip line length as shown in Figure 4.13 below.

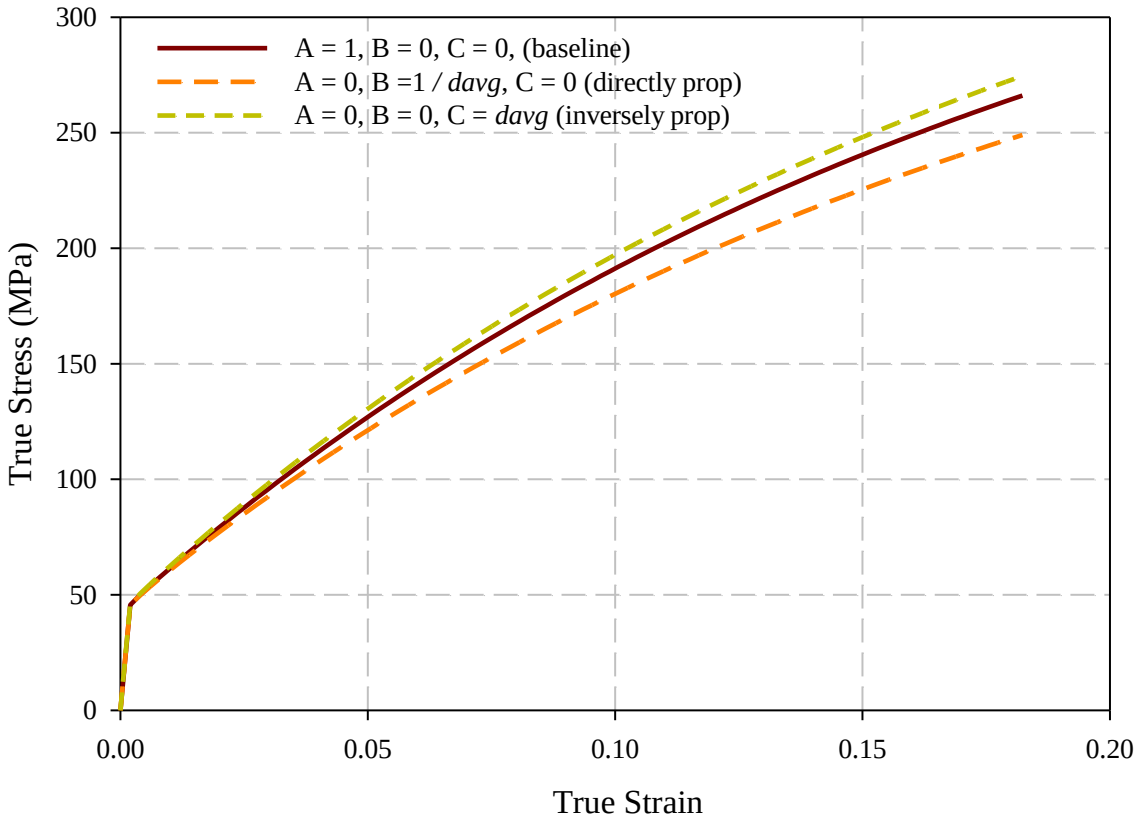

Figure 4.13. Macroscopic stress-strain response showing direct hardening dependence on slip line length.

Because of the units associated with B and C, they are both normalized by the average grain size versus the baseline case so that the case where the slip line length is equivalent to the average grain diameter yields the same response as the case for A = 1.

The same type of parametric study done for the effect on direct hardening was done for the effect of dynamic recovery on the slip line length

$$\dot{\mathbf{D}}^{\alpha} = H_{DIR}\mathbf{q}^{\alpha\beta}\left|\dot{\boldsymbol{\gamma}}^{\beta}\right| - H_{DYN}\mathbf{D}^{\alpha}\sum_{\eta=1}^{N}\left|\dot{\boldsymbol{\gamma}}^{\eta}\right|\left(A + Bl^{\alpha} + \frac{C}{l^{\alpha}}\right) \tag{4.9}$$

where A, B, and C were dimensioned the same and represented no dependence, direct dependence, and inverse dependence of the dynamic recovery coefficient on slip line length respectively. According to this set of evolution equations, the response of the system's dependence of the dynamic recovery coefficient on the slip line length is shown in Figure 4.14 below.

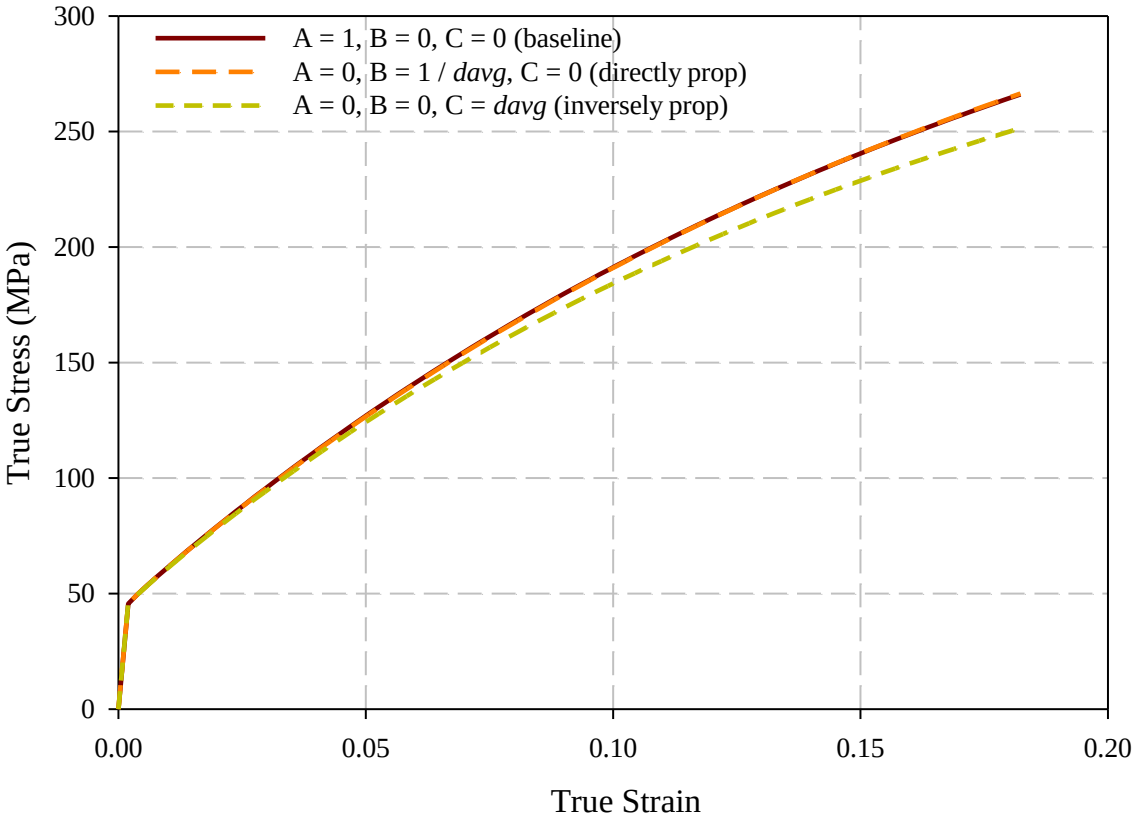

Figure 4.14. Macroscopic stress-strain response showing dynamic recovery dependence on slip line length.

With direct dependence of recovery on slip line length, there is no significant deviation from the average overall parameters.

Finally, the yield strength dependence on slip line length is reflected through the same sort of convention applied to the initial value of the drag stress

$$\mathbf{D}_0^{\alpha} = AD_0 + BD_0 l^{\alpha} + \frac{CD_0}{l^{\alpha}} \tag{4.10}$$

where once again A, B, and C are used to control the effect of each parameter. The macroscopic response of this slip length dependence is shown in Figure 4.15 below.

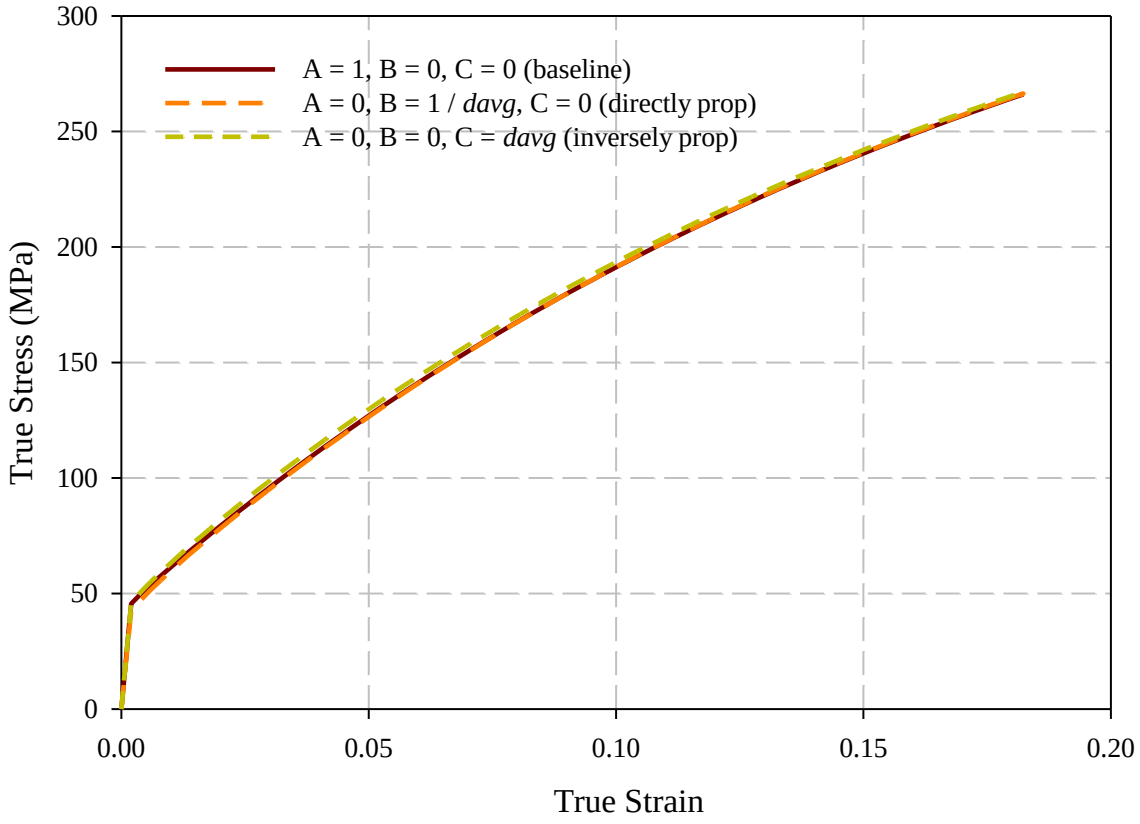

Figure 4.15. Macroscopic stress-strain response showing yield strength dependence on slip line length.

For the yield strength dependence on slip line length, there is little to no difference in the macroscopic response of the slip length model normalized by average grain size, and the average overall response.

For all three of the dependencies on slip line length, because there are 12 slip systems active, and only 5 or 6 are active during computational simulations of plastic deformation, even if a grain has heterogeneity in the form of the slip line length being

different on a few slip systems, it is overwhelmingly averaged out by the near grain diameter dimensionality.

In order to get a non-uniform mesoscale response, and in light of the experimental and analytical models for both yield strength and hardening rate dependence on slip line length, a non-uniform model will be introduced in order to more accurately represent the inhomogeneity due to the position inside of the grain similar to (Kumar et al. 2006).

Non-Uniform Slip Line length Formulation

In order to better reflect the heterogeneity in the grain provided by each point's proximity to the grain boundary, the slip line length l^{α} for each slip system was calculated at the centroid of each individual element inside of the grain and not just assumed to be the same for every element inside the grain calculated at the grain center in the previous local slip line length formulation. This method can be seen schematically in Figure 4.16 below.

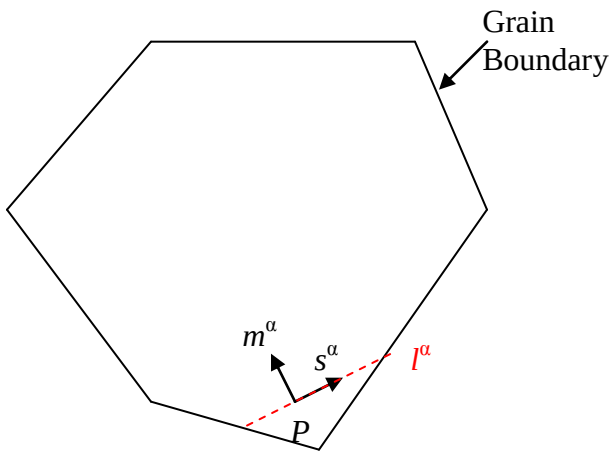

Figure 4.16. Schematic drawing showing non-uniform slip projection length l^{α} at a particular point P in the grain of the α^{th} slip system.

The same material variables and evolution equations for the evolution of the drag stress are used here as was done for the local slip line length model, with the only difference being that the slip line length is calculated at each element inside of the grain instead of at the grain center. The direct hardening dependence on slip line length normalized by the average grain size is shown in Figure 4.17 below.

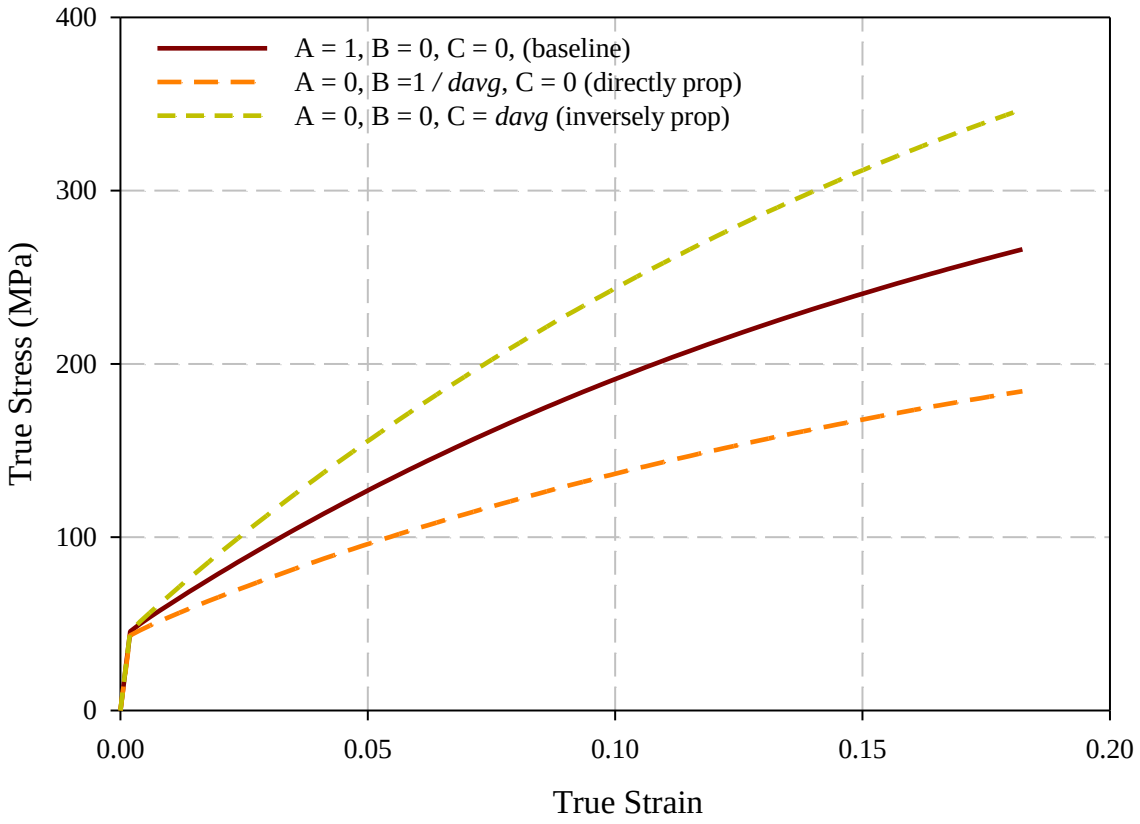

Figure 4.17. Macroscopic Stress-strain response showing direct hardening dependence on slip line length evaluated at each material point.

The non-uniform slip line length formulation clearly offers greater variance than the grain-center slip line length. It is clear from insight and verified by the macroscopic

stress-strain response that the average slip line length in the heterogeneous calculation is less than that when calculated through the grain center.

Similarly to the yield strength test, the average response when the dynamic recovery of the hardening is varied proportionally to the slip line length normalized by the average grain diameter is included in Figure 4.18 below.

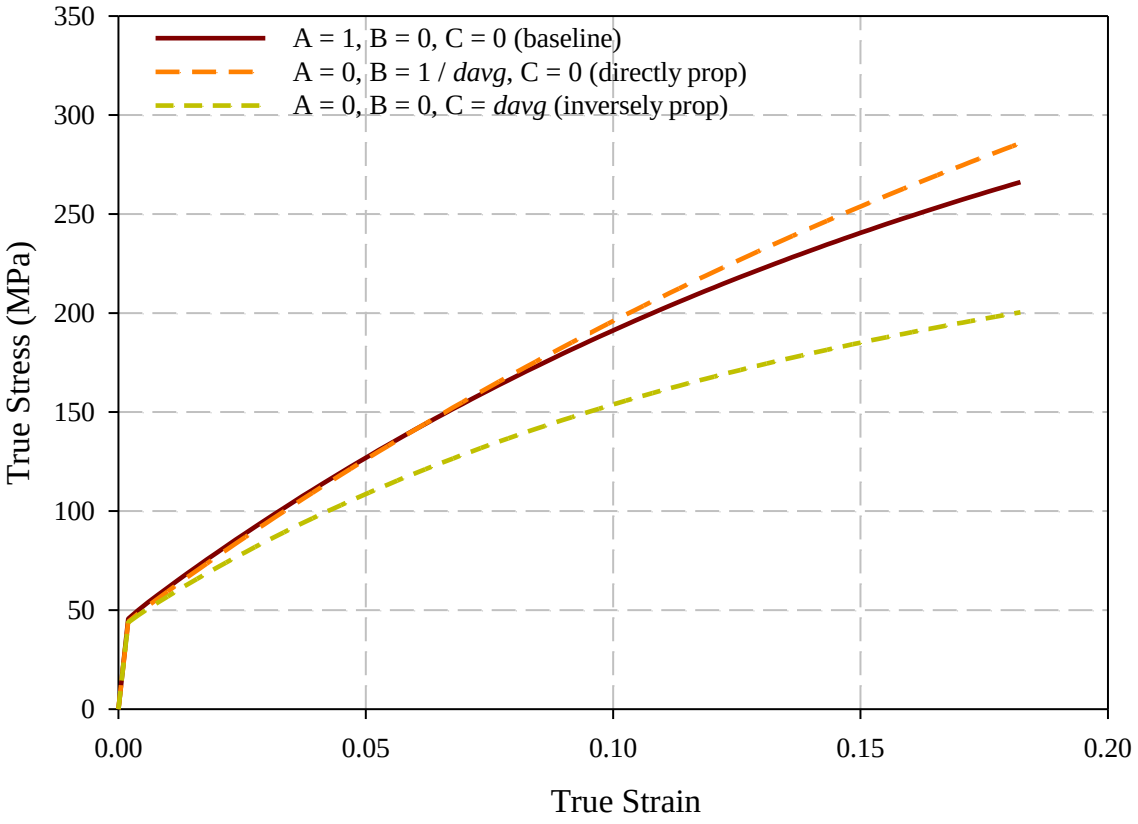

Figure 4.18. Macroscopic Stress-strain response showing dynamic recovery dependence on slip line length evaluated at each material point.

As is expected, the inversely proportional dynamic recovery equation yields faster hardening saturation, and the directly proportional dynamic recovery equation yields slower hardening saturation. This effect is explained once again by the average slip line length for the non-uniform model being less than the average grain diameter.

Finally, the yield strength dependence on slip line length was tested in the same manner and the results are shown in Figure 4.19 below.

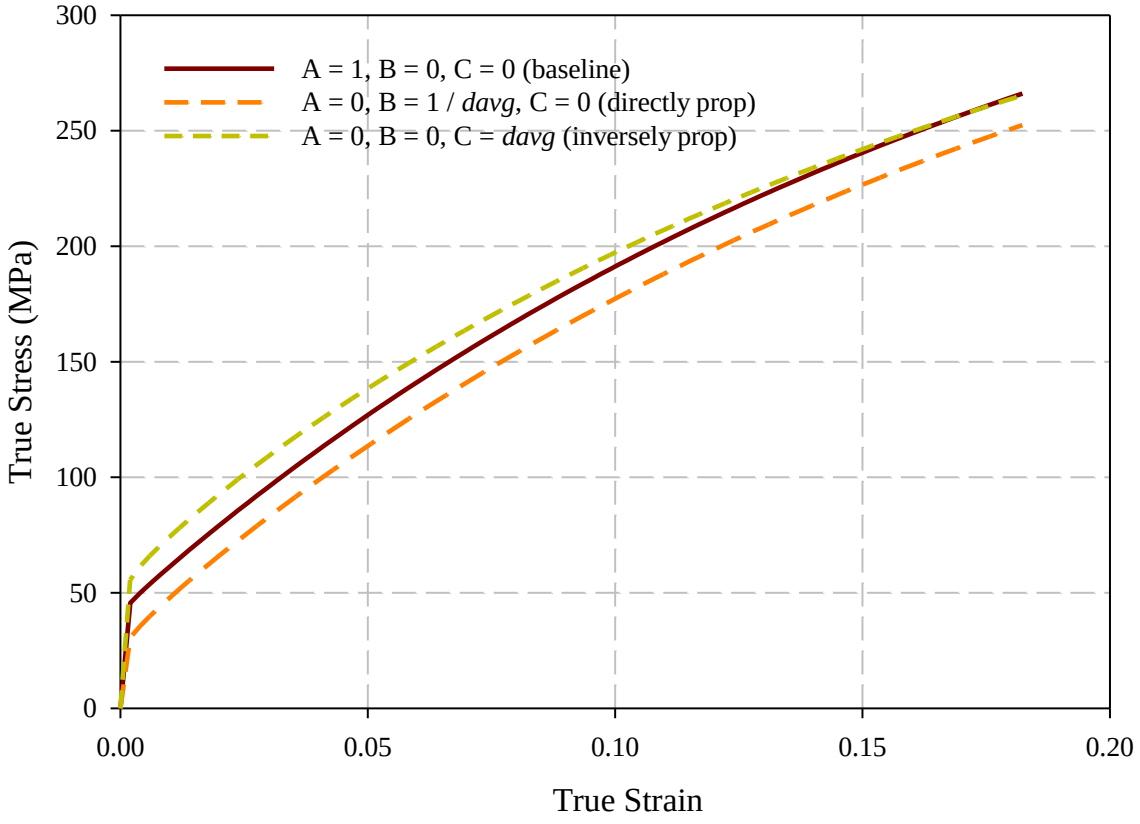

Figure 4.19. Macroscopic Stress-strain response showing yield strength dependence on slip line length evaluated at each material point

As expected, the material yielded at a lower stress for the direct slip line length dependence, and at a higher stress for the inverse slip line length dependence.

From observations of the macroscopic response of both the non-uniform and grain center uniform slip line length models, it is clear that the non-uniform model offers more variation due to the grain structure, and that in order to capture the non-uniform mesoscale response of the grain, the model that gives a new level of information in

accordance with experimental, computational, and analytical observations of preferential spatial yielding and hardening in the grain is the non-uniform slip line length model.

Model With Non-Uniform Subgrain Initial Slip Line Length Assignment

A crystal plasticity model is constructed with yielding and hardening parameters as dependent functions of the initial slip line length, which can then be compared to macroscale deformation experiments.

The crystal plasticity model used will follow the crystal plasticity framework where the only parameter that evolves is the drag stress, i.e.,

$$\dot{\boldsymbol{\gamma}}^{\alpha} = \dot{\gamma}_0 \left(\frac{\boldsymbol{\tau}^{\alpha}}{\mathbf{D}^{\alpha}} \right)^{m} \operatorname{sgn}\left(\boldsymbol{\tau}^{\alpha} \right) \tag{4.11}$$

where the drag stress will evolve according to a Fredrick-Armstrong type hardening law

$$\dot{\mathbf{D}}^{\alpha} = \sum_{\beta=1}^{N} \left(\mathbf{H}^{\alpha}_{DIR} \mathbf{h}^{\alpha\beta} - \mathbf{H}^{\alpha}_{DYN} \mathbf{D}^{\alpha} \right) \left| \dot{\boldsymbol{\gamma}}^{\beta} \right| \tag{4.12}$$

with the crystal plasticity parameters defined Table 4.2 below for quasi-static loading of copper polycrystals.

Table 4.2. Crystal Plasticity parameters for isotropic polycrystal from (McGinty 2001)

Parameter	**Units**	**Value**
C_{11}	GPa	150
C_{12}	GPa	75
C_{44}	GPa	37.5
$\dot{\gamma}_0$	s^{-1}	0.001
m	-	30
$h^{\alpha\beta}$	-	1 for all α,β

From the analytical and experimental observations of deformation at the mesoscale three conclusions about crystal plasticity parameters can be made:

1) The initial drag stress which corresponds to the yield strength follows a classical Hall-Petch relation in terms of slip line length for grain sizes larger than 1 μm such as

$$\mathbf{D}_{Y,0}^{\alpha} = D_{Y,0} + \frac{K_Y}{\sqrt{l^{\alpha}}} \tag{4.13}$$

2) The direct hardening parameter H_{DIR} is inversely proportional to the slip line length due to the increased probability of dislocations being stored with decreasing free path length such as

$$\mathbf{H}_{DIR}^{\alpha} = H_{DIR,0} + \frac{K_{DIR}}{l^{\alpha}} \tag{4.14}$$

3) The dynamic recovery is inversely proportional to the slip line length due to the fact that increased free path length corresponds to a larger number of dislocations able to accumulate on that slip line before saturation occurs. This formulation is represented numerically as

$$\mathbf{H}_{DYN}^{\alpha} = H_{DYN,0} + \frac{K_{DYN}}{l^{\alpha}} \tag{4.15}$$

In order to match experimentally observed macroscopic behavior, these parameters are fit in a top-down approach to experimental data obtained from tension experiments on polycrystalline Ni at 77K from Narutani and Takamura (1991) which studied the effect that grain size has on hardening behavior. The parameters that were used to fit the data to this experimental study and are included in the crystal plasticity formulation are included in Table 4.3 below.

Table 4.3. Parameters for non-uniform crystal plasticity model derived from Ni Experiments at 77K.

Parameter	**Units**	**Value**
$D_{Y,0}$	MPa	10.2
K_Y	$\text{MPa}\sqrt{\text{mm}}$	3.1
$H_{DIR,0}$	MPa	338
K_{DIR}	MPa • mm	0.25
$H_{DYN,0}$	MPa	1.0
K_{DYN}	MPa • mm	2.0

With these material parameters derived from a top-down manner and their relations inferred from bottom-up analytical models, a combined top-down, bottom-up, non-uniform crystal plasticity model is created for polycrystalline deformation of Ni at 77K. To see the usefulness of this model, simulations are run on 174 a grain representative volume element represented by 512 elements with different average grain sizes. The macroscopic deformation at different strain levels is measured, and compared to experimental data, as seen in Figure 4.20 below.

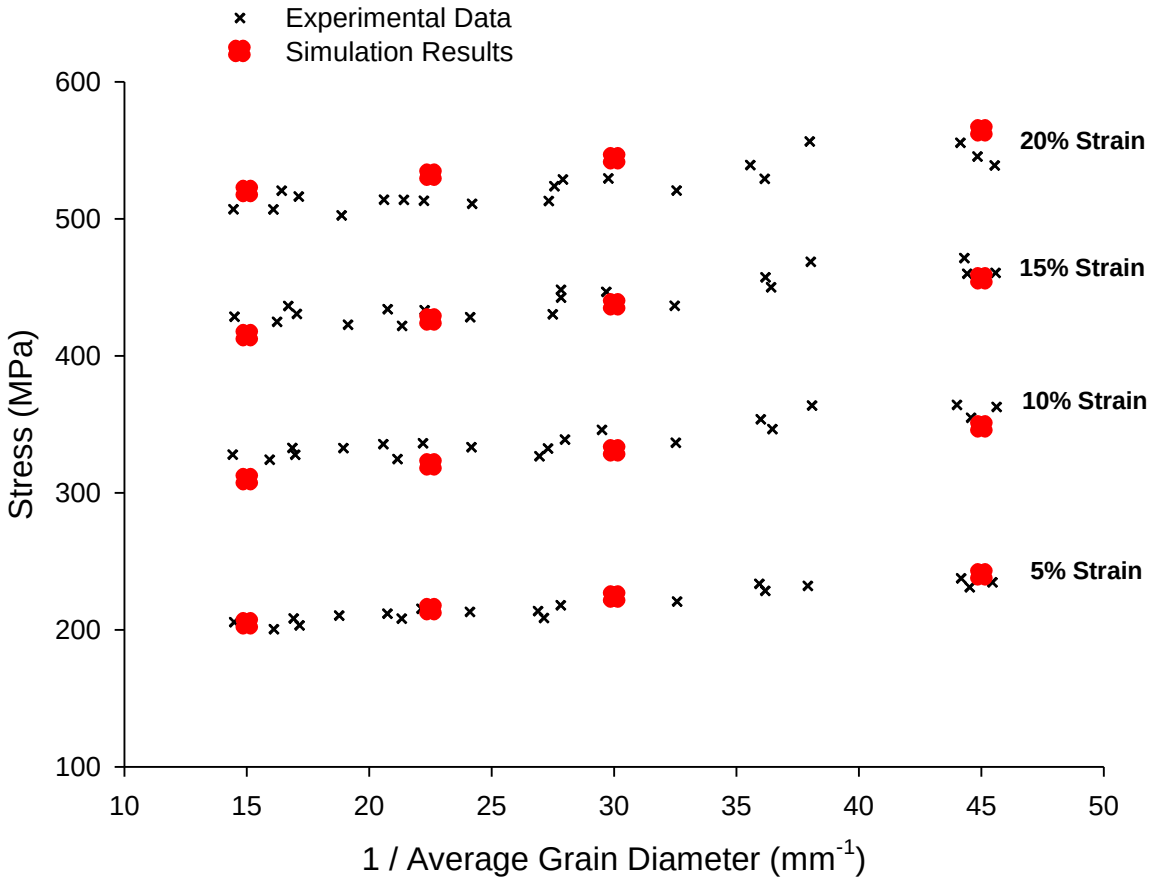

Figure 4.20. Stress compared to inverse grain diameter at different strain levels for Ni at 77K in experiments from Narutani and Takamura (1991) and from crystal plasticity simulations.

Figure 4.20 shows that the parameters inferred from top-down experimental observations put into the non-uniform slip line length model very accurately model the macroscale stress-strain response for different size grains. Furthermore, this implies that a heterogeneous slip line length model can be used to accurately relate the effect of differential yielding and subsequent hardening inside of the grain using the relations inferred from experimental and analytical observations of mesoscale deformation, and correlated through top-down parameter matching

Therefore, a comparison of the experimental results and simulations show that a non-uniform crystal plasticity formulation that parameterizes the size-effect on deformation processes at the mesoscale through incorporation of slip line length is an effective combined top-down, and bottom-up technique for incorporating the effect that a characteristic length at smaller scales than the grain size can have on macroscopic elastic-plastic deformation processes. The model is both top-down and bottom-up in that the material parameters were inferred from observations of mesoscale deformation and then fit to macroscale component level data.

Slip Line Length Model with Limited Slip Motivation

As has already been motivated from previous discussions during Chapter 3, limiting the number of active slip systems can be used to induce subgrain rotation; however, in the context presented in Chapter 3, non-uniform subgrain rotation is not a prominent effect due to the uniform assignment of material properties. With the framework from the projected slip line length in place to implement a length scale dependent limited slip model, the consequence of limiting slip inside of the grain can be further explored.

It is noted that a non-uniform limited slip model falls into models that explore the consequences of compatibility constraints. Parallel to motivation for this model to explore subgrain and macroscale texture evolution dependence on compatibility requirements are self-consistent models by Clausen et al. (1998) and more recently by Musienko et al. (2007) along with experimental studies on the number of active slip

systems and their effect on subgrain rotation (Tatschl and Kolednik 2003) and studies of crystal plasticity compared to subgrain rotations (Buchheitet al. 2005).

In order to formulate where regions of limited slip should occur, a Core-Mantle approach is used following Meyers and Ashworth (1982), as it is consistent with the elements of the CA hardening model that depends on the projected slip line length, and is illustrated qualitatively in Figure 4.21 below.

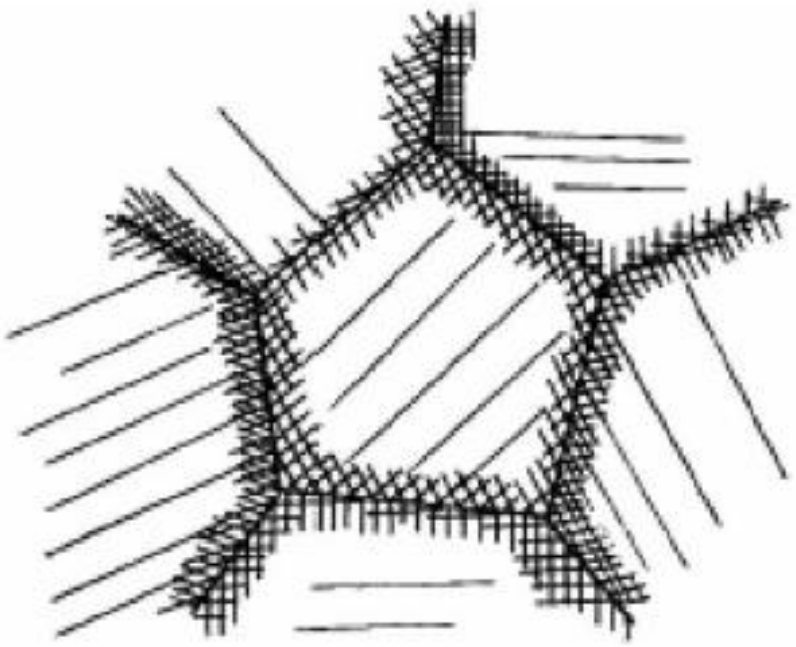

Figure 4.21. Core-Mantle model showing limited slip on the interior section, and multiple slip near the grain boundary from Meyers et al. (2006)

Using this model, it is clear that there is a region near the boundary in which multiple slip occurs, which corresponds to increased hardening rates and yield strength, and a region dominated by single or double slip, which corresponds to decreased hardening rates and yield strength. Qualitatively, multiple slip is driven by either the existence of dislocation sources such as ledges in the grain boundary or increased

compatibility requirements necessitating multi-slip due to elastic mismatch from grain orientations. Because the core region is uniform with less compatibility requirements, multiple slip is not prevalent at initial stages of yielding. From this model, as the grain diameter is decreased, so is the percentage of the grain that corresponds to the core, and therefore multiple slip is seen as a dominant feature. It should be noted that there is an obvious limitation to this model in the nanoscale regime due to the fact that once dislocations are no longer the main source of plastic deformation this model is inherently unable to connect to this regime.

Non-Uniform Limited Slip Model Formulation and Results

From studies done in Chapter 3, it is clear that hardening can be formulated in terms of the inability for plastic deformation to satisfy compatibility and through hardening relations that parameterize the dislocation-dislocation interactions throughout the course of deformation. In order to clearly understand the effect that these different hardening types have on the texture evolution of polycrystalline Cu, three different hardening formulations and their effect on texture evolution need to be compared: hardening solely due to plastic incompatibility; hardening due to combined plastic incompatibility and hardening laws; hardening solely due to hardening laws. In order to assure that differences in texture evolution are not due to the macroscopic stress-strain response, the formulations also need be fit so that their macroscopic responses are similar.

In order to compute the distance to the grain boundary at any point inside of the grain, the projected slip line length was calculated in both the positive and negative direction for all 12 slip systems, and the minimum of these 24 values was used for that

point in order to compute the minimum distance to a boundary, represented by $l_{\min}$, as

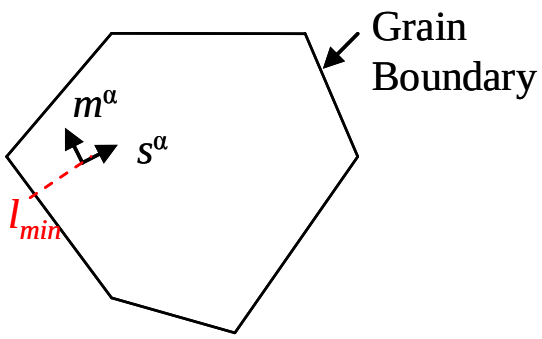

Figure 4.22. Schematic of minimum slip line length l_{min}.

seen in Figure 4.22 below.

Note that this differs from the measure of the total slip line length, which for each slip system is the sum of the positive and negative components.

To ensure that the texture evolution induced by the different types of hardening are the only source of variability between the different simulations, 50 grains and 1000 cubic C3D8 elements are used to simulate the tensile deformation of a 100 μm block, thus corresponding to an average grain size of 33.6 μm. Also, since the limited slip formulation is being used self-hardening is assumed, i.e., $\mathbf{q}_{\alpha\beta} = \boldsymbol{\delta}_{\alpha\beta}$.

A non-intuitive aspect which must be examined is the distribution of both the slip line length and the minimum distance to the boundary, as seen in Figure 4.23 below.

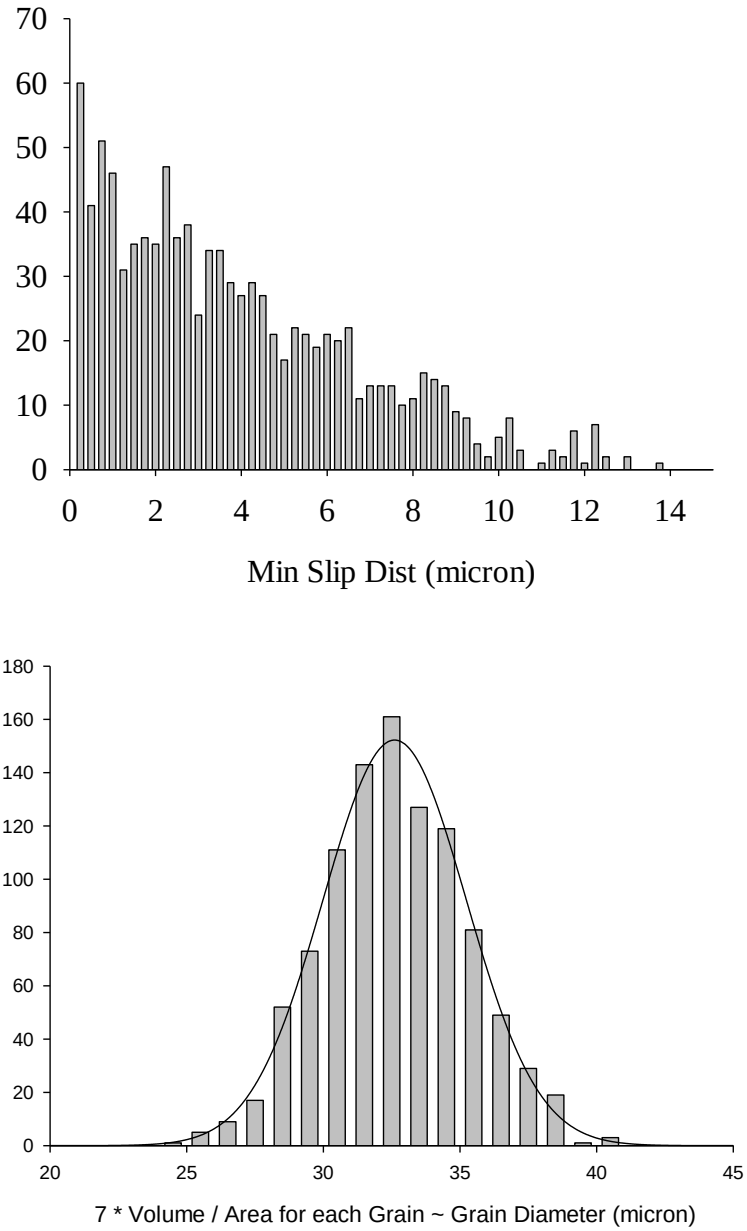

Figure 4.23. Minimum slip distance l_{min} and average grain diameter for 1000 elements representing a 100 micron cube, which corresponds to an average grain size of 33.6 μm.

While the grain diameter for an unweighted Voronoi Tessellation follows a normal distribution, the minimum slip line length l_{min} follows a different distribution which is not entirely intuitive. Also, this is not an artifact of mesh size, as the slip line length is calculated before the space is discretized by elements. An increased mesh size results only in a smoother histogram with the same fundamental shape.

With the distribution of length scales in hand, all that is left is to define the three models. In order to enforce limited slip on both the model with hardening due to limited slip only, and the model with combined hardening evolution along with limited slip, a simple algorithm is used, i.e.,

$$\begin{aligned} &\text{if} \quad l^P_{\min} \le \varphi: \; N_{ACTIVE} = 6 \\ &\text{if} \quad l^P_{\min} \ge \varphi: \; N_{ACTIVE} = 2 \end{aligned} \tag{4.16}$$

where $l^P_{\min}$ is the minimum slip distance evaluated at the center of every element, and φ is a threshold that defines distance where the grain boundary region ends. For the case where hardening is only due to the evolution of the hardening parameters, $N_{ACTIVE} = 12$.

Using these parameters, the non-uniform material parameters were fit so that the macroscopic stress-strain response of the three cases was very similar, and matched closely to experimentally observed strain levels for 33μm grains from Narutani and Takamura (1991) as seen in Figure 4.24 below.

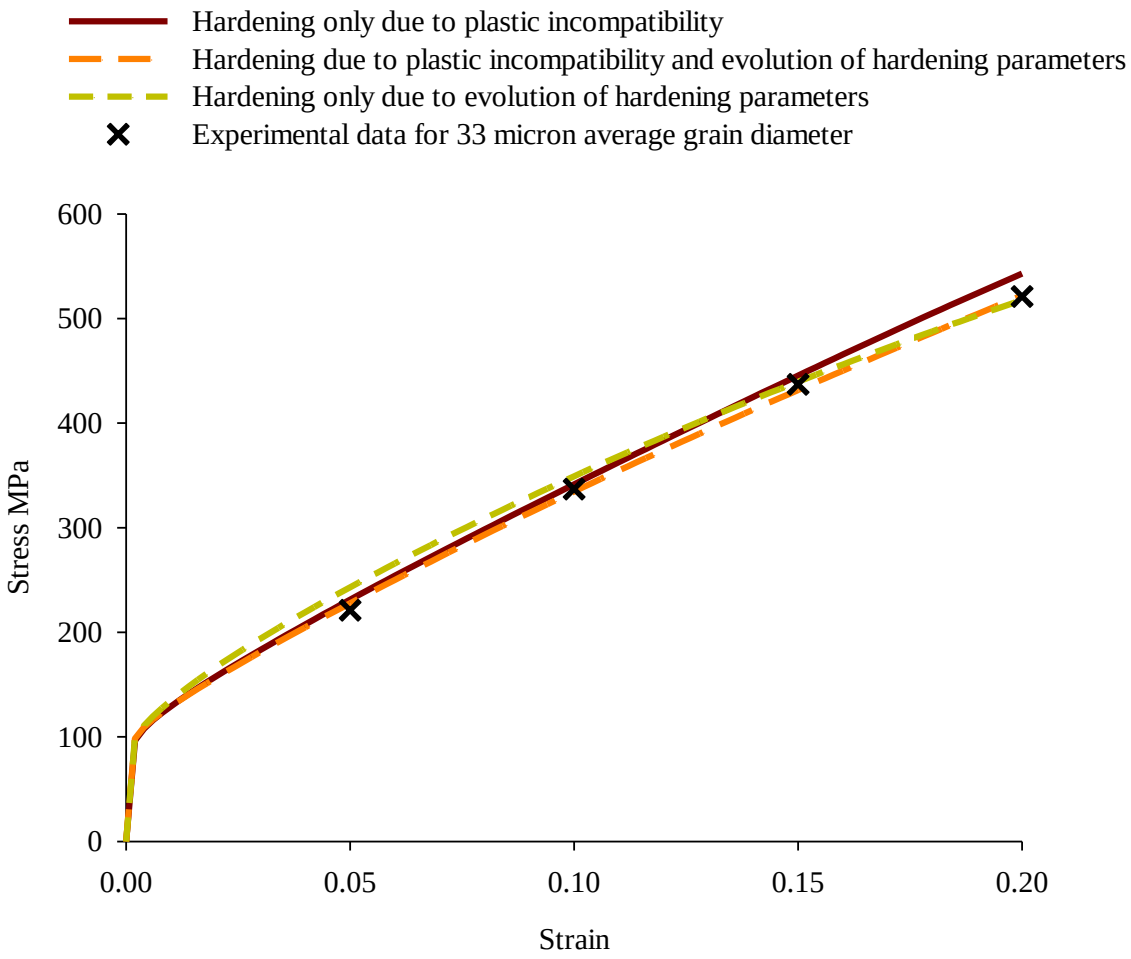

Figure 4.24. Comparison of macroscopic stress-strain response for three different types of hardening with average grain size of 33μm, and experimental data of stress-strain response of Ni at 77K.

The non-uniform material parameters used to create these similar stress-strain curves for the three different models are included in Table 4.4 below.

Table 4.4. Material properties for plastic incompatibility hardening (PIH), mixed hardening (MH), and parameter evolution hardening (PEH) models for 33μm grain size.

Parameter	**Units**	**PIH Model**	**MH Model**	**PEH Model**
$D_{Y,0}$	MPa	8.0	8.0	8.0
K_Y	MPa • mm1/2	4.0	4.0	4.0
$H_{DIR,0}$	MPa	0.0	600	1400
K_{DIR}	MPa • mm	0.0	10.0	13
$H_{DYN,0}$	MPa	0.0	0.0	0.0
K_{DYN}	MPa • mm	0.0	0.0	0.0
φ	μm	1.8	6.0	N/A

Looking at the parameters in Table 4.4 and the minimum slip line lengths in Figure 4.23, about one fifth of the grain is part of the grain boundary region where multislip occurs for the PIH model, whereas for the MH model three quarters of the model is part of the grain boundary region that can undergo multislip. For the PEH model, since all slip systems are assumed to be active, there is no threshold φ, and therefore all elements have all 12 slip systems active.

From the macroscopic stress-strain response of the same, clearly the magnitudes of the overall force-displacement response are the same, so the earlier assertion that limited slip is a driving force for subgrain rotation can be studied solely with respect to the different hardening types.

In order to examine the effect of hardening type on driving force for subgrain rotation, the same realization was tested to 36% compressive strain in the z direction using the three different models, and the {1 1 1}, {1 1 0}, and {1 0 0} pole figures for all three cases were plotted with respect to the initial configuration, -11% strain, and -22% strain, and -36% strain as seen in Figures 4.25, 4.26, and 4.27 below. For the following

three figures, all of the computational models, which are colored, use the same scale for all of the models in the figure, but are different from figure to figure. Also, each row corresponds to an equivalent strain level, and each column corresponds to the model used. Note that from left to right, the ability for plastic deformation to be accommodated decreases. Finally, the models are compared to experimental pole figures of OFHC Cu in compression, which has a similar texture evolution to Ni. All of the experimental pole figures are from (Bronkhorst et al. 1992).

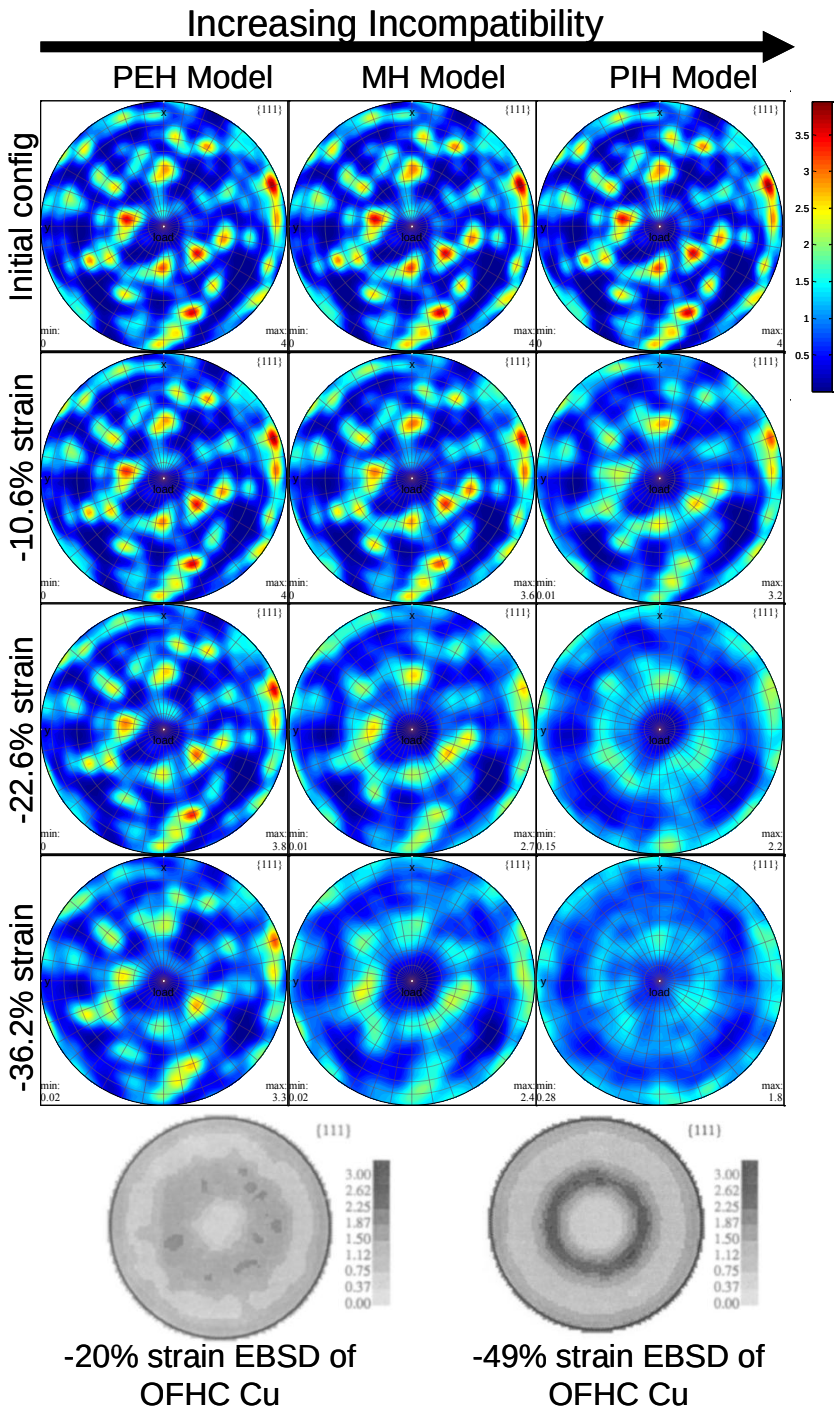

Figure 4.25. Computational {1 1 0} pole figures of Ni at 77K in compression for three different models compared to experimental pole figures of OFHC Cu in compression.

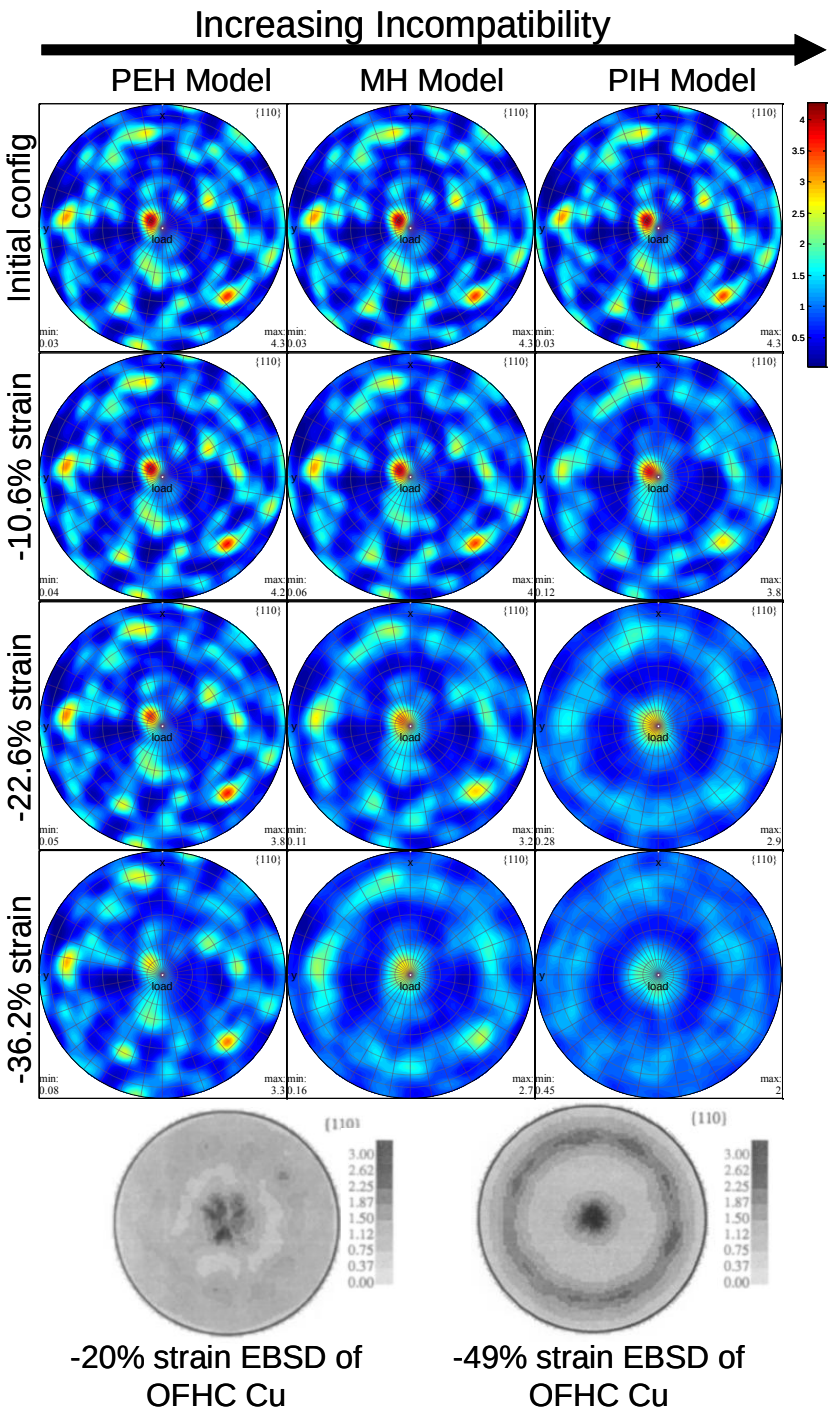

Figure 4.26. Computational {1 1 1} pole figures of Ni at 77K in compression for three different models compared to experimental pole figures of OFHC Cu in compression.

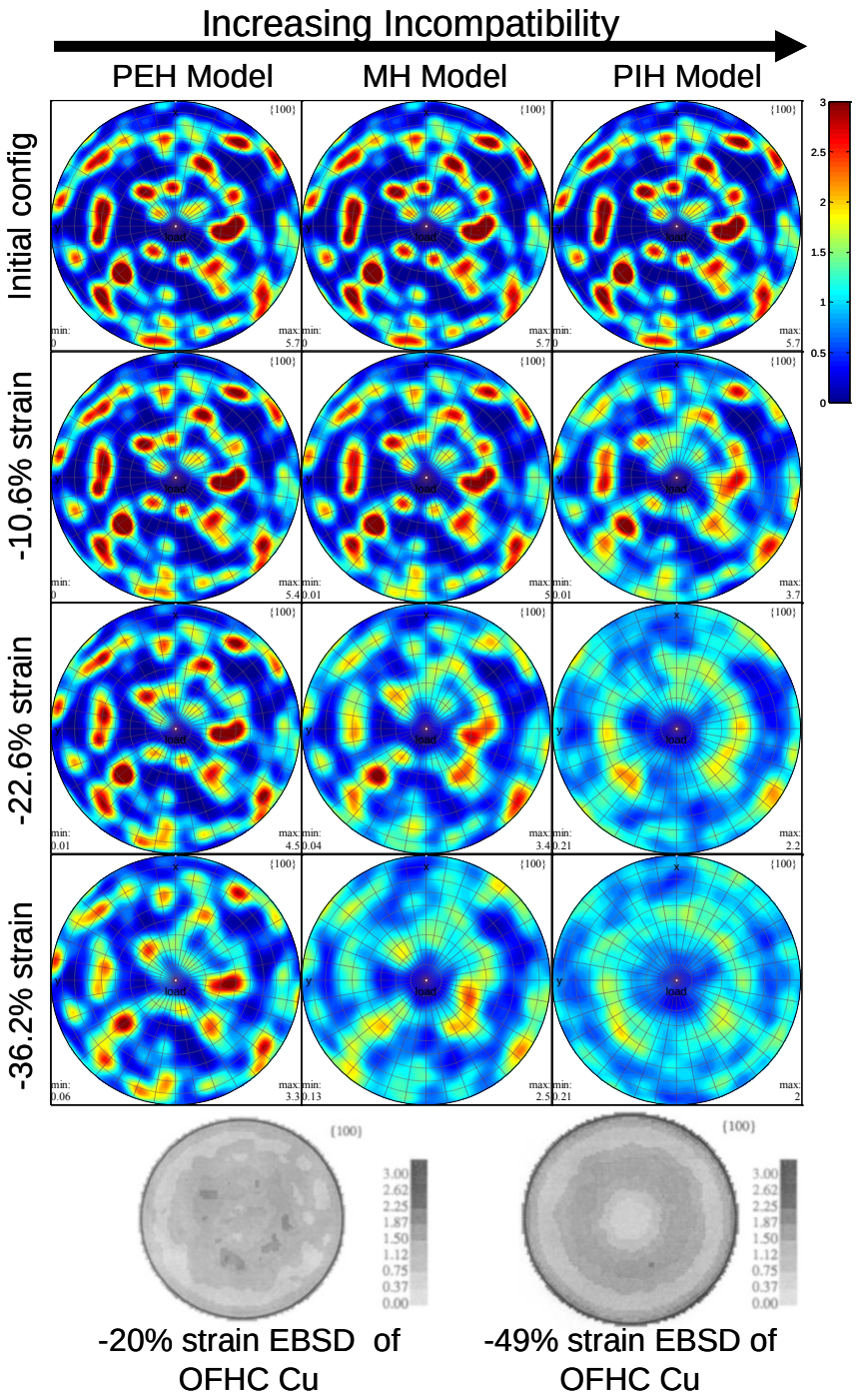

Figure 4.27. Computational {1 0 0} pole figures of Ni at 77K in compression for three different models compared to experimental pole figures of OFHC Cu in compression

From looking at the plots in Figures 4.25-4.27, it is apparent by comparing the PIH model to the PEH model that limiting the number of active slip systems necessitates an increase in the elastic stress in order to satisfy compatibility, which serves as a driving force for subgrain rotations. As strain progresses, for the PIH model, the angles bear less and less of a resemblance to the initial texture. Also, due to a lack of coherency of plastic networks that can bridge multiple grains, the sub-grain orientations seem to evolve in a less ordered manner, which mimics orientation changes that could form geometrically necessary boundaries, cells walls, or other sub-grain structures.

As the volume fraction of the grain that undergoes limited slip decreases, as is the case when going from the PIH to the MH model, the magnitude and non-uniformity of the rotations from the initial configuration decrease. Finally, going from the MH to the PEH model, the initial and final configurations bear more of a resemblance to one another, and both the magnitude and non-uniformity of the rotations decreases again.

Both PIH model and PEH serve as bounds in which the compatibility plays the entire, and the smallest roles possible respectively. It is clear that even if the PIH model captures the initial behavior adequately, evolving hardening parameters must be introduced in order to correct for the change in mean free path of dislocations, because the PIH model is only capturing the initial geometry. Also, the PEH model is not effectively incorporating the role of compatibility at all, and therefore will not accurately capture the role of substructure formation on subgrain rotations. Because these two are the bounds, a MH formulation is the most appropriate model that can be used to incorporate both the effect that compatibility has on the non-uniform subgrain rotations, as well as the overall effect of substructure formation on the macroscopic stress-strain

hardening response. Therefore, a MH formulation is suggested as necessary for further exploration.

CHAPTER 5: CONCLUSION

The effectiveness of crystal plasticity models is rooted in their ability to model deformation processes of the mesoscale and be incorporated into the macroscale. Traditional crystal plasticity models use a top-down approach of modeling mesoscopic deformation processes based on crystallographic information, and matching this information with a continuum approach and then informing the parameters in the constitutive relation through macroscale stress-strain testing. To more accurately model subgrain deformation processes through this parameter testing methodology, mesoscopic models revealing non-uniform meso-scale properties are considered and their effect is introduced through a combined top-down, bottom-up crystal plasticity model.

Summary of Novel Contributions

In this work, two different aspects of models motivated by experimental and analytical observations of mesoscale deformation were introduced. In the first exploration, slip was limited to less than five slip systems at each material point, which is physically observed in both single and polycrystal models. A summary of the macroscopic stress-strain consequence of limiting the number of active slip systems was presented in terms of the compatibility requirements imposed throughout the course of deformation. With no compatibility requirements for single crystals, limiting slip had a negligible effect; however, when increased constraints were placed on the single crystal, it mimicked the macroscopic response of polycrystals. Next, the average magnitude of the change in orientations due to the elastic stress required to satisfy compatibility in a polycrystal was presented, and examined with respect to experimental observations of

changes in rotation. From these initial investigations, it was shown that limiting the number of slip systems in combination with imposed compatibility requirements can increase the magnitude of rotations. The average change in subgrain rotations that were observed in the limited slip cases were much closer to experimental observation of subgrain rotation than the change in subgrain rotations induced when all of the deformation after yielding was accommodated through plasticity.

Therefore, the contributions of the limited slip study were twofold: one, that the effect of limiting the number of active slip systems was presented in a thorough fashion; and two, the magnitude of the change in subgrains rotations experimentally observed matched the limited slip case more closely than the case where slip was not limited, which suggests that conventional crystal plasticity does not accurately treat compatibility requirements.

The second aspect of models built upon earlier work of Kumar et al. (2006) involved assignment of initial free slip line length as a means to account for non-uniform yielding and subsequent hardening inside the grain. By making yielding and subsequent hardening relations a function of the projected initial slip line length of each slip system, aspects of non-uniform mesoscale deformation processes were incorporated. Therefore, a computational framework was created in which a non-uniform length scale was measured throughout the grain.

The length-scale dependent model was then fit in a top-down approach to experimental data, which was reproduced using relationships from mesoscale analytical models combined with heterogeneity provided by length scale incorporated through projected slip line length.

Finally, these two aspects of models were incorporated to study the effect of incorporation of hardening by either elastic stresses introduced due to the inability to satisfy plastic deformation, evolution of hardening parameters with plastic compatibility, or a combination thereof. The evolution of rotations induced by limiting the number of active slip systems based on a Mantle-Core model was studied and compared to mixed hardening and traditional hardening models. Furthermore, these models were also compared to experimental EBSD measurements from OFHC Cu compression experiments. From looking at these sets of pole figures, the inability to satisfy plastic deformation throughout the specimen increased both the magnitude and heterogeneity of rotations as deformation proceeded.

Future Work and Recommendations

Future work in both of these areas focuses in the area of mesoscopic deformation. While the initial slip line length model was correlated to monotonic deformation data, the question remains as to whether these parameters could be extrapolated in order to replicate complex loading histories. Because only the initial slip line length is used, and not an updated version, it is not known what extent these initial parameters have on a heavily deformed material. A limit in which the initial slip line length has no bearing on subsequent deformation must be found, so that the model's applicability can be assigned accordingly. The heterogeneity provided by the initial slip line length would have immediate application in determination of initial yielding or high cycle fatigue data, in which there is little change from the initial configuration, and a high dependency on magnitudes of localized deformation.

In terms of application for non-uniform limited slip and its effect on surrounding areas, multiple areas of interest exist. Computational experiments should be performed to simulate small crack growth, in which one or two slip systems are dominant. The resulting change in microstructure due to limited slip dominance in the area of the small crack may have applications as to calculating the reversibility of cyclic deformation. Furthermore, computational experiments studying localized rotations and their role into sub-grain formation in monotonic loading should be matched to existing macroscopic EBSD texture results concurrently with SEM measurements of intragranular deformation fields and localized rotations. For these experiments, more elements per grain should be used, with a suggested scope of approximately 200 elements per grain, and 300 grains. Therefore, each grain would have a much more well-defined mantle and core region. Also, the method should be applied to multiple grain sizes, to see if the size of the mantle region is a function of the grain size, or is a constant size regardless of the size of the grain.

By understanding these extra degrees of freedom which are not captured in the macroscopic stress-strain response through further comparison to multi-axial loading, pole figures that result from this loading, and the effect of multiple grain sizes, the accuracy of a Mantle-Core approach to limited slip will be more thoroughly assessed.

REFERENCES

Abaqus (2006). Providence, RI, Abaqus Inc., Simulia.

Arzt, E. (1998). "Size effects in materials due to microstructural and dimensional constraints: a comparative review." Acta Materialia **46**(16): 5611-5626.

Asaro, R. J. (1983). "Crystal Plasticity." Journal of Applied Mechanics-Transactions of the Asme **50**(4B): 921-934.

Ashby, M. F. (1970). "Deformation of Plastically Non-Homogeneous Materials." Philosophical Magazine **21**(170): 399-&.

Ashby, M. F. (1972). "A first report on deformation-mechanism maps." Acta Metallurgica **20**(7): 887-897.

Barker, I., N. Hansen, et al. (1989). "The Development of Deformation Substructures in Face-Centered Cubic Metals." Materials Science and Engineering a-Structural Materials Properties Microstructure and Processing **113**: 449-454.

Bassani, J. L. and T.-Y. Wu (1991). "Latent Hardening in Single Crystals II. Analytical Characterization and Predictions." Proceedings: Mathematical and Physical Sciences **435**(1893): 21-41.

Bronkhorst, C. A., S. R. Kalidindi, et al. (1992). "Polycrystalline Plasticity and the Evolution of Crystallographic Texture in FCC Metals." Philosophical Transactions: Physical Sciences and Engineering **341**(1662): 443-477.

Buchheit, T. E., G. W. Wellman, et al. (2005). "Investigating the limits of polycrystal plasticity modeling." International Journal of Plasticity **21**(2): 221-249.

Chokshi, A. H., A. Rosen, et al. (1989). "On the validity of the hall-petch relationship in nanocrystalline materials." Scripta Metallurgica **23**(10): 1679-1683.

Christoffersen, H. and T. Leffers (1998). "The orientation of dislocation walls in rolled copper relative to the sample coordinate system." Acta Materialia **46**(12): 4093-4102.

Clausen, B., T. Lorentzen, et al. (1998). "Self-consistent modelling of the plastic deformation of f.c.c. polycrystals and its implications for diffraction measurements of internal stresses." Acta Materialia **46**(9): 3087-3098.

Clayton, J. D. and D. L. McDowell (2003). "A multiscale multiplicative decomposition for elastoplasticity of polycrystals." International Journal of Plasticity **19**(9): 1401-1444.

Conrad, H. (2004). "Grain-size dependence of the flow stress of Cu from millimeters to nanometers." Metallurgical and Materials Transactions A **35**(9): 2681-2695.

Csikor, F. F., C. Motz, et al. (2007). "Dislocation Avalanches, Strain Bursts, and the Problem of Plastic Forming at the Micrometer Scale." Science **318**(5848): 251-254.

Cuitino, A. M. and M. Ortiz (1992). "Material-independent method for extending stress update algorithms from small-strain plasticity to finite plasticity with multiplicative kinematics." Engineering Computations **9**(4): p437-451.

Fleck, N. A., M. F. Ashby, et al. (2003). "The role of geometrically necessary dislocations in giving material strengthening." Scripta Materialia **48**(2): 179-183.

Gourdin, W. H. and D. H. Lassila (1991). "Flow stress of OFE copper at strain rates from 10-3 to 104s-1: Grain-size effects and comparison to the mechanical threshold stress model." Acta Metallurgica Et Materialia **39**(10): 2337-2348.

Haldrup, K., R. D. McGinty, et al. (2009). "Effects of constraints on lattice re-orientation and strain in polycrystal plasticity simulations." Computational Materials Science **44**(4): 1198-1207.
Hall, E. O. (1951). "The Deformation and Ageing of Mild Steel." Proceedings of the Physical Society of London Section B **64**(381): 747-753.
Hansen, N. (2004). "Hall-Petch relation and boundary strengthening." Scripta Materialia **51**(8): 801-806.
Harewood, F. J. and P. E. McHugh (2007). "Comparison of the implicit and explicit finite element methods using crystal plasticity." Computational Materials Science **39**(2): 481-494.
Hill, R. (1966). "Generalized Constitutive Relations for Incremental Deformation of Metal Crystals by Multislip." Journal of the Mechanics and Physics of Solids **14**(2): 95-&.
Hill, R. and J. R. Rice (1972). "Constitutive Analysis of Elastic-Plastic Crystals at Arbitrary Strain." Journal of the Mechanics and Physics of Solids **20**(6): 401-&.
Horstemeyer, M. F., D. L. McDowell, et al. (1999). "Design of experiments for constitutive model selection: application to polycrystal elastoviscoplasticity." Modelling and Simulation in Materials Science and Engineering **7**(2): 253-273.
Hughes, D. A., D. C. Chrzan, et al. (1998). "Scaling of misorientation angle distributions." Physical Review Letters **81**(21): 4664-4667.
Hughes, D. A., Q. Liu, et al. (1997). "Scaling of microstructural parameters: Misorientations of deformation induced boundaries." Acta Materialia **45**(1): 105-112.
Johnson, G. R. and W. H. Cook (1985). "Fracture characteristics of three metals subjected to various strains, strain rates, temperatures and pressures." Engineering Fracture Mechanics **21**(1): 31-48.
Kawasaki, Y. and T. Takeuchi (1980). "Cell Structures in Copper Single Crystals Deformed in the 001 and 111 Axes." Scripta Metallurgica **14**(2): 183-188.
Khan, A. S., Huang, Sujian., Ed. (1995). Continuum Theory of Plasticity. New York :, Wiley,.
Kocks, U. F. and H. Mecking (2003). "Physics and phenomenology of strain hardening: the FCC case." Progress in Materials Science **48**(3): 171-273.
Kuhlmann-Wilsdorf, D. (1998). "Questions you always wanted (or should have wanted) to ask about workhardening." Materials Research Innovations **1**(4): 265-297.
Kuhlmann-Wilsdorf, D. and N. Hansen (1991). "Geometrically necessary, incidental and subgrain boundaries." Scripta Metallurgica Et Materialia **25**(7): 1557-1562.
Kumar, R., A. Wang, et al. (2006). "Effects of Microstructure Variability on Intrinsic Fatigue Resistance of Nickel-base Superalloys – A Computational Micromechanics Approach." International Journal of Fracture **137**(1): 173-210.
Liao, X. Z., Y. H. Zhao, et al. (2004). "Deformation twinning in nanocrystalline copper at room temperature and low strain rate." Applied Physics Letters **84**(4): 592-594.
Ling, X. W., M. F. Horstemeyer, et al. (2005). "On the numerical implementation of 3D rate-dependent single crystal plasticity formulations." International Journal for Numerical Methods in Engineering **63**(4): 548-568.

Mayeur, J. R. (2004). Three Dimensional Modeling of Ti-Al Alloys with Application to Attachment Fatigue. Mechanical Engineering. Atlanta, Georgia Institute of Technology. **M.S.**

McDowell, D. L. "A perspective on trends in multiscale plasticity." International Journal of Plasticity **In Press, Corrected Proof**.

McDowell, D. L. (2008). "Viscoplasticity of heterogeneous metallic materials." Materials Science & Engineering R-Reports **62**(3): 67-123.

McGinty, R. D. (2001). Multiscale Representation of Polycrystalline Inelasticity. Mechanical Engineering. Atlanta, Georgia Institute of Technology. **PhD.**

McGinty, R. D. (2001). Multiscale representation of polycrystalline inelasticity. Atlanta, Ga. :, Georgia Institute of Technology.

Mecking, H. and U. F. Kocks (1981). "Kinetics of flow and strain-hardening." Acta Metallurgica **29**(11): 1865-1875.

Meyers, M. A. and E. Ashworth (1982). "A model for the effect of grain size on the yield stress of metals." Philosophical Magazine A **46**(5): 737-759.

Meyers, M. A., A. Mishra, et al. (2006). "Mechanical properties of nanocrystalline materials." Progress in Materials Science **51**(4): 427-556.

Mughrabi, H. (1971). "Electron Microscope Investigations of the Dislocation Arrangement of Deformed Copper Single Crystals in the Stress-Applied State." Phil. Mag. **23**(Apr): 931-947.

Mughrabi, H. (1983). "Dislocation Wall and Cell Structures and Long-Range Internal-Stresses in Deformed Metals Crystals." Acta Metallurgica **31**(9): 1367-1379.

Musienko, A., A. Tatschl, et al. (2007). "Three-dimensional finite element simulation of a polycrystalline copper specimen." Acta Materialia **55**(12): 4121-4136.

Narutani, T. and J. Takamura (1991). "Grain-size strengthening in terms of dislocation density measured by resistivity." Acta Metallurgica Et Materialia **39**(8): 2037-2049.

Ohashi, T., M. Kawamukai, et al. (2007). "A multiscale approach for modeling scale-dependent yield stress in polycrystalline metals." International Journal of Plasticity **23**(5): 897-914.

Ohno, N. and D. Okumura (2007). "Higher-order stress and grain size effects due to self-energy of geometrically necessary dislocations." Journal of the Mechanics and Physics of Solids **55**(9): 1879-1898.

Parks, D. M. and S. Ahzi (1990). "Polycrystalline plastic deformation and texture evolution for crystals lacking five independent slip systems." Journal of the Mechanics and Physics of Solids **38**(5): 701-724.

Peirce, D., R. J. Asaro, et al. (1983). "Material Rate Dependence and Localized Deformation in Crystalline Solids." Acta Metallurgica **31**(12): 1951-1976.

Petch, N. J. (1953). "The Cleave Strength of Polycrystals." Journal of the Iron and Steel Institute **174**(1): 25-28.

Przybyla, C. P. and D. L. McDowell (2010). "Microstructure-sensitive extreme value probabilities for high cycle fatigue of Ni-base superalloy IN100." International Journal of Plasticity **26**(3): 372-394.

Schiøtz, J. (2004). "Atomic-scale modeling of plastic deformation of nanocrystalline copper." Scripta Materialia **51**(8): 837-841.

Schmid, E. (1924). Proc. Int. Congr. Appl. Mech.

Staker, M. R. and D. L. Holt (1972). "The dislocation cell size and dislocation density in copper deformed at temperatures between 25 and 700°C." Acta Metallurgica **20**(4): 569-579.
Suresh, S. (1991). Fatigue of Materials. Cambridge [England].
Tatschl, A. and O. Kolednik (2003). "A new tool for the experimental characterization of micro-plasticity." Materials Science and Engineering A **339**(1-2): 265-280.
Taylor, G. I. (1938). "Plastic strain in metals." Journal of the Institute of Metals **62**: 307-324.
Taylor, G. I. and C. F. Elam (1925). "The Plastic Extension and Fracture of Aluminium Crystals." Proceedings of the Royal Society of London. Series A, Containing Papers of a Mathematical and Physical Character **108**(745): 28-51.
Uchic, M. D., D. M. Dimiduk, et al. (2004). "Sample dimensions influence strength and crystal plasticity." Science **305**(5686): 986-989.
van der Sluis, O., P. J. G. Schreurs, et al. (2000). "Overall behaviour of heterogeneous elastoviscoplastic materials: effect of microstructural modelling." Mechanics of Materials **32**(8): 449-462.
Weisstein, E. W. (2010). ""Line-Plane Intersection"." Retrieved Dec 10, 2009, from http://mathworld.wolfram.com/Line-PlaneIntersection.html.
Yang, W., Lee, W. B. (1993). Mesoplasticity and its applications, Berlin ; New York : Springer-Verlag, c1993.
Zaiser, M., K. Bay, et al. (1999). "Fractal analysis of deformation-induced dislocation patterns." Acta Materialia **47**(8): 2463-2476.